Stimulated Raman Scattering Imaging of Biomolecules and Single Cell Transcriptome Analysis of Mouse Retina

Stimulated Raman Scattering Imaging of Biomolecules and Single Cell Transcriptome Analysis of Mouse Retina

A dissertation presented

by

Xu Zhang

to

The School of Engineering and Applied Sciences

in partial fulfillment of the requirements

for the degree of

Doctor of Philosophy

in the subject of

Applied Physics

Harvard University

Cambridge, Massachusetts

April 2015

Dissertation Advisor: Professor Xiaoliang Sunney Xie Xu Zhang

Stimulated Raman Scattering Imaging of Biomolecules and Single Cell Transcriptome Analysis of Mouse Retina

Abstract

Complex information within biological systems is being uncovered at an unprecedented speed thanks to the rapid technical development of a wide variety of research tools, among which imaging and sequencing technologies are attracting big attention in recent years. Optical imaging enables the visualization of the spatial distribution of biomolecules at cellular level, allowing deeper understanding of the structure and dynamics of biological systems. Fluorescence microscopy has contributed greatly to our understanding of these processes, but it relies on the use of fluorescent labels or dyes. These labels may perturb the studied systems especially for imaging small molecules, and the photobleaching problem also limits the long-term biological dynamics observation within living cells. In the first part of this dissertation, we introduce the recent development of Stimulated Raman scattering (SRS) microscopy as a noninvasive imaging technique with superior sensitivity, molecular specificity at video-rate imaging speed. It has superseded coherent anti-Stokes Raman scattering (CARS) microscopy due to the absence of non-resonant background and automatic phase matching. However, SRS imaging has been mostly demonstrated for the visualization of lipid and protein with long vibrational wavenumbers. We extend the detectability of SRS imaging into the crowded fingerprint region with characteristic signatures of more biomolecules such as nucleic acids in live cells (Chapter 2), unsaturated lipid and aromatic amino acid in multiphasic food products (Chapter 3).

Noninvasiveness of SRS imaging also brings new opportunities to biomedical applications and we demonstrate its feasibility as a potential pathology diagnostic tool by generating comparable image contrast as golden standard H&E staining in human brain frozen sections (Chapter 4). We further extend SRS imaging to real-time multiband detection using a novel modulation multiplex approach (Chapter 5).

The rapid development of high throughput sequencing technologies has enabled whole genome and transcriptome wide analysis at faster speed and affordable cost, but a large number of cells are often still required for these analyses. However, cell-to-cell variation is significant and may carry important indication to the study of complex wiring in the nervous systems. In this second part of the dissertation, we explore the heterogeneity of retina using a recently developed single cell transcriptome amplification technique based on Multiple Annealing Looping Based Amplification Cycles (MALBAC), which is superior to other single cell techniques with its low amplification bias, high reproducibility rate and low dropout rate. We first classify different retinal cell populations (photoreceptor cells vs. retinal ganglion cells) and closely related subpopulations (different direction selective retinal ganglion cells) (Chapter6). We further study the molecular divergence of an unsolved ON-OFF retina circuit responsible for direction selectivity function. We show that the inhibitory interneurons responsible for this function can be classified into two clusters based on the single cell transcriptome data. This clustering result strongly correlates with the ON-OFF starburst amacrine cells (SACs) based on the immunostaining results of the identified differential genes. The newly reported differential genes can potentially be used as molecular markers for ON-OFF SACs with more validation underway (Chapter 7). These new findings open up more opportunities for the functional studies on the direction-selective circuit in retina.

Contents

List of Figures and Tables

Acknowledgements

There are many people I need to thank for providing tremendous support throughout my PhD study. It has been a very challenging journey and I could not make it without their guidance, encouragement and support.

First and foremost, I would like to thank my thesis advisor, Professor Xiaoliang Sunney Xie, for his great support and mentorship during my PhD research. I am grateful for his trust and allowing me to pursue my research interests in different fields, as well as providing guidance and resources along the way. I have learned a lot from his dedication in scientific research, great insights in the academic trend and management style for motivating people to achieve their personal goals. I believe the inspirations I got from him will be very beneficial for my future career development as well.

I also want to thank another three members on my thesis committee: my SEAS co-adviser Prof. David A. Weitz, Prof. Joshua R. Sanes with whom I had a close collaboration for my project described in Chapter 6-7 and Prof. Marco Loncar. In addition, I also want to thank Prof. Daniel Needleman for serving on my oral qualification exam committee. I am grateful for their precious time and valuable advice to my qualify exam as well as dissertation defense. Especially Prof. Joshua Sanes provided great mentorship and support in our collaborative project and I learned a lot of scientific thinking in neural biology from him.

My advisor Sunney has also created an amazing research group in which I had stimulating experiences working with exceptional people. I had a great opportunity working with many people in the group especially the people in the SRS imaging subgroup as wells as single cell DNA/RNA sequencing subgroup. I want to thank Dr. Brian Saar and Dr. Christian Freudiger for introducing me to the work at the group and provided great mentorship at the beginning of my

PhD career. They shared their insights upon the optical imaging field and provided hands-on guidance on optics and electronics, which helped me pick up the technical tips more quickly than I would expect. I had a close collaboration with Dr. Maarteen Roeffers for several imaging projects, which led to my initial contribution to the field. I had also worked closely with Dr. Srinjan Basu on the DNA imaging project and learned a lot of cell biology from him. I also worked closely with Dr. Dan Fu on another two imaging projects and his passion in pushing the advancement of technical development has influenced me a lot and I had learned a lot of technical implementation during our collaboration. I also want to thank Dr. Geoffrey S. Young and Dr. Pedro Diarlini for their collaboration on the pathology project. Dr. Gary Holtom has helped me tremendously as well in achieving some detailed technical research goals. I am so expressed by his broad range of knowledge and expertise in optics. I also enjoyed working with Dr. Fa-Ke Lu and Dr. Minbiao Ji in the SRS imaging subgroup. With the great chance to explore the genomics field provided by my advisor, I also learned a lot from the people in the sequencing subgroup. I started working in this field with Jenny Lu, who was then a talented undergrad student, now a MD/PhD student in Harvard Medical School. I learned a lot from her, Dr. Sijia Lu and Dr. Dong Xing and Zi He on the hands on experiment skills in sequencing. I worked closely with Dr. Yirong Peng in Prof. Joshua R. Sanes' lab for my last project. We had numerous communications on the research project over many phone calls, meetings and hundreds of email exchange over the last 2 years. She is a very hard working, sharing person and a great researcher. I also want to thank Alec Chapman and Guangyu Zhou for their help and consultation on data analysis, Longzhi Tan for coordinating sequencing runs, sharing reagents and helpful discussion. There are so many people in the lab that I interacted with and learned from them in many different aspects: Dr. Lin Song for her support and ordering chemical reagents, Larry Valles,

Tracey Schaal, Teri Howard and Patricia Purcell for help on administrative issues, Dr. Chongyi Chen, Winston Zhao, Dr. Shasha Chong, Dr. Xiaohui Ni and Ang Li for helpful discussions.

I am also very lucky to have my family and many friends supporting me throughout my PhD life. Without their encouragement and unconditional support, it would not be possible for me to achieve any of these. I want to express my greatest gratitude to them.

Citation to Previously Published Work

Section 1.3.3 has been previously published with minor changes in the following papers:

C.W. Freudiger, M.B.J. Roeffaers, **X. Zhang**, S.G. Brian, M. Wei, X.S. Xie. "Optical Heterodyne-Detected Raman-Induced Kerr Effect (OHD-RIKE) Microscopy', *J Phys Chem B* **115**, 5574-5581 (2011).

Chapter 2 has been previously published with minor changes as the following papers:

> **X. Zhang***, M.B.J. Roeffaers*, S. Basu*, J. R. Daniele, D. Fu, C. W. Freudiger, G. R. Holtom, X. S. Xie, " Label-Free Live-Cell Imaging of Nucleic Acids Using Stimulated Raman Scattering Microscopy", ChemPhysChem, **13**, 1054-1059 (2012).

Chapter 3 has been previously published with minor changes as the following papers:

> M.B.J. Roeffaers, **X. Zhang**, C.W. Freudiger, B. G. Saar, M. van Ruijven, G. van Dalen, C. Xiao, X. S. Xie, " Label-free Imaging of Biomolecules in Food Products Using Stimulated Raman Microscopy", *J Biomed Opt* **16**(2), 021118-(1-6) (2011).

Chapter 5 has been previously published with minor changes as the following papers:

> D. Fu, F. Lu, **X. Zhang**, C.W. Freudiger, D. Pernik, G. R. Holtom, X. S. Xie, "Quantitative Chemical Imaging with Multiplex Stimulated Raman Scattering Microscopy", *J. Am. Chem. Soc.*, **134**, 3623-3226 (2012)**.**

* : Equal Contribution Authors

Part I (Chapter 1-5)
Stimulated Raman Scattering Imaging of Biomolecules

Chapter 1

Introduction to Coherent Raman Scattering Microscopy

The rapid advancement of optical microscopy techniques has enabled better understanding of biological and medical systems by visualizing the distribution and dynamics of various biomolecules at the subcellular level. Among a large variety of imaging techniques, fluorescence microscopy has been widely used for understanding biological processes. However, the dependence on exogenous labels or dyes may perturb the system, especially for the study of small molecules. Fluorescence imaging also suffers from photobleaching problem, making long-term dynamics study very difficult. Due to these reasons non-invasive label-free imaging techniques are highly desirable. Raman microscopy is a label-free imaging technique that offers contrast based on vibrational frequencies that are characteristic of chemical bonds, however its imaging speed and sensitivity are limited by its weak signal level. Coherent Raman scattering techniques have been developed in recent years with great signal enhancement, which allows for fast imaging speed. However, CARS microscopy has been limited by the presence of a nonresonant background, which causes image artifacts and limits sensitivity. Stimulated Raman scattering (SRS) has overcome all of these problems and opens up new opportunities of detecting more species in living systems. Here we discuss the theoretical background of spontaneous Raman and Coherent Raman techniques and especially focus on the comparison between CARS and SRS as well as newly reported OHD-RIKE. We will explain why SRS is the best option to pursue label-free imaging.

1.1 Label-free Optical Imaging

The technical advancement of optical imaging has been driving the research in a wide variety of biological systems. Fluorescence imaging has been most widely used in biological research (Pawley, 2006) with great specificity coming from targeted labels. Fluorescent proteins (Chalfie et al., 1994; Zhang et al., 2002), exogenous dyes are usually incorporated to the systems to assist the visualization. Several major techniques such as confocal laser scanning technique (Pawley, 2006), two-photon excited fluorescence (TPEF) (Denk et al, 1990), single-molecule microscopy (Moerner, 1999; Xie, 1998) and super-resolution imaging (Hell, 1994; Betzig et al., 2006; Rust, 2006) have been developed based on fluorescence mechanism.

However, for imaging nonfluorescent molecules, the labeling approach sometimes brings unwanted perturbation to the studied systems. This is especially true when the fluorescent labels are larger than the molecules of interest such as metabolites, drugs, peptides and neurotransmitters. In addition to that, fluorescence based techniques cannot be used for in vivo medical applications especially for the body parts lacking autofluorescence.

Therefore label-free optical imaging with high sensitivity is highly desirable and recently a variety of label-free microscopy techniques have been developed such as infrared absorption and Raman scattering. The technical development of vibrational spectroscopy brings new opportunities for chemical imaging based on the distinctive vibrational fingerprints of different molecules (Raman and Krishnan, 1928; Turrell and Corset, 1996). However, infrared microscopy suffers from low spatial resolution due to the long wavelength and strong water absorption in the infrared also limits the penetration depth into aqueous samples. Raman scattering, on the other hand, has low signal level and requires long integration time to achieve a good image contrast. Here we discuss the major coherent Raman techniques that greatly enhance

the efficiency and also conduct comparison on advantages and disadvantages of each one.

1.2 Spontaneous Raman Scattering

The basis for the technical development of Raman spectroscopy and microscopy dates back to the early discovery of Raman effect by Indian physicist Sir C.V. Raman (Raman and Krishnan, 1928). It was found that when an incident light beam interacted with a certain matter, most of the photons were scattered elastically without any change in frequency, wavelength and energy. This is called Rayleigh scattering process. However a small portion of the photons went through a different process making the scattered photons carry different frequencies and wavelengths. This is an inelastic scattering process termed as Raman effect. The energy difference corresponds to the vibrational or rotational energy of the matter. When spectroscopy technique is carried out on chemical compounds, the vibrational energy is usually concerned. The following figure represents the energy level diagrams for the Rayleigh scattering process and two different kinds of Raman scattering processes.

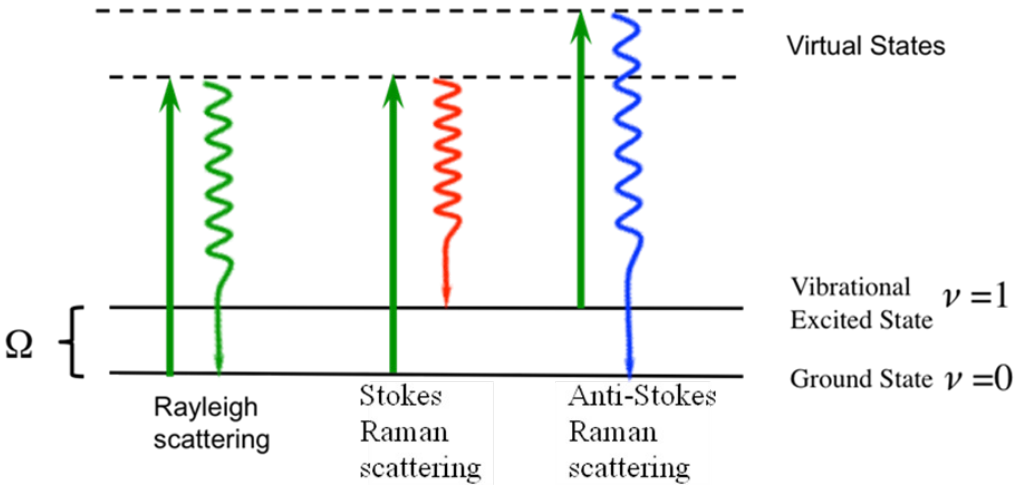

Figure1.1 Energy level diagram of Rayleigh scattering and Raman scattering

The scattering intensity scales as the square of the induced dipole moment. Therefore for highly

polar moiety such as O-H bond, the scattering intensity is weak while for moieties with distributed electron clouds such as C=C bond, the scattering intensity is relatively strong.

1.3 Coherent Raman Scattering

Coherent Raman scattering techniques hold the similar information as spontaneous Raman scattering, but has much higher intensity level. The great intensity enhancement is due to the driving force resulted from two incident laser fields carrying different frequencies. The frequency difference drives the molecule to achieve a vibrational mode and in return the vibrating molecules modulate the dielectric constant thus producing a coherent Raman light beam with altered frequency and polarization.

The polarization of the sample can usually be written as a power serious of the excitation fields. The general expression for the third order contribution at the frequency ω_4 is

$$P^{(3)}(\omega_4) = \chi^{(3)}(\omega_4;\omega_1,\omega_2,\omega_3)\cdot E(\omega_1)\cdot E(\omega_2)\cdot E(\omega_3) \qquad (1)$$

where $\chi^{(3)}(\omega_4;\omega_1,\omega_2,\omega_3)$ is the non-linear optical susceptibility and $E(\omega_1)$, $E(\omega_2)$ and $E(\omega_3)$ are the electric fields of the excitation beams at, ω_1, ω_2 and ω_2(Levenson and Kano, 1982). All vibrational information about the sample is contained in $\chi^{(3)}(\omega_4;\omega_1,\omega_2,\omega_3)$, which, far from electronic resonance, has a resonant contribution from the vibrational resonance $\chi_r^{(3)}$ and a non-resonant contribution from the electronic response $\chi_{nr}^{(3)}$:

$$\chi^{(3)}(\omega_4;\omega_1,\omega_2,\omega_3) = \mp\left(\sum_i \frac{A_i}{\Omega_i - (\omega_1+\omega_2) - i\cdot\Gamma_i} + \chi_{nr}^{(3)}\right)$$

where the sum is performed over all vibrational resonances of the sample with center frequencies Ω_i, Ω_i is proportional to the particular spontaneous Raman cross-section and Γ_i is the half-width at half maximum (Boyd, 2008). Because the electronic response of the non-resonant

background is instantaneous, $\chi_{nr}^{(3)}$ is purely real, while the resonant contribution $\chi_{r}^{(3)}$ has real and imaginary components. This results in a phase shift of the non-linear polarization with respect to the excitation fields.

This non-linear polarization further has to be treated as a tensor $\chi_{\alpha\beta\gamma\delta}^{(3)}$, in which α, β, γ and δ are the indices of the polarization components of the electrical field $E_{\alpha}(\omega_1)$, $E_{\beta}(\omega_2)$, $E_{\gamma}(\omega_3)$ and $E_{\delta}(\omega_4)$ in the x-, y- and z-direction. Depending on the symmetry of the system, only certain combinations are allowed. Specifically, in isotropic samples $\chi_{1111}^{(3)}$, $\chi_{1122}^{(3)}$, $\chi_{1212}^{(3)}$ and $\chi_{1221}^{(3)}$ and their permutations are the only non-vanishing elements. Their resonant contributions can be related to the spontaneous Raman cross section σ and the Raman depolarization ratio ρ (Levenson, 1982).

1.3.1 Coherent Anti-Stokes Raman Scattering(CARS)

In CARS, two incident beams with parallel polarizations are mixed in the sample. One incident carries the frequency of ω_1 corresponding to the laser frequency in the case of spontaneous Raman spectroscopy, while another incident beam carries the frequency of ω_2 corresponding to the Stokes scattered beam in spontaneous Raman scattering. The difference frequency corresponds to the vibrational frequency (Raman resonance frequency) of the sample. These two incident beams generate a new frequency: $\omega_3 = 2\omega_1 - \omega_2$ which is the anti-Stokes frequency carried with the signal field. The energy level diagram for CARS is illustrated in Figure 1.2. The presented case here is with $\omega_1 > \omega_2$. A similar case is with $\omega_1 < \omega_2$, which is called coherent Stokes Raman scattering (CSRS). CARS is associated with the third order susceptibility of $\chi_{1111}^{(3)}$. In this notation, CARS excitation is at $\omega_1 = \omega_3 = \omega_p$ and $\omega_2 = -\omega_S$ and emission is at $\omega_1 = \omega_3 = \omega_p$. The original implementation of CARS requires parallel and linearly polarized excitation fields

where $\chi^{(3)}_{1111}$ is measured.

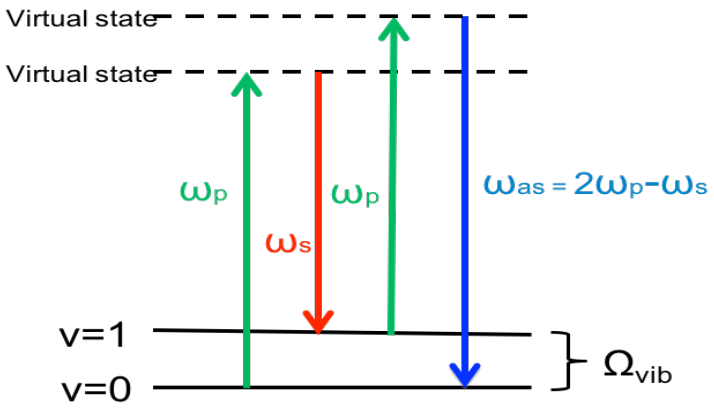

Figure1.2 Energy level diagram of CARS

In this process, the induced polarization density is

$$P_x(\omega_3) = \frac{3}{8}\chi_{1111}(\omega_3;\omega_1,-\omega_2,\omega_1)E_x(\omega_1)E_x^*(\omega_2)E_x(\omega_1)$$

From the wave equation using slowly varying wave approximation, we get the signal field

$$E_x = \frac{3}{8}i\omega_3\sqrt{\frac{\mu_0}{\varepsilon_3\varepsilon_0}}\chi_{1111}(\omega_3;\omega_1,-\omega_2,\omega_1)E_x^2(\omega_1)E_x^*(\omega_2)L\,\mathrm{sinc}\left(\frac{\Delta kL}{2}\right)$$

where $\Delta k = \left|(2\mathbf{k}_1 - \mathbf{k}_2 - \mathbf{k}_3)\cdot \mathbf{z}\right|$ is the phase matching angle. The phase matching condition for CARS is shown below (Figure 1.3).

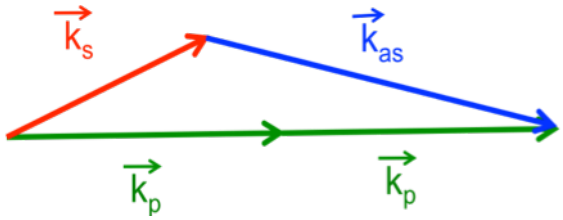

Figure 1.3 Phase matching condition for CARS

Separating the susceptibility to the nonresonant term and real and imaginary resonant terms, we

get the four different contributions from the susceptibility to the detected intensity

$$I(\omega_3) = \frac{c}{2} n_3 \varepsilon_0 \left| E_x(\omega_3) \right|^2 = \frac{9\omega_3^2 \mu_0^2}{16 n_1^2 n_2 n_3 \varepsilon_0^2} I^2(\omega_1) I(\omega_2) L^2 \sin c^2\left(\frac{\Delta k L}{2}\right) \times \left| \chi_{1111}^{NR} + \chi_{1111}^{'} + i\chi_{1111}^{''} \right|^2$$

$$= \frac{9\omega_3^2 \mu_0^2}{16 n_1^2 n_2 n_3 \varepsilon_0^2} I^2(\omega_1) I(\omega_2) L^2 \sin c^2\left(\frac{\Delta k L}{2}\right) \times [(\chi_{1111}^{NR})^2 + (\chi_{1111}^{'})^2 + (\chi_{1111}^{''})^2 + 2\chi_{1111}^{NR}\chi_{1111}^{'})]$$

Here we see signal from non-resonant backgroudn presented in the first term and spetral distortion due to the mixing of resonant and non-resonant signal presented in the fourth term. These factos influence the specificiy of the detection scheme and greatly limit the sensitivity as well.

1.3.2 Stimulated Raman Scattering

Similar to CARS, the process of SRS also involves two incident beams: a pump beam with the frequency of ω_1 and a probe beam with the frequency of ω_2. These two beams are put in the sample of our interest at the same time, when $|\omega_1 - \omega_2|$ equals to the vibrational frequency of the sample, a change in the frequencies of two incident beams are observed. When $\omega_1 > \omega_2$, a gain is produced for the probe beam, which is called Raman gain. When $\omega_1 < \omega_2$, attenuation in the probe beam is observed, which is called Raman loss. Figure 1.4a illustrates the energy level diagram for SRS. This diagram looks similar to that of spontaneous Raman, but is different in principle. The incident photon is not scattered by the vibrational phonon but scattered by stimulated phonon generated by the collision of the incident photon and the vibrational phonon. When the incident photon collides with this stimulated phonon again, another stimulated phonon is generated. Therefore, this process can be described by the avalanche behavior of stimulated phonons. The energy transfer involved in this light matter interaction process is illustrated in Figure 1.4b. Part of the intensity loss in pump beam is transferred as the intensity gain in Stokes

beam. The net energy loss in these two excitation beams is used to drive the molecules from ground state to vibrational excited state.

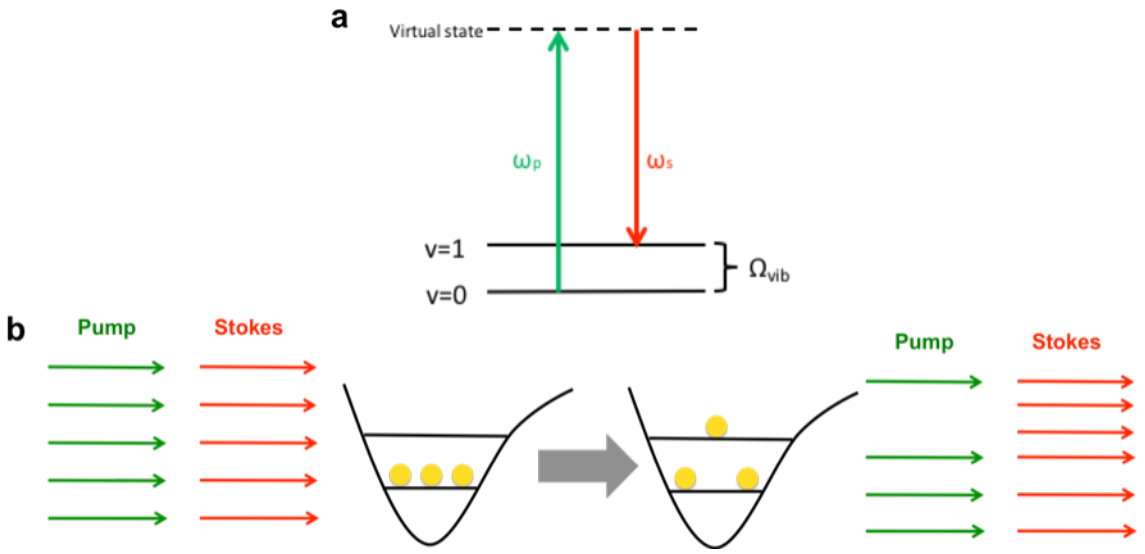

Figure 1.4 (a) Energy level diagram (b) Schematic of light matter interaction process of SRS

In SRS, the two incident fields (pump and probe) are parametrically coupled. This process can be described by the following coupled wave equation

$$\left(\frac{\partial^2 \mathbf{Q}}{\partial t^2}\right)^* + 2\Gamma\left(\frac{\partial \mathbf{Q}}{\partial t}\right)^* + (\beta^2\nabla^2 + \omega_0^2)\mathbf{Q}^* = N\frac{\partial \alpha}{\partial Q}\mathbf{E}_2\mathbf{E}_1^*$$

$$\nabla^2\mathbf{E}_2 - \frac{\varepsilon_0}{c^2}\frac{\partial^2}{\partial t^2}\mathbf{E}_2 = -\frac{4\pi}{c^2}N\frac{\partial \alpha}{\partial Q}\frac{\partial^2}{\partial t^2}\mathbf{Q} * \mathbf{E}_1$$

Here $\mathbf{E}_1$ and $\mathbf{E}_2$ are the electric fields of pump beam and Stokes beam. $\mathbf{Q}$ is defined earlier as the dynamical coordinate variable. The first equation is derived previous in the theory of coherent Raman scattering except a correction term $\beta^2\nabla^2\mathbf{Q}$ which corresponds to the propagation of the stimulated phonon, but this term does not have much effect in the process of scattering. The second equation is easily derived from Maxwell equation.

Solving the above coupled equations, we can get the signal field as following

$$\frac{\partial E_i(\omega_2)}{\partial z} = \frac{3i\omega_2}{4cn_2}\chi^{(3)}_{ijkl}(\omega_2;\omega_1,-\omega_1,\omega_2)E_j(\omega_1)E^*_k(-\omega_1)E_l(\omega_2)$$

For the third order susceptibility, we need to consider the symmetry involved in this process. In SRS, the polarization of the probe field can be either parallel or perpendicular to the pump field. Therefore the susceptibility involved here can be written as $\chi^{(3)}_{1111}$ and $\chi^{(3)}_{1221}$.

Next we want to compare the signal amplitude between SRS and spontaneous Raman. This comparison can be evaluated from the cross sections involved in these two processes. For SRS, we have

$$\frac{d^2\sigma_{SRS}}{d\Omega d\omega_2} = \frac{32\pi^2\hbar\omega_1\omega_2 F(\omega_2)}{c^2 N}\mathrm{Im}\,\chi^3_R$$

where the number density of molecules is defined as N and $F(\omega_2)$is defined as the spectral photon flux. For spontaneous Raman scattering

$$\frac{d^2\sigma_{Spon}}{d\Omega d\omega_2} = \frac{\hbar\omega_1\omega_2^3}{\pi c^2 N}\mathrm{Im}\,\chi^3_R$$

Comparing these two cases, we take the ratio of these equations

$$\frac{d^2\sigma_{SRS}}{d\sigma^2_{spon}} = \frac{32\pi^3 c^2}{\omega_2^2}F(\omega_2)$$

From the above equations, we see that the Raman gain signal increases with smaller frequency (red shift) of the Stokes field. Moreover this gain is proportional to the cube of the imaginary part of the third order nonlinear susceptibility which is the resonant part. Therefore the lineshape should be similar to spontaneous Raman scattering process. Considering the phase matching condition, we find SRS is actually a self-matched process. This is a big advantage over CARS, which requires phase matching. This process can generate beams coherently with the probe beam so this technique is suitable to be used in the study of fluorescent molecules. More comprehensive comparison between CARS and SRS is summarized in Table 1.1.

Table 1.1. Comparison of CARS and SRS

CARS	SRS
Parametric process	Energy transfer process
Complex vibrational spectra	Identical to spontaneous Raman spectra
Signal generated at new optical frequency	Signal at the same frequency as one excitation beam
Linear to quadratic concentration dependence	Linear concentration dependence
Sensitivity limited by non-resonant background	No non-resonant background
Phase matching required	Automatically phase matched

1.3.3 Raman-induced Kerr-effect (RIKE)

This technique utilizes the principles of the optical Kerr effect related to the field-induced birefringence. The birefringence induced by a strong pump beam passing though a nonlinear medium changes the polarization of a weaker probe beam. If we put a polarizer after the sample with the perpendicular polarization with the probe beam, the polarization change in probe beam can be measured as the transmitted intensity increase.

In the original implantation of SRS microscopy, parallel and linearlypolarized excitation fields were used, where $\chi^{(3)}_{1111}$ was measured (Figure 1.5). It is straightforward to also measure features of $\chi^{(3)}_{1221}$ by using linearly-polarized pump and Stokes beams with perpendicular polarization. In the SRL analog of RIKE, the emission is perpendicular to the original polarization of the pump beam, which we detect by blocking the transmitted pump beam with a cross-polarizer and measuring the polarization rotation due to the nonlinear interaction with the sample. Traditionally, two different beam geometries have been routinely used: one employs a linearly-polarized Stokes beam at a 45° angle with respect to pump beam (known as linear RIKE), the other uses a circularly-polarized Stokes beam (known as circular RIKE) (Figure 1.5). The RIKE

non-linear polarization at the pump frequency is proportional to $\chi^{(3)}_{1122} + \chi^{(3)}_{1212}$ for the linear RIKE and $i \cdot \left(\chi^{(3)}_{1122} - \chi^{(3)}_{1212}\right)$ in case of the circularly RIKE, where i indicates that the polarization is phase-shifted by 90° with respect to the phase of the pump beam (Levenson and Kano, 1982). Thus, the combination of SRS and RIKE microscopy can probe the distribution of all important tensor elements of the non-linear susceptibility in the sample.

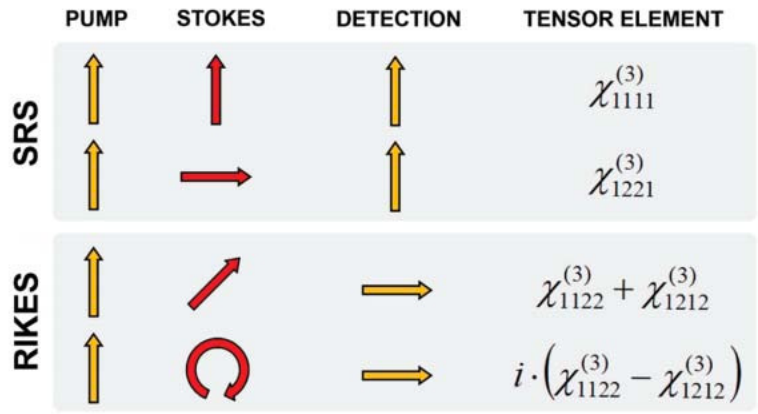

Figure 1.5 Polarization configuration for SRS and RIKE of the pump beam. The first two columns show the polarization of the excitation fields (pump and Stokes) and the third column the orientation of a polarizer in front of the detector, which is sensitive for the pump beam only. Configurations in which detection is along the polarization of the pump beam are referred to as SRS, and configurations in which detection is perpendicular to the polarization of the pump beam as RIKE. In isotropic samples, $\chi^{(3)}_{1111}$, $\chi^{(3)}_{1122}$, $\chi^{(3)}_{1212}$ and $\chi^{(3)}_{1221}$ are the nonvanishing elements of the third order susceptibility tensors, so only the four configurations shown here generate a signal. RIKE requires the Stokes beam to have polarizations along both polarization axes. One can distinguish between linear RIKE, in which both polarizations have the same phase, and circular RIKE, in which one of the polarizations is shifted by 90°. The fourth column indicates the specific tensor elements that are probed.

Theoretically RIKE, in contrast to SRS, is a background-free technique as the emission is polarized perpendicular to the excitation light, which is blocked with a cross-polarizer. In practice, however, and especially in a microscopy configuration with a high numerical aperture (NA) objectives (Cheng, 2001), it is hard to suppress the excitation light sufficiently. It is thus useful to introduce a carefully controlled portion of the excitation light on purpose, e.g. by detuning either the cross-polarizer with respect to the excitation beams or the excitation beams

with respect to the cross-polarizer. Due to the coherent nature of RIKE, this portion of the transmitted excitation light interferes with the RIKE emission. Such approach is known as optical heterodyne detected RIKE (OHD- RIKE) (Heiman et al., 1976).

Optical heterodyne detection is a standard technique in spectroscopy. The general idea is that a small homodyne signal ΔE is amplified with a second, coherent electrical field at the same frequency E_{LO}, known as the local oscillator. Because of the coherent addition of the two fields, the overall detected intensity is proportional to

$$\left|E_{LO}+\Delta E\right|^2=\left|E_{LO}\right|^2+2\cdot\mathrm{Re}\left[E_{LO}\right]\cdot\mathrm{Re}\left[\Delta E\right]+2\cdot\mathrm{Im}\left[E_{LO}\right]\cdot\mathrm{Im}\left[\Delta E\right]+\left|\Delta E\right|^2$$

If $\left|E_{LO}\right|>>\left|\Delta E\right|$, the contribution due to the homodyne signal $\left|\Delta E\right|^2$ is negligible compared to the mixing term $2\cdot\mathrm{Re}\left[E_{LO}\right]\cdot\mathrm{Re}\left[\Delta E\right]+2\cdot\mathrm{Im}\left[E_{LO}\right]\cdot\mathrm{Im}\left[\Delta E\right]$. If heterodyne detection is further combined with a modulation transfer scheme, as used in SRS microscopy, the contribution of the local oscillator $\left|E_{LO}\right|^2$ is suppressed and only the mixing terms are detected. Depending on the phase of E_{LO}, the real and imaginary part of ΔE can be probed specifically because either $\mathrm{Re}\left[E_{LO}\right]$or $\mathrm{Im}\left[E_{LO}\right]$can be set equal to zero.

In CRS, the small homodyne signal ΔE is the radiation generated from the non-linear polarization $P^{(3)}(\omega_4)$. It turns out that ΔE is 90° phase-shifted with respect to $P^{(3)}(\omega_4)$ due to the Gouy phase-shift from focus to far-field (Boyd, 1980; Saleh et al, 1991). Thus

$$\mathrm{Re}\left[\Delta E(\omega_4)\right]\propto\mathrm{Im}\left[\chi^{(3)}(\omega_4;\omega_1,\omega_2,\omega_3)\right]\cdot E(\omega_1)\cdot E(\omega_2)\cdot E(\omega_3)$$

$$\mathrm{Im}\left[\Delta E(\omega_4)\right]\propto-\mathrm{Re}\left[\chi^{(3)}(\omega_4;\omega_1,\omega_2,\omega_3)\right]\cdot E(\omega_1)\cdot E(\omega_2)\cdot E(\omega_3)$$

with $E(\omega_1)$, $E(\omega_2)$, and $E(\omega_3)$ being real by definition. As such the signal in optically heterodyne detected CRS is proportional to

$$\left(\mathrm{Re}\left[E_{LO}\right]\cdot\mathrm{Im}\left[\chi^{(3)}\left(\omega_4;\omega_1,\omega_2,\omega_3\right)\right]-\mathrm{Im}\left[E_{LO}\right]\cdot\mathrm{Re}\left[\chi^{(3)}\left(\omega_4;\omega_1,\omega_2,\omega_3\right)\right]\right)\cdot E(\omega_1)\cdot E(\omega_2)\cdot E(\omega_3).$$

In OHD-RIKE some of the excitation beam is rotated to match the emission polarization, allowing us to provide a local oscillator with adjustable strength and phase. In contrast to SRS, in OHD-RIKE the local oscillator strength can thus be optimized and both the real and imaginary parts of the non-linear susceptibility tensor can be probed selectively.

In general chemical imaging aims at detecting the resonant response of the sample (i.e. the imaginary part of the non-linear respnse), which carries the chemically-specific information. Whereas in CARS microscopy, this weak resonant response can be overwhelmed by the non-resonant background, SRS has improved the detection limitation of label-free microscopy by overcoming this notorious background signal. However, another, much weaker, spurious background signal from cross-phase modulation (XPM) can be the limiting factor when pushing the sensitivity limit to low chemical concentrations (Ekvall et al., 2000; Freudiger et al., 2008).

XPM is detected in SRS microscopy because the modulated Stokes beam intensity causes a modulation of the refractive index in focus due to the Kerr effect. This results in a modulation of the divergence of the transmitted pump beam. If the pump beam, after passing through the focus, strikes any type of aperture (e.g. the edges of the collection optics), this divergence modulation is transformed into an amplitude modulation which is detected by the lock-in amplifier. As such, the modulated change of focusing properties can cause a spurious background signal in SRS microscopy. Using a condenser with numerical aperture (NA=1.4) higher than that of the excitation objective (N.A.=1.2) and a large area photodiode in order to collect all the light from the sample minimize this effect (Freudiger et al., 2008). However, in strongly scattering samples, this is not always possible and XPM cannot always be fully suppressed.

In OHD-RIKE microscopy, probing the resonant response (i.e. the imaginary part) of the sample,

the same process can also cause spurious background signal proportional to $\mathrm{Re}\left(\chi^{(3)}_{1122} \pm \chi^{(3)}_{1212}\right)$. However, off vibrational resonance, $\chi^{(3)}_{1122} = \chi^{(3)}_{1212} = \chi^{(3)}_{1221} = \frac{1}{3}\chi^{(3)}_{1111}$ according to Kleinmann symmetry (Levenson and Kano, 1982). Thus circular OHD-RIKE should be free of spurious background signal from XPM as $\mathrm{Re}\left(\chi^{(3)}_{1122} - \chi^{(3)}_{1212}\right) = 0$.

In principle, this allows for a higher sensitivity than SRS, as laser noise scales with the spurious background signal introduced by XPM. However it turns out that OHD-RIKE microscopy suffers from similar limitations as P-CARS and I-CARS microscopy for the imaging of complex biological samples, which is the inherent loss of polarization and the inability to maintain a fixed phase relationship of emitted homodyne field and local oscillator in heterogeneous and potentially birefringent samples. As such, the theoretical sensitivity advantages of RIKE compared to SRS are difficult to realize in practice in microscopy.

1.4 Conclusion

Coherent Raman techniques CARS, SRS and RIKE are reviewed here. SRS is a unique contrast for microscopy of biological samples. It is a heterodyne detection scheme, thus overcomes the problems associated with homodyne-detected CARS, (such as the limited sensitivity due to the non-resonant background, spectral distortion, coherent image artifacts and non-linear concentration dependence) the homodyne field and local oscillator are intrinsically synchronized as they have the same optical frequency and polarization. Although OHD-RIKE might suppress cross phase modulation that still exists in SRS, the realization of the suppression in practice is very difficult to achieve, which also complicates the experimental implementation and compromises signal level. Therefore SRS remains to be the best option for coherent Raman imaging.

References

Begley, R.F., Harvey, A.B., Byer, R.L. (1974).Coherent anti-Stokes Raman spectroscopy. Applied Physics Letters. Vol.25, No.7.

Betzig, E. et al. (2006). Imaging Intracellular Fluorescent Proteins at Nanometer Resolution. Science 313(5793): 1642–1645.

Bloembergen, N. (1992) Nonlinear Optics. Addison-Wesley, USA.

Boyd, R. W. (1980).J Opt Soc A, 70, 877.

Boyd, R. W. (2008) Nonlinear Optics. Elsevier, London.

Chalfie, M., Tu, Y., Euskirchen, G., Ward, W.W., Prasher, D.C. (1994). Green fluorescent protein as a marker for gene expression. Science 263:802–5.

Cheng, J. X., Book, L. D., Xie, X. S. (2001). *Opt Lett 26*, 1341.

Cheng, J., Xie, S. X. (2004). Coherent Anti-Stokes Raman Scattering Microscopy: Instrumentation, Theory and Applications. J.Phys.Chem.B,108,827-840.

Cui, M. (2009). Coherent Raman scattering: applications in imaging and sensing. The University of Michigan.

Dao, T.L., Georges, A., Dalibard, J., Salomon, C., Carusotto, I. (2007). Measuring the one-particle excitations of ultracold fermionic atoms by stimulated Raman spectroscopy. Phys.Rev.Letters, 98,240402.

Denk W, Strickler J, Webb WW. (1990). Two-photon laser scanning fluorescence microscopy. Science 248:73–76

Eesley, G.L. (1979) J.Quant.Spectrosc.Radiat.Transfer Vol.22, pp.507-576.

Ekvall, K., van der Meulen, P., Dhollande, C.; Berg, L. E., Pommeret, S., Naskrecki, R., Mialocq, J. C. (2000). J. Appl. Phys. *87*, 5.

Freudiger, C. W., Min, W., Saar, B. G., Lu, S., Holtom, G. R., He, C. W., Tsai, J. C., Kang, J. X., Xie, X. S. (2008) Science, 322, 1857.

Giraud, G., Gordon, C.M., Dunkin, I.R., Wynne, K. (2003). The effects of anion and cation substitution on the ultrafast solvent dynamics of ionic liquids: A time-resolved optical Kerr-effect spectroscopic study. Journal of Chemical Physics, Vol.119, No.1.

Giraud, G., Karolin, J., Wynne, K. (2003). Low-frequency modes of peptides and globular proteins in solution observed by ultrafast OHD-RIKES spectroscopy. Biophysical Jounal, Vol.85, 1903-1913.

Heiman, D., Hellwarth, R.W., Levenson, M.D., Martin, F. (1976). Raman-Induced Kerr effect. Physical Review Letters, Vol.36, No.4.

Hell SW. (2007). Far-field optical nanoscopy. Science 316:1153–58.

Hyun, B., Dzyuba, S.V., Bartsch, R.A., Quitevis, E.L. (2002). Intermolecular dynamics of roo-temperature ionic liquids: femtosecond optical Kerr effect measurements on 1-Alkyl-3-methylimidazolium Bis imides. J.Phys.Chem.A,106,7579-7585.

Hyun, B.R., Quitevis, E.L. (2003). Intermolecular spectrum of 4-octyl-4'-cyanobiphenyl in n-heptane: OHD-RIKES measurements. Chemical Physics Letters,373,526-531.

Knutsen, K.P., Johnson, J.C., Miller, A.E., Petersen, P.B., Saykally, R.J. (2004). High spectral resolution multiplex CARS spectroscopy using chirped pulses. Chemical Physics Letters, 387,436-441.

Kukura, P., McCamant, D.W., Yoon, S., Wandschneider, D.B., Mathies, R.A. (2005). Structural observations of the primary isomerization in vision with femtosecond-stimulated Raman. Science,310,1006.

Levenson, M.D., Kano, S.S.(1982). Introduction to nonlinear laser spectroscopy. Academic Press, New York.

Mallick, B., Lakshmanna, A., Radhalakshmi, V., Umapathy, S. (2008). Design and development of stimulated Raman spectroscopy apparatus using a femtosecond laser system. Current Science, Vol.95, No.11.

Maker, P.D., Terhune, R.W. (1965). Study of optical effects due to an induced polarization third order in electric field strength. Physical Review, 137(3A):801-819.

Mills, D.L.(1991) Nonlinear Optics: Basic concepts. Springer-Verlag Berlin Heidelberg,New York.

Moerner WE, Orrit M. (1999). Illuminating single molecules in condensed matter. Science 283:1670–76 9.

Mukamel, S. (1995). Principles of nonlinear optical spectroscopy. Oxford University Press, New York.

Pawley, J. B. (2006). Handbook of Biological Confocal Microscopy. New York: Springer. 3rd ed.

Pestov, D., Murawski, R.K., Ariunbold, G.O., Wang, X., Zhi, M., Sokolov, A.V., Sautenkov,

V.A., Rostovtsev, Y.V., Dogariu, A., Huang, Y., et al. (2007). Optimizing the laser-pulse configuration for coherent Raman spectroscopy. Science 316, 265-268.

Raman, C.V.; Krishnan, K.S. (1928). The optical analog of Compton effect. Nature, 121, 711.

Rust, M.; M. Bates; X. Zhuang (2006). "Sub-diffraction-limit imaging by stochastic optical reconstruction microscopy (STORM)". Nature Methods 3 (10): 793–796.

Saleh, B. E. A., Teich, M. C. (1991).Fundamentals of Photoncis; John Wiley & Sons inc.: New York.

Stefan W. Hell and Jan Wichmann (1994). "Breaking the diffraction resolution limit by stimulated emission: stimulated-emission-depletion fluorescence microscopy". Optics Letters19 (11): 780–2.

Tu, A. T. (1982) Raman spectroscopy in biology. John Wiley& Sons, New York.

Turrell, G.; Corset, J. (1996). J. Raman Microscopy: Developments and Applications; Academic Press: San Diego, CA.

Wang, C.S. (1969). Theory of stimulated Raman scattering. Physical Review, 182(2):482- 494.

Wynne, K. (2005). A new ultrafast technique for measuring the terahertz dynamics of chiral molecules: the theory of optical heterodyne-detected Raman-induced Kerr optical activity. J.Chem.Phys, 122, 244503.

Xie XS, Trautman JK. (1998). Optical studies of single molecules at room temperature. Annu. Rev. Phys. Chem. 49:441–80.

Yu, Y., Zhou, G., Lin, K., Dai, H., Lin, L., Ma, X. (2006). The comparison of RIKES and PARS in measuring the spectrum of CH_4. Acta Physica Sinica, Vol.55, No.6.

Zhang, J., Campbell, R.E., Ting, A.Y., Tsien, R.Y. (2002). Creating new fluorescent probes for cell biology. Nat. Rev. Mol. Biol. 3:906–18.

Chapter 2

SRS imaging of Nucleic Acids in Live Cells

Imaging of nucleic acids is important for studying cellular processes such as cell division and apoptosis. A noninvasive label-free technique is attractive. Raman spectroscopy provides rich chemical information based on specific vibrational peaks. However, the signal from spontaneous Raman scattering is weak and long integration times are required, which drastically limits the imaging speed when used for microscopy. Coherent Raman scattering techniques, comprising coherent anti-Stokes Raman scattering (CARS) and stimulated Raman scattering (SRS) microscopy, overcome this problem by enhancing the signal level by up to five orders of magnitude. CARS microscopy suffers from a nonresonant background signal, which distorts Raman spectra and limits sensitivity. This makes CARS imaging of weak transitions in spectrally congested regions challenging. This is especially the case in the fingerprint region, where nucleic acids show characteristic peaks. The recently developed SRS microscopy is free from these limitations; excitation spectra are identical to those of spontaneous Raman and sensitivity is close to shot-noise limited. Herein we demonstrate the use of SRS imaging in the fingerprint region to map the distribution of nucleic acids in addition to proteins and lipids in single salivary gland cells of Drosophila larvae, and in single mammalian cells. This allows the imaging of DNA condensation associated with cell division and opens up possibilities of imaging such processes in vivo.

Contributions

The work in this chapter involved close collaboration with Dr. Maarteen Roeffers and Dr. Srinjan Basu. I, Dr. Roeffers and Prof. Xie conceived the idea and designed the experiments. I and Dr. Roeffers performed the imaging experiments and conducted image analysis. Dr. Basu prepared mammalian cells. Dr. Joseph R. Daniele prepared salivary gland cells of Drosophila Melanogaster. Dr. Dan Fu, Dr. Christian Freudiger and Dr. Gary Holtom helped with technical discussion.

2.1 Background

As discussed in Chapter 1, spontaneous Raman scattering has very weak signals, so a long integration time is required to achieve a good signal to noise ratio (SNR) (Kraft et al., 2009; Fujita and Smith, 2008; Swain and Stevens, 2007). This is not ideal for live cell imaging because biological dynamics generally occur at shorter time scales.Coherent Raman scattering techniques such as Coherent anti-Stokes Raman scattering (CARS) (Zumbusch and Xie, 1999; Evans et al., 2005; Evans and Xie, 2008; Rinia et a., 2006; Ganikhanov et al., 2006) and Stimulated Raman scattering (SRS) (Ploetz et al., 2007; Freudiger et al., 2008; Ozeki et al., 2009; Nandakumar et al., 2009; Saar et al., 2010) can increase the speed of Raman imaging by up to 5 orders of magnitude. However, CARS microscopy contains a nonresonant background which distorts the Raman spectra (Evans and Xie, 2008) and limits the sensitivity (Rinia et al., 2006). This is particularly problematic when imaging below 1800 cm^{-1}, the vibrational fingerprint region, because this region has many neighboring peaks and these peaks have low intensities. Although CARS microspectroscopy with maximum entropy method (MEM) analyses has been used to circumvent this problem (Okuno et al., 2010), it is fair to say that CARS microscopy to date has focused predominantly on the chemical imaging of C-H vibrations (Evans and Xie, 2008). SRS

microscopy is free from the nonresonant background and spectral distortion and the signal is linearly proportional to the target molecule concentration and offers easy explanation of imaging contrast. SRS microscopy is particularly suited for imaging in the fingerprint region.

Imaging of nucleic acids, which have vibrations within the fingerprint region, has not been shown with SRS microscopy because of its much weaker signal than lipids. Nucleic acid distributions are important for studying cellular processes such as cell division or apoptosis. The ability to detect these processes is useful for screening chemicals during drug discovery and for monitoring the growth of engineered tissues (Notingher, 2006). In this study, we demonstrate SRS imaging of the distribution of nucleic acids in living cells in addition to lipids and proteins. We show live cell imaging of single polytene chromosomes within the salivary glands of the fruit fly (Drosophila melanogaster), as well as imaging of two mammalian cell lines: human embryonic kidney cells (HEK-293) and breast cancer cells (MCF-7).

2.2 Results and Discussion

2.2.1 Assignment of Raman Resonance Peaks

Lipid, protein and nucleic acids are major biochemical components of a cell. They all have specific Raman peaks, many of which are within the fingerprint region. The vibrational modes used in this study are listed in Table 2.1 (Thomas et al., 1977; Goodwin and Brahms, 1978; Benevides and Tohomas, 1983; Prescott et al., 1984; Savoie et al., 1985; Thomas, 1999; Parker, 1983; Gelder et al., 2007; Roeffaers et al., 2011). The Raman peaks for nucleic acids, protein and lipid are confirmed using a confocal laser Raman spectrometer (Labram HR800, Horiba Jobin Yvon).

Table 2.1 Raman peak assignment of different chemical bonds.

Raman peaks [cm^{-1}]	Functional group	Chemical species
783–790	symmetric phosphodiester stretch ring breathing modes of pyrimidine bases	nucleic acids
1090–1010	symmetric dioxy stretch of the phosphate backbone ν (C-C)	nucleic acids lipid
1655	amide I ν (C=O) ν (C=C)	protein unsaturated lipid
1004	phenylalanine	protein
2845	ν (CH2)	lipid

Figure 2.1a shows the Raman spectrum of a deoxyribonucleic acid (DNA) fiber extracted from salmon testes. The peak at 785cm^{-1} originates from the superposition of the symmetric phosphodiester stretch and the ring breathing modes of the pyrimidine bases, and the peak at 1099 cm^{-1} originates from the symmetric dioxy-stretch of the phosphate backbone (Goodwin and

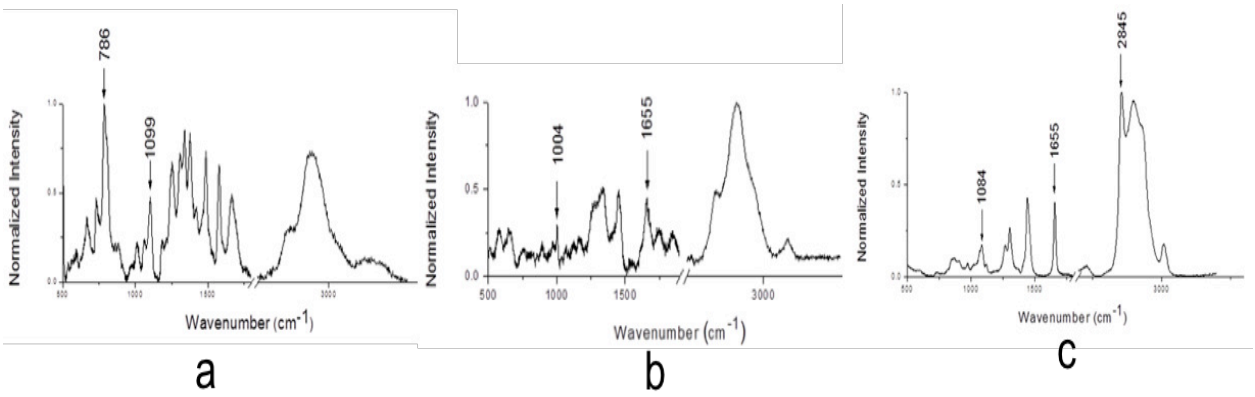

Figure 2.1. Raman spectra of (a) DNA, (b) BSA and (c) Oleic Acid.

Brahms, 1978). Figure 2.1b shows the Raman spectrum of bovine serum albumin (BSA) powder which is a protein. The peak at 1004 cm^{-1} originates from the ring-breathing mode of phenylalanine in the protein (Roeffaers et al., 2011). Another peak at 1655 cm^{-1} originates from the Amide I band of the protein. Figure 2.1c shows the Raman spectrum of oleic acid which represents unsaturated lipid. The peak at 2845 cm^{-1} originates from paraffinic C-H vibrations. Another peak at 1655 cm^{-1} originates from the C=C vibrations of unsaturated lipids, which overlaps with the Amide I band of protein. The peak at 1084 cm^{-1} originates from the skeletal C-C vibrations which may interfere with the 1099 cm^{-1} peak of nucleic acids. These peaks are within the range of those observed previously (See Table 2.1).

2.2.2 SRS imaging of single polytene chromosomes in the salivary gland cells of Drosophila melanogaster

Since the Raman signal of nucleic acids is very weak compared to that of lipids and proteins, the first cellular system in this study is the salivary gland cells in Drosophila melanogaster larvae because of their unusually high DNA concentration: each cell contains 100-500 DNA copies.

Based on the spontaneous Raman spectra from these cells (Figure 2.1a), four peaks were selected for SRS imaging: 1) the peak at 2845cm^{-1} attributed to the CH_2 vibration in lipids, 2) the peak at 1655cm^{-1} attributed to the amide I band of proteins and 3)&4) two peaks in the fingerprint region that are attributed to nucleic acids being the resonance at 785 cm^{-1} and 1090 cm^{-1} (See Table 2.1).

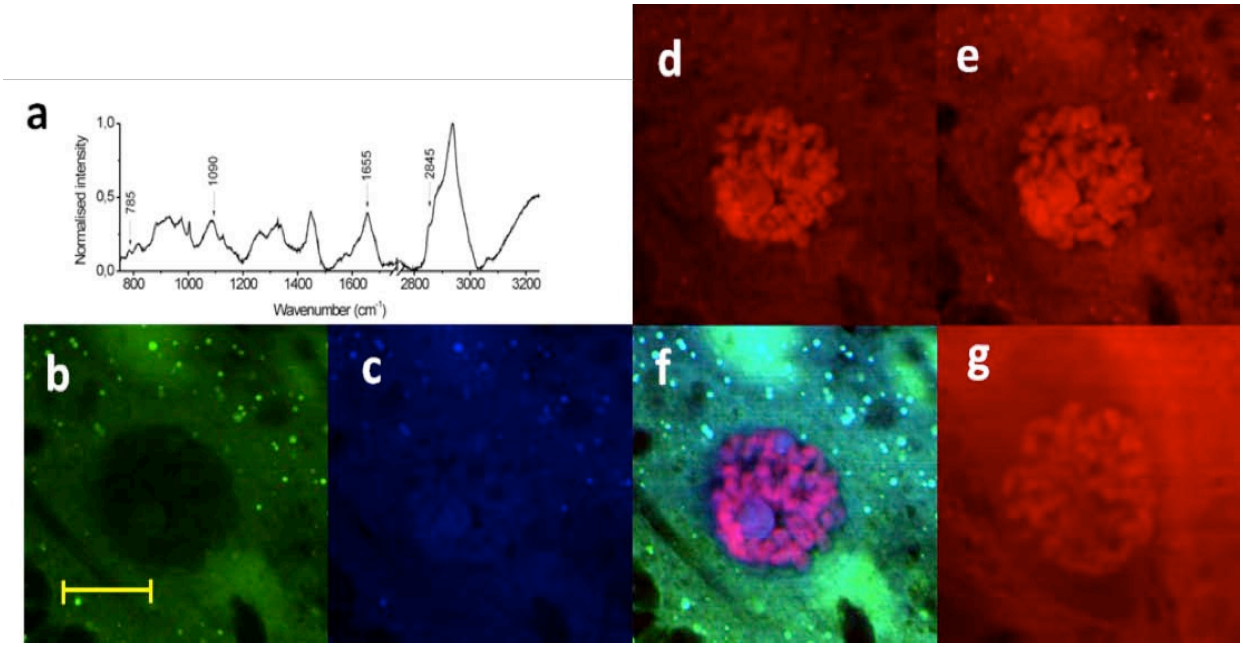

Figure 2.2 (a) Raman spectrum of a Drosophila cell (b)-(g) SRS images of a salivary gland cell from Drosophila melanogaster, via the stimulated Raman loss detection scheme. (b) Lipid specific image taken at 2845 cm^{-1}, (c) Amide I band at 1655 cm^{-1} (d) nucleic acids at 785 cm^{-1} and (e) 1090 cm^{-1}. (f) multicolor image generated by combining images (b)-(e). (g) Nucleic acid map recorded at 785 cm^{-1} via the stimulated Raman gain detection scheme. Scale bar is 20 µm. Each image has a size of 512 x 512 pixels.

Figure 2.2b-f shows the SRS imaging of salivary gland cells in Drosophila melanogaster larvae at different Raman resonances. The image at 2845 cm^{-1} shows small lipid droplets that are visible as bright dots. The nucleus shows up as a dark zone due to its lack of lipids. The amide I channel measured at 1655 cm^{-1} shows a more homogeneous distribution since both the nucleus and the cytoplasm contain a large amount of protein. However, the C=C vibration in unsaturated lipid also has contribution to this channel due to its Raman peak at 1655 cm^{-1} (See Table 2.1). The bright dots in this channel mainly come from the lipid droplets in the cytoplasm.

The specific structure of the polytene DNA in the nucleus, which consists of multiple copies of tightly bound sister chromosomes, shows up at 785cm^{-1} and 1090 cm^{-1}. The typical banding structure called "puffing" (Ashburner, 1972) is clearly resolved (Figure 2.3). The specific structure arises from transcriptionally-inactive, compacted regions of the chromosome called heterochromatin and gene-rich transcriptionally-active regions of the chromosome called euchromatin. Heterochromatin has higher DNA concentration compared to euchromatin.

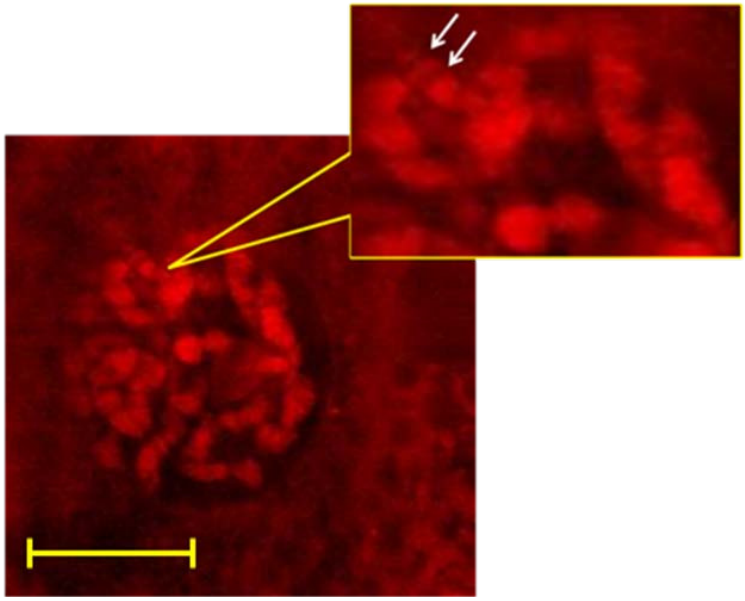

Figure 2.3 The zoomed in image of a polytene chromosome where the typical banding pattern is observed. The arrows highlight euchromatin. The image is taken at 785cm^{-1}, nucleic acid. Scale bar is 20 µm.

It is worth noting that the fingerprint region of Raman spectra consists of several closely packed vibrational resonances. It is also reflected in our SRS images. For example, the 1090 cm^{-1} peak is amidst the abundant C-C vibrational resonance. This could explain the elevated signal in the lipid droplets in the cytoplasm. However, there is no contribution from C-C in 785cm^{-1}, but there is still a background signal in the cytoplasm in this channel. This signal can, at least in part, be attributed to the presence of large amounts of RNA because of the similarity between DNA

and RNA Raman spectra.

One likely imaging artifact, cross phase modulation (XPM) (Ekvall et al., 2000; Freudiger et al., 2011), could also give rise to this signal, but we ruled out this possibility by comparing images taken with SRL and SRG detection schemes. XPM could contribute to the signal when the modulated Stokes beam intensity causes a modulation in the refractive index in focus due to the Kerr effect, therefore resulting in a modulation of the divergence of the transmitted pump beam. This divergence modulation can be transformed into amplitude modulation when the detection numerical aperture (NA) or the detector size is limited. In that case, it will be detected as a modulated loss in pump beam intensity. Obviously the signal size would depend on the detection geometry and becomes more significant when the detection NA is too small. In addition, the phase of the signal should be the same in both the SRL and the SRG detection configurations. Therefore XPM shows positive signal in SRL but negative signal in SRG. This allows us to distinguish XPM from SRS signal. This phenomenon is confirmed by placing a pinhole in front of the detector to reduce the collection NA and measuring the XPM signal from water (off resonance of the O-H stretching vibration at 2830 cm^{-1}) (Freudiger et al., 2011). By closing down the pinhole, the XPM signal increases in phase with the pump beam in SRL but out of phase with the Stokes beam in SRG.

Figure 2.2g shows the SRG images taken in salivary gland cells in Drosophila larvae. As discussed above, XPM should in principle show a negative signal in the SRG detection scheme. However, there is still positive background signal in the cytoplasm. We therefore conclude that the background in the cytoplasm comes mainly from the Raman signal of RNA and Raman background from other species, and not from XPM.

The merged image of the lipid, protein and nucleic acid channels (Figure 2.2f) shows a strong correlation between nucleic acids and protein resulting in a pink colored polytene chromosome in which proteins not only serve as organizational units, but also fulfill an important function in gene transcription and other nuclear processes.

2.2.3 Determining the cell cycle phase of mammalian cells using SRS imaging

Having demonstrated the detectability of single polytene chromosomes using SRS imaging, the technique was also applied to single mammalian cells that have much lower DNA concentration. Based on the spontaneous Raman spectra of HEK293 cells (Figure 2.1a), three peaks were selected at 2845 cm^{-1}, 785 cm^{-1} and 1090 cm^{-1} for imaging lipids and nucleic acids (as in section 2.2.1). To image the protein distribution, a different peak was selected at 1004 cm^{-1}, since there is interference at 1655 cm^{-1} from unsaturated lipid(as shown in Table 2.1). The peak at 1004 cm^{-1} is attributed to the ringbreathing mode of phenylalanine.

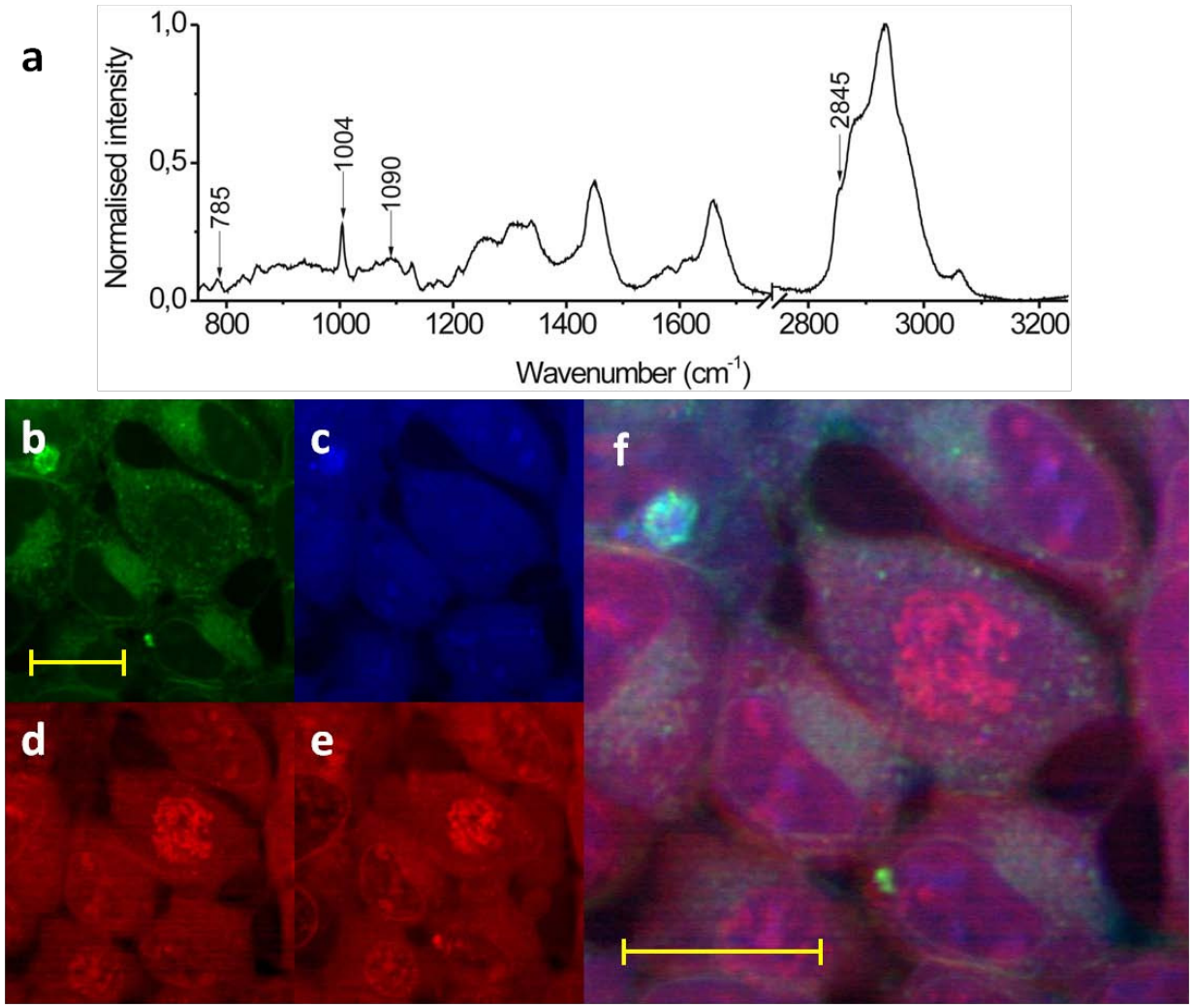

Figure 2.4 (a) Raman spectrum of a HEK-293 cell pellet. (b)-(f) SRS images of HEK-293 cells at (b) 2845 cm^{-1}, primarily lipid (c) 1004cm^{-1}, phenylalanine (d) 785 cm^{-1}, nucleic acid (e) 1090 cm^{-1}, primarily nucleic acid. (f) multicolor overlay of (b),(c),(d). Scale bar is 20 μm.

Figure 2.4 shows the SRS biomolecular maps of HEK-293 cells. The same dark zone as shown before is observed in the nucleus at 2845 cm^{-1} (the lipid channel in Figure 2.4b) and lipid droplets are visible in the cytoplasm. The protein channel shows signal in both the nucleus and the cytoplasm (Figure 2.4c). Figure 9d-e show that we can detect nucleic acids, which are enriched in some cell nuclei. However cell-to-cell variation is observed. The signal level is 2-5 times lower than that in salivary gland cells.

Similar biomolecular maps are also observed in another mammalian cell line (MCF-7) (Figure 2.5).

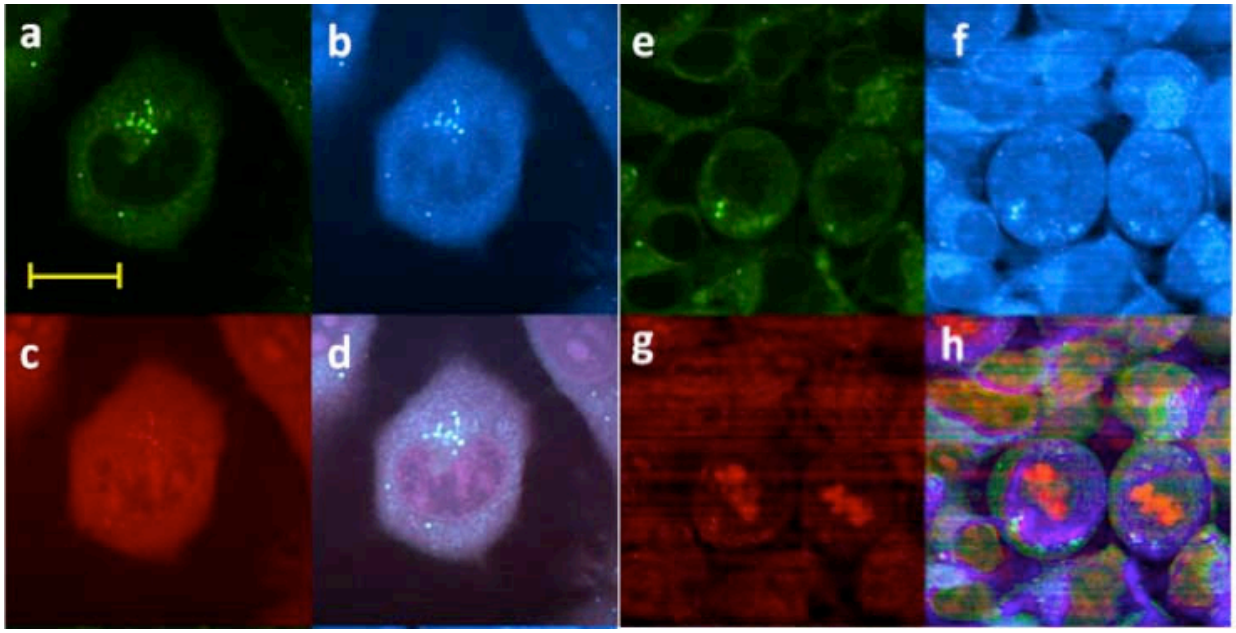

Figure 2.5 SRS images of MCF-7 cells at (a) 2845 cm^{-1}, primarily lipid (b) 1655cm^{-1}, primarily protein (c) 785cm^{-1}, nucleic acid, and (d)overlay of (a)-(c). SRS images of a few other MCF-7 cells at (e) 2845 cm^{-1}, (f) 1655cm^{-1}, (g) 785cm^{-1} and (h) overlay of (e)-(g). Scale bar is 20 μm.

The cell-to-cell variations observed in the nucleic acid channel are attributed to differences between metaphase cells from interphase cells. When the cell is in interphase (Figure 2.5a-d), there is increased signal in the nucleolus, a region within the nucleus with high levels of ribosomal RNA production and hence a higher nucleic acid concentration. It is also possible to observe when the cell is undergoing stages of cell division. For example, some cells show increased contrast within the nucleus (Figure 2.5d-e) because they are in prophase (the stage at which DNA condenses before cell division). Some cells show increased signal lining up along one axis of the nucleus (Figure 2.5g) and are in metaphase (the stage at which condensed chromosomes line up in the middle of the cell before they separate into daughter cells). Such information allows us to distinguish cells that are dividing from cells that are not.

Fluorescent staining of DNA using a live cell dye was used to confirm that the nucleic acid enrichment in the nucleus correlated with an enrichment of dye labeled DNA (Figure 2.6). Furthermore, the specificity of the signal was demonstrated by imaging 15 cm^{-1} away from the resonant peak (Figure 2.7).

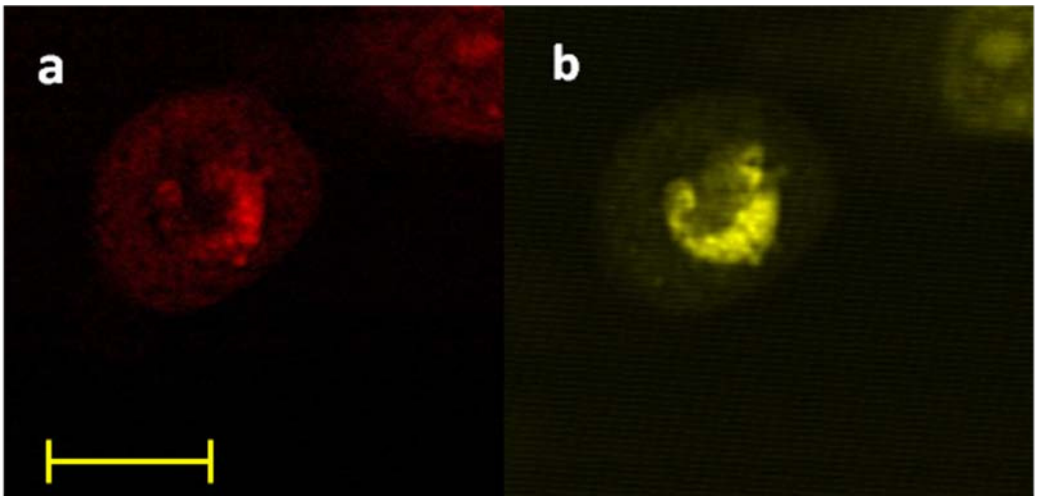

Figure 2.6 (a) The SRS image of a MCF-7 cell at 1090 cm^{-1} , primarily nucleic acid (subtracted from off-resonace image). (b) The two photon fluorescence image of a MCF- 7 cell labeled with syto11 dye. Scale bar is 20 µm.

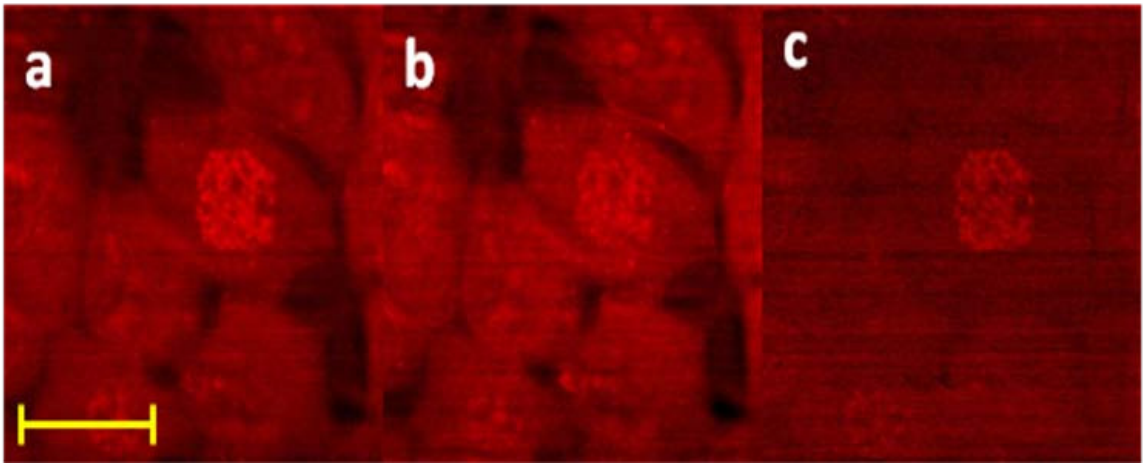

Figure 2.7 SRS images of HEK-293 at (a) 785ccm^{-1}, (b) 770 cm^{-1} . (c) The subtracted image of (a) from (b). Scale bar is 20 µm

2.3 Methods and Materials

2.3.1 Imaging Instrumentation

SRS is implemented with high frequency modulation excitation and high frequency phase sensitive detection scheme (Figure 2.8). Two excitation beams with the frequency difference matching the vibrational frequency of targeted molecules are utilized. The Stokes beam is provided by a 1064 nm Nd:YVO_4 laser (picoTRAIN, High-Q, Germany) which delivers a 6 ps pulse train at a 76 MHz repetition rate. The pump beam is provided by the signal output of an optical parametric oscillator (OPO) (Levante Emerald, APE-Berlin, Berlin, Germany) synchronously pumped by the frequency doubled Nd:YVO_4 laser at 532 nm. The wavelength of the pump beam can be tuned between 680 nm and 1010 nm.

The pump beam and the modulated Stokes beam are spatially overlapped using a dichroic mirror (1064DCRB, Chroma Technology, Bellow Falls, Vermont) and also temporally overlapped by adjusting a manual delay stage.

After transmission through an upright Olympus laser-scanning microscope (BX61WI/FV300, Olympus, Pittsburgh, Pennsylvania), the excitation beams are focused onto the sample by a water immersion objective (UPlanApo/IR 60×/1.2 NA Olympus). A 1.45 NA oil immersion condenser is used to collect the transmitted light. A high NA condenser is used to reduce a potential artifact coming from cross phase modulation (XPM).

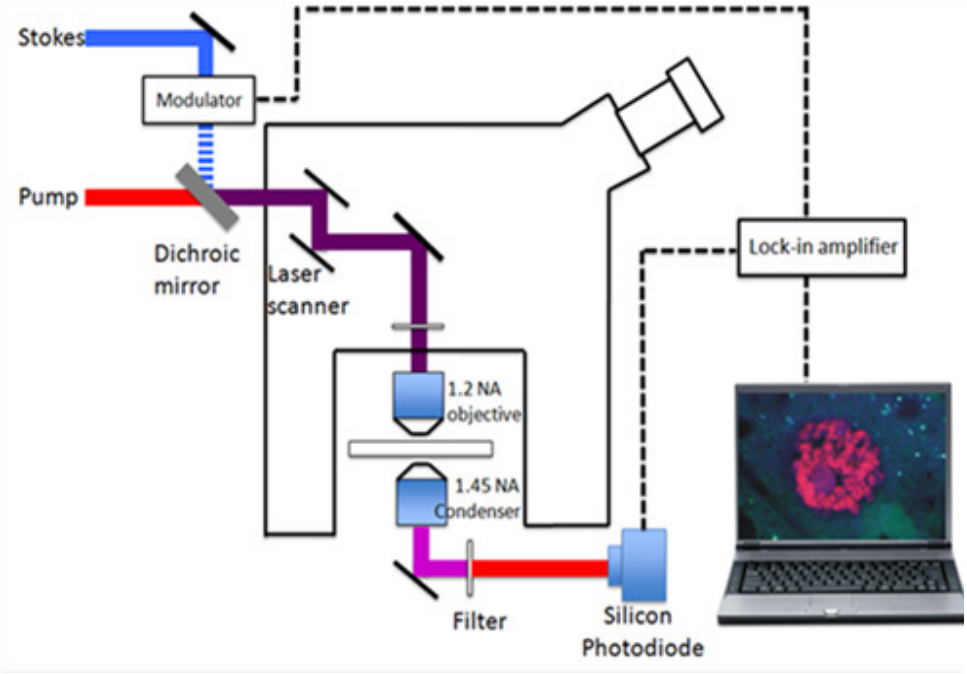

Figure 2.8 Experimental schematic of stimulated Raman loss (SRL) microscope. For SRG, the pump beam is modulated instead of the Stokes beam and an InGaAs photodetector is used instead of a silicon photodetector because of its better responsivity at 1064 nm.

In the SRS process, an increase in the intensity of the Stokes beam (stimulated Raman gain) occurs along with the decrease in the intensity of the pump beam (stimulated Raman loss). Since the intensity change is minute compared to the excitation beam intensity and can be buried within the laser noise, high frequency intensity modulation at 10.4 MHz is applied to one of the excitation beams so that the SRS signal can be separated from the laser noise, which occurs at much lower frequencies, using lock-in detection (SR844RF, Stanford Research Systems, Sunnyvale, California). In the stimulated Raman loss detection scheme (Figure 2.9a), the Stokes beam is modulated at 10.4 MHz and the transmitted pump beam is detected using a 1 cm^2 silicon photodiode with a reverse bias of 64 V to 128 V after filtering out the Stokes beam using a bandpass filter (CARS890/220M, Chroma Technology, Bellow Falls, Vermont). In contrast, in the stimulated Raman gain detection scheme (Figure 2.9b), the pump beam is modulated at 10.4

MHz and the transmitted Stokes beam is detected using a 4 mm^2 InGaAs photodetector with reversed bias of 10 V after filtering out the pump beam using a longpass filter (FEL1050, Thorlabs, Newton, New Jersey). Different detectors are chosen according to their wavelength-dependent responsivity.

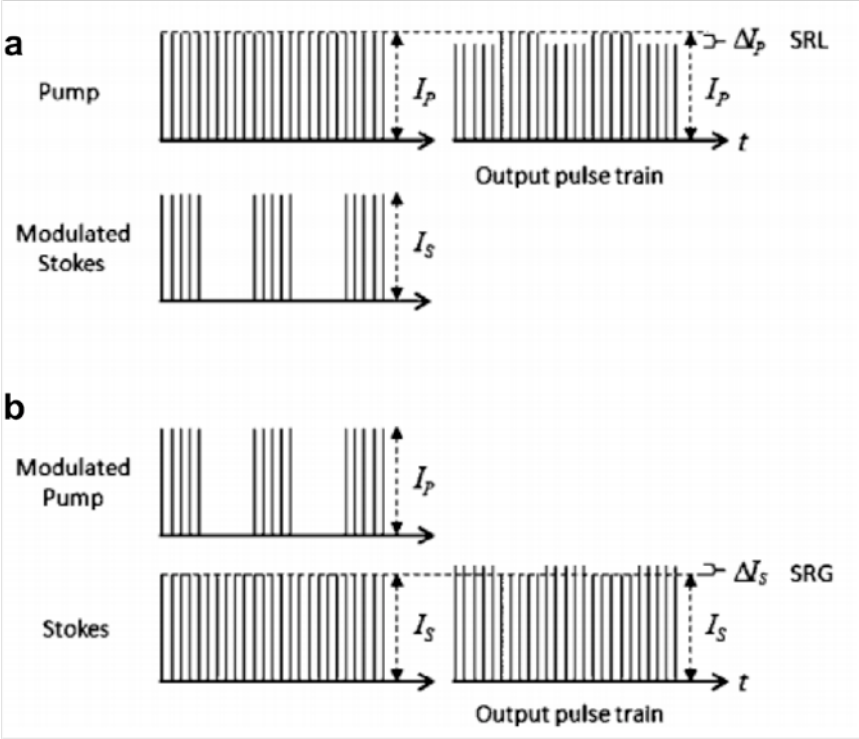

Figure 2.9 (a) Detection scheme of SRL. Stokes beam is modulated at 10.4 MHz at which the resulting amplitude modulation of the pump beam due to the stimulated Raman loss can be detected. (b) Detection scheme of SRG. Pump beam is modulated at 10.4 MHz at which the resulting amplitude modulation of the Stokes beam due to the stimulated Raman gain can be detected.

Most images were taken using a stimulated Raman loss (SRL) setup (Figure 2.9a) with a pixel dwell time of 40 µs or 120 µs depending on the signal strength. The imaging speed is mostly limited by the signal intensity. The pump beam intensity ranges from 40mW to 140mW and the Stokes beam intensity ranges from 60mW to 210mW depending on the signal strength of the target species. Figure 2.2g was taken using a stimulated Raman gain (SRG) setup, which was discussed in detail in section 2.2.2.

2.3.2 Sample Preparation

MCF7 and HEK-293 cell lines (ATCC) were maintained at 37°C in a humidified 5% CO_2 air incubator. HEK-293 cells were cultured in DMEM (Invitrogen) supplemented with 10 % fetal bovine serum (Sigma). MCF7 cells were cultured in MEM (Invitrogen) supplemented with 10 % fetal bovine serum and 0.01 mg/ml insulin (Sigma). Cells were imaged in phenol red-free growth medium. Polytene chromosomes in Drosophila salivary glands were imaged directly in live fly larvae. The samples were placed between a mounting glass slide and a No.1 coverslip (VWR,Radnor, Pennsylvania) and sealed with nail polisher. The experiments were performed at room temperature.

2.3.3 Spontaneous Raman Spectroscopy

The spontaneous Raman spectra were acquired using a confocal laser Raman spectrometer (Labram HR800, Horiba Jobin Yvon) at room temperature. A 10 mW 633 nm HeNe laser was used to excite the sample through a 50x, 0.75 NA objective (MPlan N, Olympus). A polychromator with 600 lines / mm was used to disperse the light onto the CCD camera. The total data acquisition was performed during 40 seconds and the background was subtracted using the LabSpec software.

2.4. Conclusions

We have demonstrated that SRS microscopy can be used as a non-invasive label-free imaging tool for the quantitative mapping not only of protein and lipid distributions but also of the nucleic acids distribution. The SRS images of different cellular components have been shown in single salivary gland cells of Drosophila larvae, as well as in single HEK293 and MCF7 cells. We detected differences in the nucleic acid signal when comparing heterochromatin and euchromatin

within these cells. In the case of the fruit fly, we demonstrated that we can detect the banding pattern of polytene chromosomes that is known to arise from alternating regions of heterochromatin and euchromatin. In the case of mammalian cells, we determine whether or not a cell is dividing through the detection of a nucleolus present in non-dividing cells during interphase and the increased levels of DNA condensation that occur in dividing cells. In this study, we show that it is possible to detect cell division through imaging of DNA. This technique may be important in identifying cells undergoing cell division or apoptosis within living tissue, making it possible to study diseases such as cancer.

References

Ashburne.M (1972). Patterns of Puffing Activity in Salivary-Gland Chromosomes of Drosophila .6. Induction by Ecdysone in Salivary-Glands of D-Melanogaster Cultured in-Vitro. Chromosoma 38, 255-&.

Benevides, J.M., and Thomas, G.J. (1983). Characterization of DNA Structures by Raman-Spectroscopy - High-Salt and Low-Salt Forms of Double Helical Poly(Dg-Dc) in H2o and D2o Solutions and Application to B-DNA, Z-DNA and a-DNA. Nucleic Acids Res 11, 5747-5761.

De Gelder, J., De Gussem, K., Vandenabeele, P., and Moens, L. (2007). Reference database of Raman spectra of biological molecules. J Raman Spectrosc 38, 1133-1147.

Ekvall, K., van der Meulen, P., Dhollande, C., Berg, L.E., Pommeret, S., Naskrecki, R., and Mialocq, J.C. (2000). Cross phase modulation artifact in liquid phase transient absorption spectroscopy. J Appl Phys 87, 2340-2352.

Evans, C.L., Potma, E.O., Puoris'haag, M., Cote, D., Lin, C.P., and Xie, X.S. (2005). Chemical imaging of tissue in vivo with video-rate coherent anti-Stokes Raman scattering microscopy. Proceedings of the National Academy of Sciences of the United States of America 102, 16807-16812.

Evans, C.L., and Xie, X.S. (2008). Coherent Anti-Stokes Raman Scattering Microscopy: Chemical Imaging for Biology and Medicine. Annu Rev Anal Chem 1, 883-909.

Fujita, K., and Smith, N.I. (2008). Label-free molecular imaging of living cells. Molecules and cells 26, 530-535.

Freudiger, C.W., Min, W., Saar, B.G., Lu, S., Holtom, G.R., He, C.W., Tsai, J.C., Kang, J.X., and Xie, X.S. (2008). Label-Free Biomedical Imaging with High Sensitivity by Stimulated Raman Scattering Microscopy. Science 322, 1857-1861.

Freudiger, C.W., Roeffaers, M.B.J., Zhang, X., Saar, B.G., Min, W., and Xie, X.S. (2011). Optical Heterodyne-Detected Raman-Induced Kerr Effect (OHD-RIKE) Microscopy. J Phys Chem B 115, 5574-5581.

Ganikhanov, F., Evans, C.L., Saar, B.G., and Xie, X.S. (2006). High-sensitivity vibrational imaging with frequency modulation coherent anti-Stokes Raman scattering (FM CARS) microscopy. Optics letters 31, 1872-1874.

Goodwin, D.C., and Brahms, J. (1978). Form of DNA and Nature of Interactions with Proteins in Chromatin. Nucleic

Krafft, C., Dietzek, B., and Popp, J. (2009). Raman and CARS microspectroscopy of cells and tissues. The Analyst 134, 1046-1057.

Nandakumar, P., Kovalev, A., and Volkmer, A. (2009). Vibrational imaging based on stimulated Raman scattering microscopy. New J Phys 11.

Notingher, I., and Hench, L.L. (2006). Raman microspectroscopy: a noninvasive tool for studies of individual living cells in vitro. Expert Rev Med Devic 3, 215-234.

Okuno, M., Kano, H., Leproux, P., Couderc, V., Day, J.P.R., Bonn, M., and Hamaguchi, H. (2010). Quantitative CARS Molecular Fingerprinting of Single Living Cells with the Use of the Maximum Entropy Method. Angew Chem Int Edit 49, 6773-6777.

Ozeki, Y., Dake, F., Kajiyama, S., Fukui, K., and Itoh, K. (2009). Analysis and experimental assessment of the sensitivity of stimulated Raman scattering microscopy. Optics express 17, 3651-3658.

Parker, F. S. (1983). Applications of Infrared, Raman and Resonance Raman Spectroscopy in Biochemistry, Plenum Press, New York.

Ploetz, E., Laimgruber, S., Berner, S., Zinth, W., and Gilch, P. (2007). Femtosecond stimulated Raman microscopy. Appl Phys B-Lasers O 87, 389-393.

Prescott, B., Steinmetz, W., and Thomas, G.J. (1984). Raman Spectral Studies of Nucleic-Acids .23. Characterization of DNA Structures by Laser Raman-Spectroscopy. Biopolymers 23, 235-256.

Rinia, H.A., Bonn, M., and Muller, M. (2006). Quantitative multiplex CARS spectroscopy in congested spectral regions. J Phys Chem B 110, 4472-4479.

Roeffaers, M.B.J., Zhang, X., Freudiger, C.W., Saar, B.G., van Ruijven, M., van Dalen, G., Xiao, C.H., and Xie, X.S. (2011). Label-free imaging of biomolecules in food products using stimulated Raman microscopy. Journal of biomedical optics 16.

Saar, B.G., Freudiger, C.W., Reichman, J., Stanley, C.M., Holtom, G.R., and Xie, X.S. (2010). Video-Rate Molecular Imaging in Vivo with Stimulated Raman Scattering. Science 330, 1368-1370.

Savoie, R., Jutier, J.J., Alex, S., Nadeau, P., and Lewis, P.N. (1985). Laser Raman-Spectra of Calf Thymus Chromatin and Its Constituents. Biophysical journal 47, 451-459.

Swain, R.J., and Stevens, M.M. (2007). Raman microspectroscopy for non-invasive biochemical analysis of single cells. Biochem Soc T 35, 544-549.

Thomas, G.J. (1999). Raman spectroscopy of protein and nucleic acid assemblies. Annu Rev Bioph Biom 28, 1-+.

Thomas, G.J., Prescott, B., and Olins, D.E. (1977). Secondary Structure of Histones and DNA in Chromatin. Science 197, 385-388.

Zumbusch, A., Holtom, G.R., and Xie, X.S. (1999). Three-dimensional vibrational imaging by coherent anti-Stokes Raman scattering. Phys Rev Lett 82, 4142-4145.

Chapter 3

SRS Imaging of Biomolecules in Multiphasic Food Products

Many food products have multiphasic structures with complex distribution of different molecular content. The texture, quality and even the flavor of food is determined not only by the chemical composition but also by the way that different content molecules are organized at microscopic scale. Like in mayonnaise, an oil-in-water emulsion, the overall properties of the end product are determined not only the total fat/water ratio, but also by the distribution and the size of the lipid droplets. SRS has demonstrated fast label-free imaging capability in mapping the spatial distribution of different molecules. Without nonresonant background as in CARS, SRS generates identical spectra as of spontaneous Raman scattering. This enables SRS to specifically target different molecules with a linear dependence on concentration. Here we demonstrate SRS imaging on several types of solid or liquid multiphasic food products by targeting distinct vibrational modes of different molecules. Imaging based on different vibrational modes of the same molecule and the differentiation between saturated lipid versus nonsaturated lipid are also demonstrated. This approach brings new opportunities to quality screening processes in food production.

Contributions

The work in this chapter involved close collaboration with Dr. Maarteen Roeffers. Dr. Roeffers I, and Prof. Xie conceived the idea and designed the experiments. Dr. Roeffers and I performed the imaging experiments and conducted image analysis. Samples were provided by Dr. Marjolein van Ruijven, Dr.Gerard van Dalen and Dr. Chunhong Xiao from Unilever. Dr. Christian Freudiger and Dr. Brian Saar helped with the technical discussion.

3.1 Background

The sensorial properties of food such as texture and flavor are not only determined by the chemical composition within it but also by how different content molecules are arranged spatially and their interactions (Anguiler, 2005). Moreover, the shelf time or breakdown process during storage also has a structure dependence. Therefore visualizing the microstructure within food product is very important for modern food technology to preserve, transform or destroy the microstructures for engineering towards food with new properties. Optical microscopy is valuable for this purpose because it allows non-destructive imaging with a high spatiotemporal resolution. Fluorescence microscopy is currently the most widely used type of optical microscopy in biomedical research because of its sensitivity and molecular specificity (Pawley, 2006) and visualizing protein/lipid in butter and cheese has been demonstrated (Blonk and Aalst, 1993). However, fluorescence studies require staining or the use of fluorogenic reactants which is not always possible and may even perturb the system under investigation. Recently, significant research effort has been focused on the development of label-free microscopy with chemical contrast. Vibrational spectroscopy, based on infrared absorption or Raman scattering, gives access to a variety of intrinsic molecular signatures, avoiding the need for labeling. Unfortunately, the spatial resolution of infrared microscopy is poor because of the long wavelengths and the penetration into aqueous samples is limited by strong water absorption in the infrared. Raman spectroscopy with visible or near infrared wavelengths offers high resolution in aqueous samples, but the Raman scattering efficiency is extremely low, necessitating high laser power and long integration times to achieve good sensitivity. This limits the detailed observation of microscopic features.

The weak Raman signals can be strongly enhanced by using nonlinear coherent excitation. This makes it possible to image molecular distributions with submicron resolution and imaging speeds up to video rate by targeting isolated vibrational resonances.(Cheng and Xie, 2004; Evans and Xie, 2008). However, the existence of nonresonant background limits the sensitivity of CARS by overwhelming weak resonant signals and distorting the vibrational spectrum through interference. The well isolated CH_2-stretching mode of lipids at 2845 cm^{-1} has been extensively utilized in CARS, but the spectral interference limits the applicability of CARS microscopy to target vibrational signatures in the densely populated fingerprint region. Some advanced CARS-based imaging techniques, like polarization sensitive CARS,(Cheng et al., 2001) time-resolved CARS(Volkmer et al., 2002), interferometric CARS,(Potma et al., 2006) and multiplex CARS(Chen et al., 2002; Vartiainen et al., 2006) have been developed to minimize the non-resonant background. However these techniques either sacrifice signal or require post-processing and do not allow the direct imaging of molecular distributions in complex materials. Raman scattering microscopy does not suffer from the non-resonant background (Freudiger et al., 2008). With the currently available lasers, it is possible to get direct access to a whole range of vibrational frequencies with SRS, including those in the fingerprint region. A major advantage of SRS compared to CARS is that it has the same spectral response as the spontaneous Raman signal even in congested spectral regions and hence enables selective imaging of the different biomolecules like lipids and proteins without the need for data processing. For this study we used different food products which commonly appear as complex multiphasic systems since many organics are not miscible with water (Langton et al., 1999). SRS microscopy is an effective label-free analytical tool to study the distribution and organization of the different constituents in such colloidal systems by specifically targeting the different vibrational modes of molecules at

submicron resolution. Saturated lipid and unsaturated lipid can also be distinctively mapped which cannot be achieved by other label free techniques.

3.2 Results and Discussion

3.2.1 SRS microspectroscopy in mayonnaise

One well known multiphasic food product is mayonnaise, which is an oil-in-water emulsion. The overall properties of the end product are determined not only by the total fat/water ratio, but also by the distribution and the size of the lipid droplets.(Langton et al., 1999; Sadeghijorabchi et al., 1991) The sample used in this study is a full-fat mayonnaise, which contains 77% lipids on a weight basis, of which the large majority (85%) is unsaturated.

First, a traditional spontaneous Raman spectrum was recorded with a total integration time of 40 seconds. Figure 3.1a shows this Raman spectrum of mayonnaise before and after correction for the inherent fluorescence background of the sample. Since mayonnaise largely consists of lipids, it is fairly easy to attribute the major peaks to specific chemical bonds and their vibrational modes (Keller et al., 1993). Most clearly recognizable is the strong Raman signal stemming from the C-H stretching in the region between 2800 – 3050 cm^{-1}. A detailed analysis of this region shows that it consists of several (partially) overlapping bands (Figure 3.1b). In particular, the band around 2845 cm^{-1} originates from paraffinic C-H vibrations ($\nu(CH_2)$), the band centered at 2930 cm^{-1} originates from C-H vibrations in terminal methyl groups ($\nu(CH_3)$) and the peak at 3005 cm^{-1} is the result of C-H vibrations at unsaturated C=C bonds of the lipids (ν(=C-H)) (Keller et al., 1993; Sadeghi-Jorabchi et al., 1991). Other very strong vibrational modes of C-H bonds appear in the fingerprint region(< 2000 cm^{-1}) (Figure 3.1a-d). The peaks at 1445 and 1300 cm^{-1} originate respectively from $\rangle CH_2$ scissoring ($\delta(CH_2)$) and the in-phase methylene twisting mode. In addition to C-H bond vibrations, the 1750 cm^{-1} resonance results from the C=O

stretching ((ν(C=O)) of the ester groups present in glycerides, the 1655 cm^{-1} peak can be attributed to C=C vibrations (ν(C=C)) of unsaturated lipids and the peak at 1080 cm^{-1} can be linked to skeletal C-C vibration (ν(C-C)) of the lipids (Keller et al., 1993; Sadeghi-Jorabchi et al., 1991). All of these vibrational resonances show up as distinctive peaks that are directly related to the lipids in mayonnaise. The Raman spectrum of water (ν(O-H)) is generally known to consist of a very broad peak centered around 3500 cm^{-1} that extends almost into C-H region.

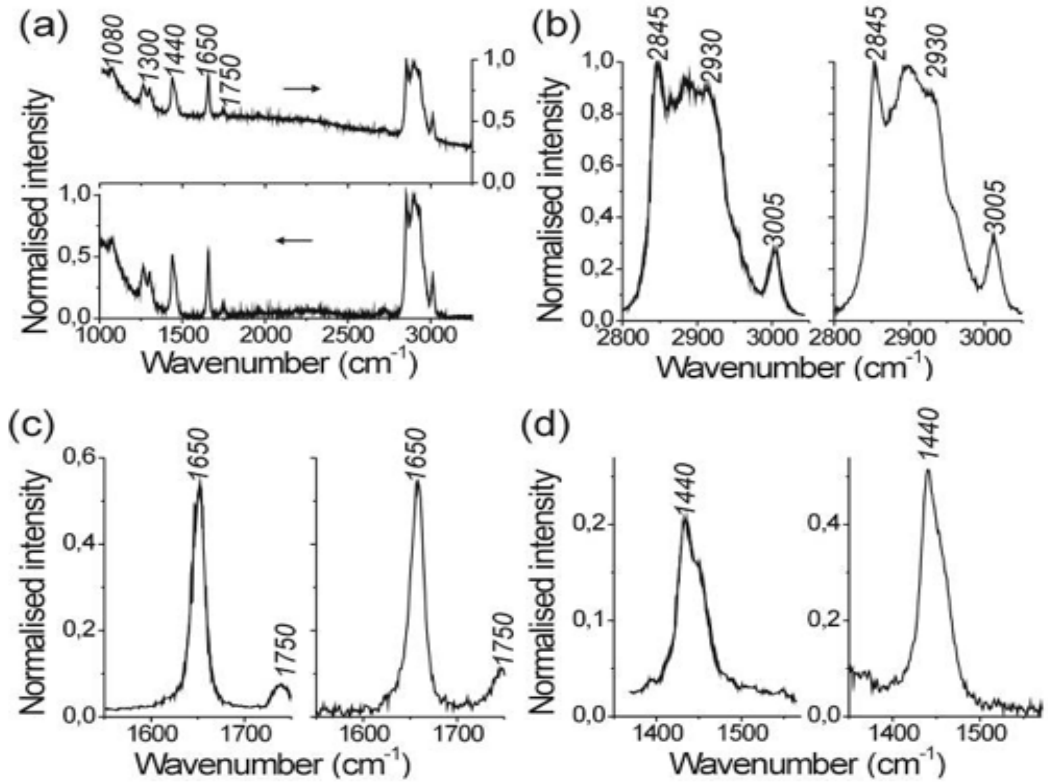

Figure 3.1 Comparison between spontaneous and stimulated Raman spectrum of a mayonnaise sample. (a) Spontaneous Raman spectrum before (top) and after (bottom) subtraction of the fluorescence background. (b)-(d) SRS spectrum (left) and spontaneous Raman spectrum (right) measured at different regions of the vibrational spectrum.

In the next step, we acquired SRS spectra of the same mayonnaise sample. A LabVIEW program was used to acquire the data points with approximately 1 cm^{-1} per step by automated tuning of

the OPO's Lyot filter and the acquisition time for every data point was 100 ms. Figure 3.1b-d compare the stimulated (left) and spontaneous Raman scattering (right) spectra for three different vibrational regions. These spectra clearly show that SRS does not suffer from the interference with the non resonant background like coherent anti-Stokes Raman scattering. Instead of the dispersive line shapes of CARS spectra, SRS spectra are identical to the spontaneous Raman spectra. Another major benefit of SRS is that it is not hindered by background fluorescence: no fluorescence background corrections had to be performed as was done for the spontaneous Raman spectrum in Figure 3.1. Due to the similarity in spectral response between SRS and spontaneous Raman scattering it is safe to use the well known, molecularly-specific vibrational frequency of a species of interest for coherent excitation. Since the SRS signal is linear with concentration, local variations in signal intensity can be directly related to differences in local concentration.

This approach was used to visualize the water and lipid distribution in mayonnaise (Figure 3.2a-f). Figure 3.2a-c show the lipid distribution based on the paraffinic CH_2 stretching (2845 cm^{-1}), the $\diagdown\!\diagup CH_2$ scissoring (1445 cm^{-1}) and the in-phase methylene twisting mode (1303 cm^{-1}). All three images are representative for both unsaturated and saturated lipids and show, as expected, a similar distribution. In Figure 3.2d-e the distribution of unsaturated lipids is visualized by targeting the peaks at 3005 cm^{-1} and at 1655 cm^{-1}. As expected for mayonnaise, the unsaturated and saturated lipids are co-localized within large lipid droplets which range in size from 1 to 15 μm in diameter. The inverse picture (Figure 3.2f) is obtained when recording the water distribution at 3250 cm^{-1}. The two complementary pictures nicely visualize the molecular distribution in this oil in water emulsion. These measurements show that with SRS microscopy we can selectively visualize the different components of a multiphase material like mayonnaise

without adding labels and with a time resolution that is more than three orders of magnitude faster than typical spontaneous Raman imaging.

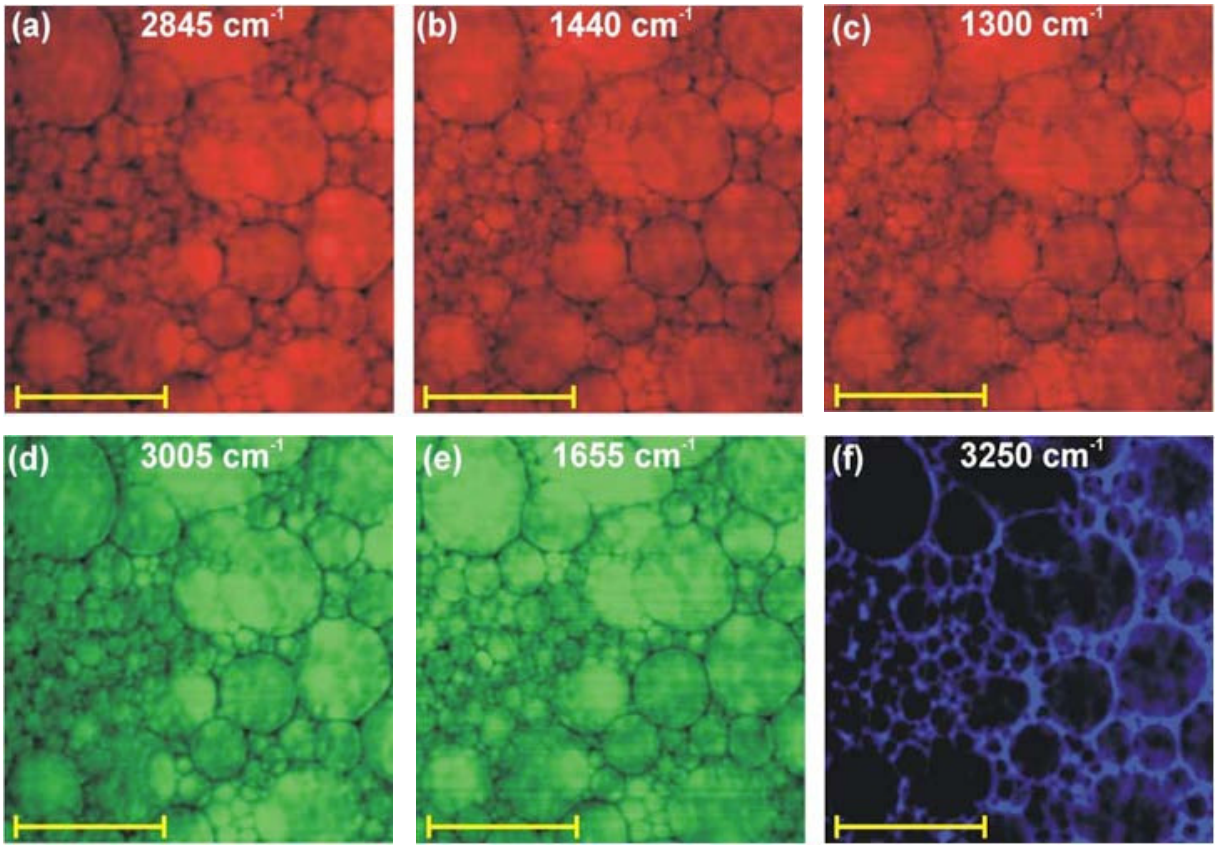

Figure 3.2 SRS micrographs (52 x 52 µm²) of mayonnaise.(a)-(c) SRS images at different CH_2 vibrational resonances using: (a) 2845 cm^{-1}, (b) 1440 cm^{-1} and (c) 1300 cm^{-1}. (d)-(e) SRS images of the unsaturated lipid distribution recorded at: (d) 3005 cm^{-1} and (e) 1655 cm^{-1}. (f) Water distribution measured at 3250 cm^{-1}. Scale bar in the images is 20 µm.

3.2.2 SRS imaging of proteins, lipids and water in cheese and soy drinks

In general, food products have a more complex chemical composition. In addition to oil and water, significant amounts of proteins and carbohydrates are also often present. We for example examined cheese and a soy-based drink which contain significant amounts of proteins, lipids and water. In this particular semi hard Swiss cheese sample the listed content is 28 wt% lipids and 32 wt% proteins. Figure 3.3a shows the spontaneous Raman spectrum after correction for the

background. Noteworthy is the absence of the 3005 cm^{-1} resonance peak in the CH stretching region, which indicates that virtually the whole fat content of this cheese consists of saturated lipids. Due to the presence of large quantities of proteins in cheese compared to the mayonnaise, there is also a relative increase of the terminal methyl group ($\nu(CH_3)$) vibration at 2930 cm^{-1} with respect to that at 2845 cm^{-1} stemming from aliphatic $\nu(CH_2)$ resonance. Furthermore, the aromatic amino acids in proteins like phenylalanine and tryptophan give rise to a new peak at 3060 cm^{-1}, which is a signature for aromatic C-H vibrations. Because of these aromatic amino acids, there should be another very distinctive peak in the fingerprint region at 1004 cm^{-1} originating from the ring breathing mode of phenylalanine. Even though there are almost no unsaturated lipids present in this sample, there is still a very strong resonance at 1650 cm^{-1}. This signal is generated by the $\nu(C=O)$ in the amide bonds of proteins which occurs at the same frequency as C=C bonds of unsaturated lipids. When using the 1650 cm^{-1} peak for coherent Raman imaging, care must be taken to analyze the relatively contributions of lipids and proteins in this frequency range.

By using these different distinctive vibrational resonances, SRS allows selective visualization of the protein, lipid and water distribution. Figure 3.3b-d compares the SRS images of a 95 x 95 μm^2 region taken for different C-H vibrations. The images taken at 2845 cm^{-1}, specific for the lipid distribution (Figure 3.3b), and at 3060 cm^{-1}, specific for the protein distribution (Figure 3.3c), show an inverse contrast indicating that this cheese consists of two well separated phases (Gunasekaran and Ding, 1999; Ribero et al., 2009). The image taken at the water tail (Figure 3.3d) at 3250 cm^{-1}, shows the same distribution as the protein channel, suggesting that water and proteins make up one phase of the cheese material and lipids can be found in a separate phase. To demonstrate that the broad water resonance cannot explain the contrast at 3060 cm^{-1}, an SRS

spectrum was recorded to prove that in this case the signal measured at 3060 cm^{-1} is representative for the protein distribution. An overall spectrum was collected by scanning rapidly over the whole image area (95x95 µm²) while recording the spectrum, approximately 1 cm^{-1} per 100 ms. This spectrum (Figure 3.3e) clearly shows the presence of a resonant peak at 3060 cm^{-1}, specific for aromatic amino acids in proteins.

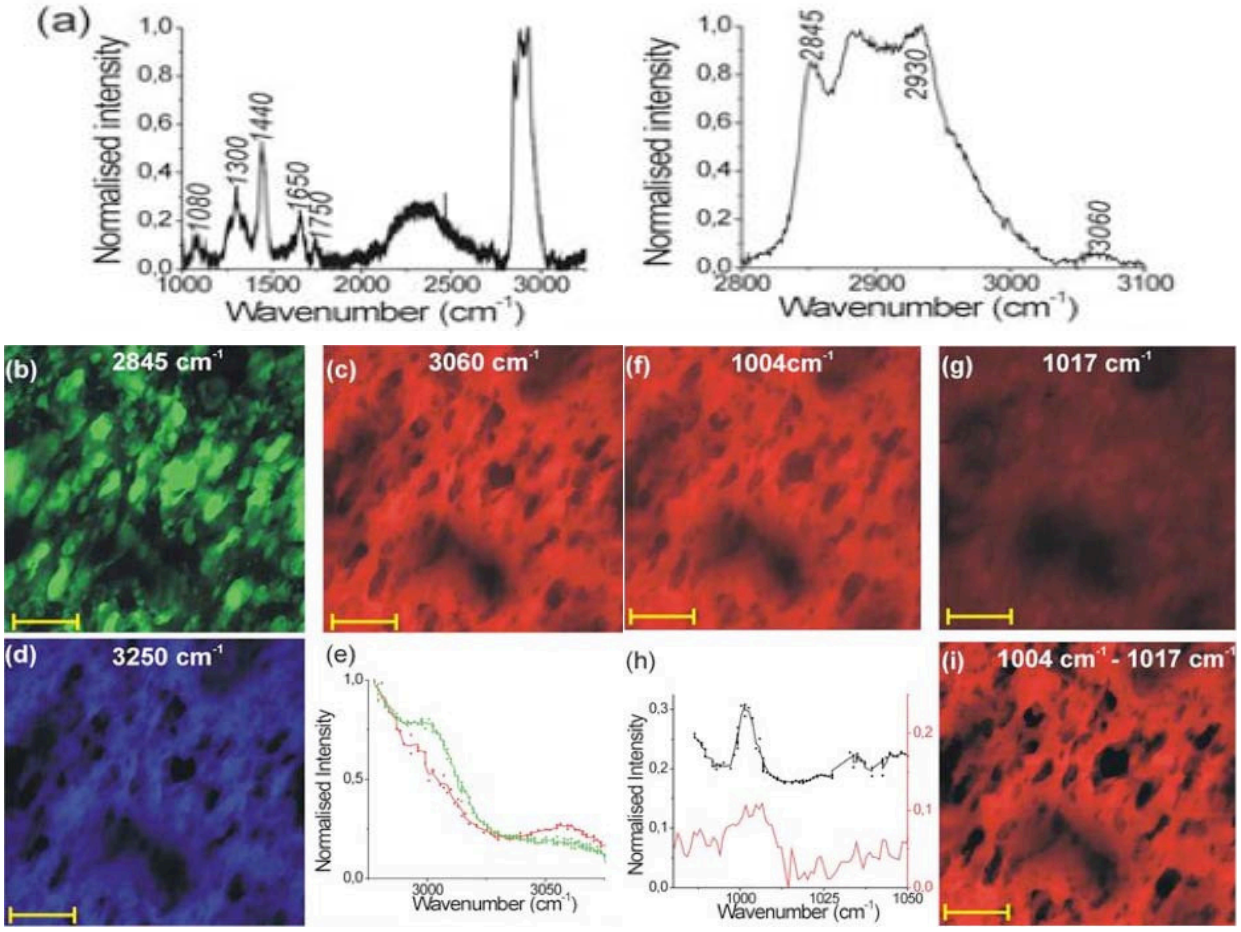

Figure 3.3 Vibrational characterization of biomolecules in cheese sample. (a) Spontaneous Raman spectrum. (b)-(d) SRS images of the distribution of (b) lipids (2845 cm^{-1}), (c) protein(3060 cm^{-1}), and (d)water(3250 cm^{-1}) (e) SRS spectrum of the whole area (red) and of the lipid phase (green). (f) SRS image of protein distribution by targeting the 1004 cm^{-1} ring breathing resonance of phenylalanine. (g) SRS micrograph measured at 1017 cm^{-1}. (h) Comparison between the spontaneous Raman spectrum after fluorescence substraction (red) and the SRS spectrum around 1004 cm^{-1} (i) Image obtained by subtracting the signal detected at 1004 cm^{-1} and 1017 cm^{-1}. The scale bar in the SRS micrographs is 20 µm.

When focusing specifically on a fat globule, a small bump due to the presence of a small amount of unsaturated lipids can be resolved. Another useful vibrational resonance to specifically target the protein distribution is the phenylalanine peak at 1004 cm^{-1}; Figure 3.3f shows the protein distribution as determined at this phenylalanine peak. This picture compares well to Figure 3.3c recorded at 3060 cm^{-1}, however the zones where lipids are present show some residual intensity. This residual SRS intensity can be attributed to the multitude of vibrational resonances that are close by and partly overlapping. This becomes even more apparent when tuning the pump wavelength less than 2 nm away when recording at 1017 cm^{-1} (Figure 3.3g).

This picture clearly shows a vibrationally resonant signal which clearly has a different distribution than the one recorded at the phenylalanine peak. The presence of multiple vibrational resonances can also be seen as a broad offset of this phenylalanine peak in the SRS spectrum (Figure 3.3h). In contrast to the spontaneous Raman spectrum, where this peak is only weakly present, the SRS spectrum shows a significant resonance intensity. To minimize the contribution from nearby vibrational resonances, the signal obtained at 1017cm^{-1} was subtracted from that at 1004cm^{-1} (Figure 3.3i). This image shows a lipid phase that is virtually free of any protein content similar to that obtained at 3060 cm^{-1} (Figure 3.3c).

Since SRS microscopy allows fast image acquisition at one vibrational frequency and since tuning between the different bands can be performed reasonably fast, this approach can also be used to image biomolecular distributions in liquid samples like a commercial soy-based drink. The lipid distribution was determined by measuring the SRS signal at 2845 cm^{-1} (Figure 3.4a), the protein content was determined by targeting the phenylalanine peak (1004 cm^{-1}, Figure 3.4b) and for the water distribution the SRS signal was measured at 3400 cm^{-1} (Figure 3.4c). These images and the combined multicolor image (Figure 3.4d) clearly show that this sample has a

more complex multiphasic structure. This colloidal system clearly consists of a continuous water phase in which the proteins and lipids are dispersed as separate phases.

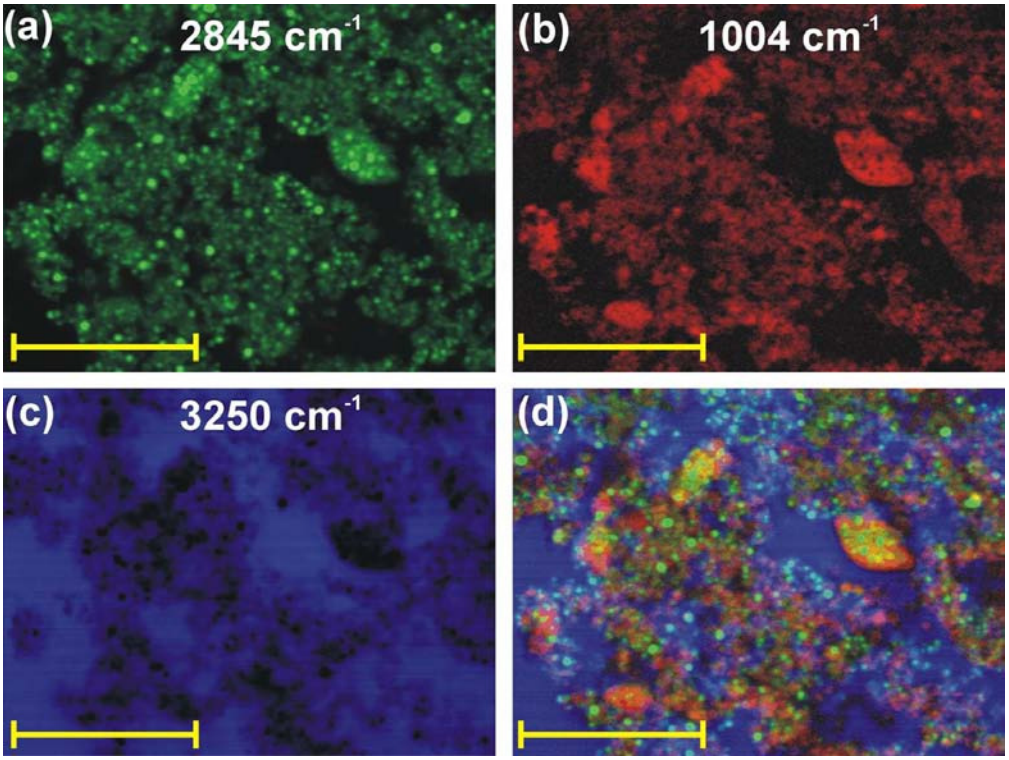

Figure 3.4 SRS image of the distribution of (a) lipids, (b) protein and (c) water in a soy-based drink (54 x 40 µm² area). (d) Multicolor image showing the combined distribution of all three components. Scale bar is 20 µm.

3.3 Methods and Materials

3.3.1 Sample preparation

Three commercial food samples were used in this study: mayonnaise (Hellmann's® Real Mayonnaise, Unilever), cheese (Swiss Cheese, Trader Joe's) and soy-based drink (AdeZ, Unilever). 120 µm thick samples were prepared between two No.1 coverslides (VWR) by using a spacer made from double-sided adhesive sheets (SecureSeal SA-S-1L, Grace Bio-labs). All experiments were performed at room temperature.

3.3.2 Instrumentation

The imaging system is similar to what has been described in Section 2.3.1. The laser source of this microscopy setup is a 1064-nm Nd:YVO4 laser (picoTRAIN, High-Q, Watertown, Massachusetts) that delivers 6 ps pulses at a 76-MHz repetition rate. One part of the output is frequency doubled to 532 nm, which pumps an optical parametric oscillator (OPO) (Levante Emerald, APE-Berlin, Berlin, Germany). A second output directly provides the remaining part of the 1064-nm beam. The signal beam of the OPO is tunable between 680 and 1010 nm. In this SRS setup, the OPO output is used as the pump beam for the SRS experiment, which in combination with the 1064-nm output of the Nd:YVO4 laser (Stokes beam) probes the Raman shifts from >3500 to 500 cm^{-1}. The idler beam of the OPO is blocked with filter (CARS 890/220m, Chroma Technology, Bellow Falls, Vermont). A home-built Pockel cell based on a pair of 2×2×10 mm rubidium titanyl phosphate crystals (Raicol Crystals, Ltd., Yehud, Israel) combined with a polarizer is used to modulate the Stokes beam intensity. The modulation frequency of 10.4 MHz is directly provided by the lock-in amplifier (SR844RF, Stanford Research Systems, Sunnyvale, California). The pump and Stokes beam are spatially overlapped using a dichroic mirror (1064 DCRB, Chroma Technology, Bellow Falls, Vermont), and a manual delay stage is used to overlap both pulse trains in time. These two spatially and temporally overlapped laser beams are directed into an upright Olympus laser-scanning microscope (BX61WI/FV300, Olympus, Pittsburgh, Pennsylvania) optimized for NIR transmission. The sample is illuminated through a 60×1.2-NA (Numerical Aperture) water objective (UPlanApo/IR, Olympus, Pittsburgh, Pennsylvania), and care is taken that the beam diameter matches the size of the back aperture of the objective. The transmitted light is collected with a 1.4-NA oil condenser (Nikon, Melville, New York), which is aligned for Koehler illumination. After passing a telescope, the transmitted light is spectrally filtered by a bandpass

filter (CARS890/220M, Chroma Technology, Bellow Falls, Vermont) and detected by a large-area photodiode (FDS1010, Thorlabs, Newton, New Jersey) with a reversed bias of 64 V. Before measuring the modulation transfer with a high-frequency lock-in amplifier (SR844RF, Stanford Research Systems, Sunnyvale, California), an electronic bandpass filter (BBP-10.7, Mini-Circuits, Brooklyn, New York) is used. The analog output of the lock-in amplifier is fed into the input of the microscope's A/D-converter. Images were taken at 42µs/pixel or 11 s for a 512×512–pixel image. Recording of SRS spectra was performed using a home-built LabVIEW routine. This software automatically scans the output of the OPO over a 10–20 nm range by changing the orientation of the in-cavity Lyot filter and simultaneously records the SRS signal intensity directly from the analog output of the lock-in ampli- fier. Phase-matching temperature and cavity length of the OPO were set manually and remain unchanged during the tuning.

3.4 Conclusion

We have used SRS as a non-invasive tool to map distributions of specific biomolecules in food products at the submicron-scale. SRS microscopy combines high sensitivity resulting from the coherent excitation of molecular vibrations with easily interpretable contrast because its spectral response is identical to spontaneous Raman spectroscopy. This makes fast and quantitative imaging available using the well known vibrational frequencies throughout the whole vibrational spectrum. This contribution is focused on imaging lipids, proteins and water, using both the high wavenumber CH and OH stretching region as well as a number of fingerprint bands. It was recently shown that SRS microscopy also allows direct targeting of sugars like cellulose and more complex biopolymers like lignin in plant materials(Saar et al., 2010). Therefore, SRS microscopy is an ideal tool to study the biomolecular distribution in a wide range of research

areas based on the full information of Raman spectroscopy. As food microstructure gets more attention in the food processing or engineering industry, SRS will potentially bring new opportunities for these fields such as serving as a quality control or screening tool.

References

Aguilera, J.M.(2005).Why food microstructure? Journal of Food Engineering *67*, 3-11.

Blonk, J.C.G., van Aalst, H. (1993) Confocal scanning light microscopy in food research. Food Research Internation *26*, 297-311.

Chen, J.X., Volkmer, A., Book, L.D., and Xie, X.S. (2002). Multiplex coherent anti-stokes Raman scattering microspectroscopy and study of lipid vesicles. J Phys Chem B *106*, 8493-8498.

Cheng, J.X., Book, L.D., and Xie, X.S. (2001). Polarization coherent anti-Stokes Raman scattering microscopy. Optics Letters *26*, 1341-1343.

Cheng, J.X., and Xie, X.S. (2004). Coherent anti-Stokes Raman scattering microscopy: Instrumentation, theory, and applications. J Phys Chem B *108*, 827-840.

Evans, C.L., and Xie, X.S. (2008). Coherent Anti-Stokes Raman Scattering Microscopy: Chemical Imaging for Biology and Medicine. Annual Review of Analytical Chemistry *1*, 883-909.

Freudiger, C.W., Min, W., Saar, B.G., Lu, S., Holtom, G.R., He, C.W., Tsai, J.C., Kang, J.X., and Xie, X.S. (2008). Label-Free Biomedical Imaging with High Sensitivity by Stimulated Raman Scattering Microscopy. Science *322*, 1857-1861.

Gunasekaran, S., and Ding, K. (1999). Three-dimensional characteristics of fat globules in cheddar cheese. Journal of Dairy Science *82*, 1890-1896.

Keller, S., Lochte, T., Dippel, B., and Schrader, B. (1993). Quality-control of food with near-infrared excited raman-spectroscopy. Fresenius Journal of Analytical Chemistry *346*, 863-867.

Langton, M., Jordansson, E., Altskar, A., Sorensen, C., and Hermansson, A.M. (1999). Microstructure and image analysis of mayonnaises. Food Hydrocolloids *13*, 113-125.

Pawley, J. (2006). Handbook of Biological Confocal Microscopy (Springer).

Potma, E.O., Evans, C.L., and Xie, X.S. (2006). Heterodyne coherent anti-Stokes Raman scattering (CARS) imaging. Optics Letters *31*, 241-243.

Ribero, G.G., Rubiolo, A.C., and Zorrilla, S.E. (2009). Microstructure of Mozzarella cheese as affected by the immersion freezing in NaCl solutions and by the frozen storage. Journal of Food Engineering *91*, 516-520.

Saar, B.G., Zeng, Y., Freudiger, C.W., Liu, Y.-S., Himmel, M.E., Xie, X.S., and Ding, S.-Y. (2010). Label-Free, Real-Time Monitoring of Biomass Processing with Stimulated Raman Scattering Microscopy. Angew Chem, Int Ed *49*, 5476-5479.

Sadeghi-Jorabchi, H., Wilson, R.H., Belton, P.S., Edwards-Webb, J.D., and Coxon, D.T. (1991). Quantitative-analysis of oils and fats by fourier-transform Raman-spectroscopy. Spectrochimica Acta Part a-Molecular and Biomolecular Spectroscopy *47*, 1449-1458.

Sadeghijorabchi, H., Wilson, R.H., Belton, P.S., Edwardswebb, J.D., and Coxon, D.T. (1991). Quantitative-analysis of oils and fats by fourier-transform Raman-spectroscopy. Spectrochimica Acta Part a-Molecular and Biomolecular Spectroscopy *47*, 1449-1458.

Vartiainen, E.M., Rinia, H.A., Muller, M., and Bonn, M. (2006). Direct extraction of Raman line-shapes from congested CARS spectra. Optics Express *14*, 3622-3630.

Volkmer, A., Book, L.D., and Xie, X.S. (2002). Time-resolved coherent anti-Stokes Raman scattering microscopy: Imaging based on Raman free induction decay. Applied Physics Letters *80*, 1505-1507.

Chapter 4

Histopathology Study on Human Brain Tissues Using Stimulated Raman Scattering Microscopy

With the emergence of more advanced medical imaging technologies such as MRI and CT, abnormities in human body can be identified at earlier stage. However, in order to get a confirmative understanding of identified suspicious lesions, surgical biopsy with histology test is usually needed for the intra-operative consultation with pathologist. The traditional histology procedure requires multiple steps including freezing, sectioning and staining, which usually requires 30 minute for each round. In human brain, surgeons bear high risk upon decision making on surgical endpoints due to the complexity and importance of neuron network in this region, therefore an imaging guided probe without need for biopsy is in big demand. We here demonstrate that SRS imaging can provide the same pathology features compared with H&E staining on frozen sections of mouse and human brain tissue. The label-free imaging mechanism combined with intrinsic 3D sectioning capability potentially eliminates the need for biopsy, and with further technical development of handheld scanning probe coupled with fiber optics, imaging guided intra-operative pathological diagnosis may become possible in the near future.

Contributions

The work in this chapter involved close collaboration with Dr. Pedro Ciarlini and Dr. Geoff Young. I, Dr. Young, Dr. Ciarlini and Prof. Xie conceived the idea and designed the project. Dr. Ciarlini conducted sample preparation. I conducted imaging experiments as well as image analysis.

4.1 Background

4.1.1 Histopathology

Technological advancement in medical imaging has been driving the early stage clinical diagnosis. The emergence of Magnetic Resonance Imaging (MRI) has enabled medical doctors to noninvasively visualize abnormalities within patient bodies. However the spatial resolution of MRI is still low lacking extensive chemical contrast. Lesions such as tumor appear as shadows in the MRI images with different color compared to surrounding areas. However medical doctors cannot make conclusive diagnosis solely based on this feature since some post surgery inflammation (pseudoprogression) also appear as similar features in the MRI contrast (Hygino da Cruz et al., 2011). In order to conduct a more precise diagnosis, a surgery is usually scheduled for a biopsy, which is a process to remove pieces of tissue from the suspicious area. The appearance of neoplastic tissue is hard to distinguish from healthy tissue and a histology test is usually needed. The pathologists are called into the operation room to perform intra-operative consultation based on the histological result on the removed tissue. A quick diagnosis using frozen sections is usually conducted outside the operation room. The tissue is first embedded in the OCT (Optimal Cutting Temperature Compound) and placed into the cryostat microtome at -20^{o}C. The OCT freezes into a white block at this temperature and is cut into thin slices using the microtome. The sliced tissue is mounted a glass slide and placed into H&E (Hemotoxylin and Eosin) stains. The stained tissue is then placed under light microscope and pathologists conduct diagnosis based on the features shown in the H&E stained slides. Pathologists then communicate with the surgeon about the diagnostic result as either non-tumor, benign or malignant tumor to help make further operative

decisions. This process usually takes 20~30 minutes each time. If malignant tumor is confirmed based on the pathology result, the surgeon usually goes back to the patient and remove additional tissue next to previous removal spot and the same pathology test procedure is repeated. Since it is risky to remove large areas of tissue from the human body especially like in brain, where a lot of neural connections exist and any destruction of this may cause mental dysfunction, repetitive process removing a small piece each time is needed to clear the tumor margin in the operation. This may take hours depending on the area of the tumor and the patient body needs to be exposed during the entire process with the general anesthesia in effect during the whole process as well. Making decisions on the surgical endpoint has been the major challenge in neurosurgical oncology given the complexity of infiltrated tumor and potential premature recurrence if the tumor is not cleared (Kalkanis et al., 2010; Nazzaro et al., 1990; Sughrue et al., 2010). In current neurosurgical practice, the ineffective surgical procedure rate is still very high (Albert et al., 1994).

Frozen section method is a fast approach providing pathological information in the intro-operative process but the quality is still low. More accurate pathology diagnosis is conducted by formalin fixed paraffin embedded tissue processing procedure which usually takes 2 days to get the result.

4.1.2 Why SRS imaging?

Stimulated Raman Scattering (SRS) microscopy can visualize the cell nuclei, cytoplasm without the need for any staining or labeling as described in Chapter 2. It can be used a noninvasive chemical analysis tool with its quantitative detectability of lipid, protein and nucleic acid concentration. Pathologists make diagnosis upon the H&E staining slides

mainly based on the cellularity, nucleus to cytoplasm ratio. These features can all be captured by SRS imaging (Ji et al., 2013; Freudiger et al. 2012). Based on the nonlinear optical process, SRS imaging has intrinsic 3D sectioning capability and the vertical resolution is much better than the sectioning resolution of a microtome (Saar et al., 2010; Horton et al., 2013). Therefore there is also no sectioning needed for this imaging modality.

Recently SRS imaging has reached video-rate imaging speed and can work in the epi-detection scheme (Saar et al., 2010), which brings new potential of future intro-operative diagnosis with SRS imaging modality incorporated to the endoscope (Saar et al., 2010). Moreover, the biosafety of utilized optical exposure can be well controlled (Fu et al., 2006; Nan et al., 2006). Therefore, real time pathology guided surgery without the need for biopsy may not be a dream in the near future. The surgical endpoints can be redefined based on the SRS images rather than the gross visual and textural indications that surgeons rely on at the moment (Nimsky et al., 2003; Stummer et al., 2006).

Here we first demonstrate the SRS imaging on frozen sections from brain tissue and have pathologists conduct blind reading upon the images. Traditional H&E staining images are also shown side by side for comparison.

4.2 Results

4.2.1. SRS Imaging on Mouse Brain

SRS imaging was first conducted on the mouse brain sections for method validation and sample preparation testing. Two individual scans were performed on each area in the brain tissue with one excitation beam fixed at 1064nm and the other beam switching

between 816.7nm (corresponding to 2845 cm^{-1}) and 810.5nm (corresponding to 2930 cm^{-1}). Adjusting Lyot filter and the cavity length of the optical parametric oscillator (OPO), the tuning between the two wavelengths can be achieved in a few seconds. This was conducted automatically using Labview program and the sample stage was motorized to move to the next scanning area. Images were processed using ImageJ and pseudo-colors were assigned to each scanning wavelength. The green channel (Figure 4.1a) shows the SRS image taken at 2845 cm^{-1}, the blue channel (Figure 4.1b) shows the SRS image taken at 2930 cm^{-1}. The nuclei in Figure 4.1a appear darker than the surrounding extracellular areas due to the lack of lipid, but the intensity difference in Figure 4.1b is smaller. A linear combination method is utilized here to extract the lipid and protein distributions (Fu et al., 2012; Freudiger et al., 2012; Ji et al., 2013), color-coded and combine them in Figure 4.1c with green indicating the lipid and blue indicating the protein.

Different features can be observed in distinct regions of brain (Figure 4.1c-f). The cellular regions (Figure 4.1d) can be well differentiated from myelin-rich regions such as fiber tracts (Figure 4.1e) (Wang et al., 2005).

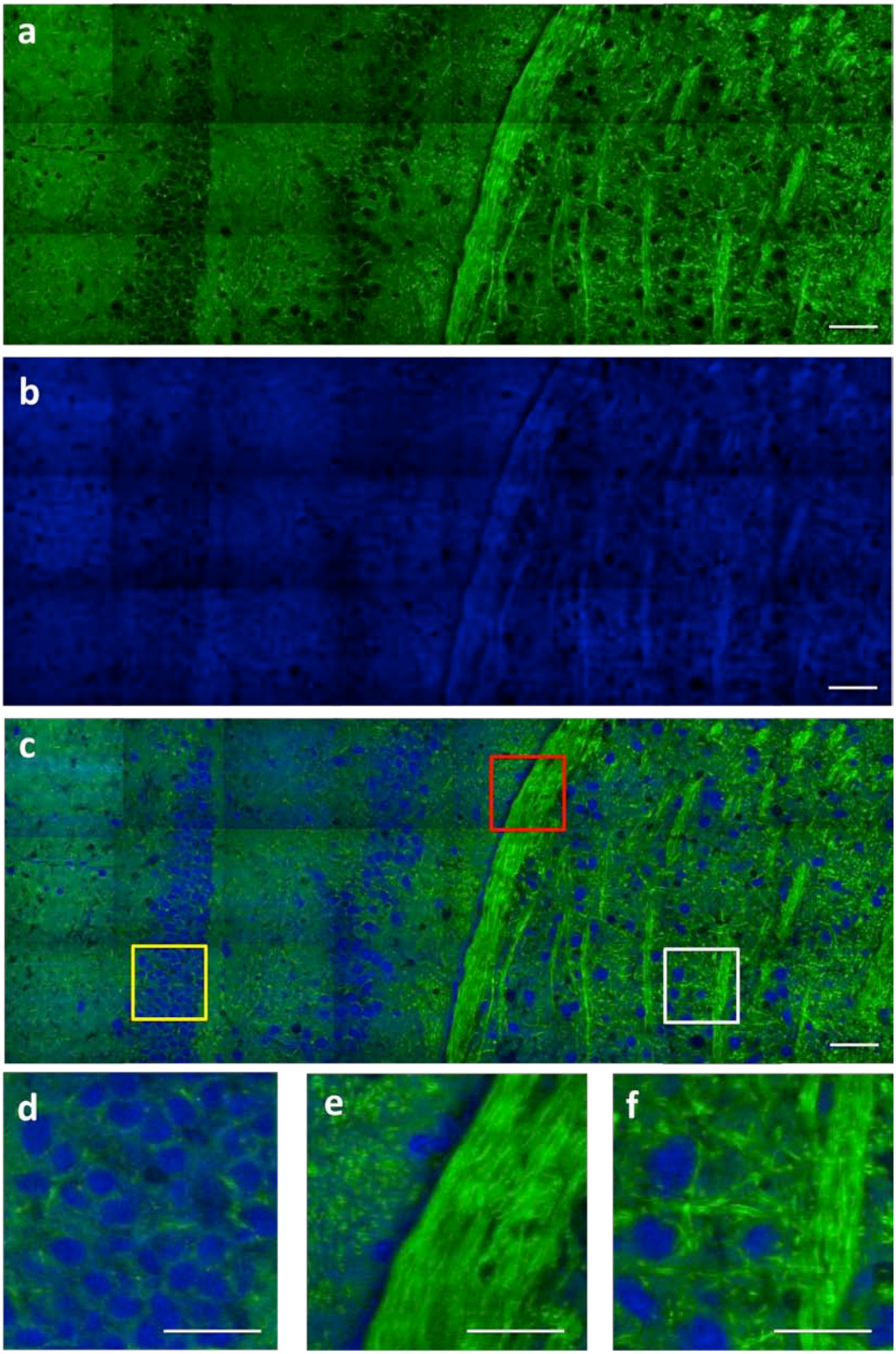

Figure 4.1 Multicolor SRS images of mouse brain(a)Lipid distribution taken at 2845cm^{-1}, (b) Protein distribution taken at 2930cm^{-1}, (c) Merged image of (a) and (b), (d)-(f) Zoomed in images of white, yellow and red box in (c). scale bar: 50 μm.

4.2.2. SRS Imaging on Human Brain Frozen Section Tissues

Figure 4.2 shows the two color SRS image (b) and H&E staining (a) from a human brain frozen section. This section is from an area with Glioblastoma Multiforme (GBM), which is the most common and aggressive malignant primary brain tumor in human. The green channel represents the SRS signal taken at 2845cm^{-1} reflecting the distribution of lipid content. The blue channel represents the SRS signal taken at 2930cm^{-1} reflecting the distribution of protein content. Nuclei show up as blue color due to lack of lipid content. Tumor cells are apparent due to the high nuclear-to-cytoplasm ratio, which is consistent with H&E staining.

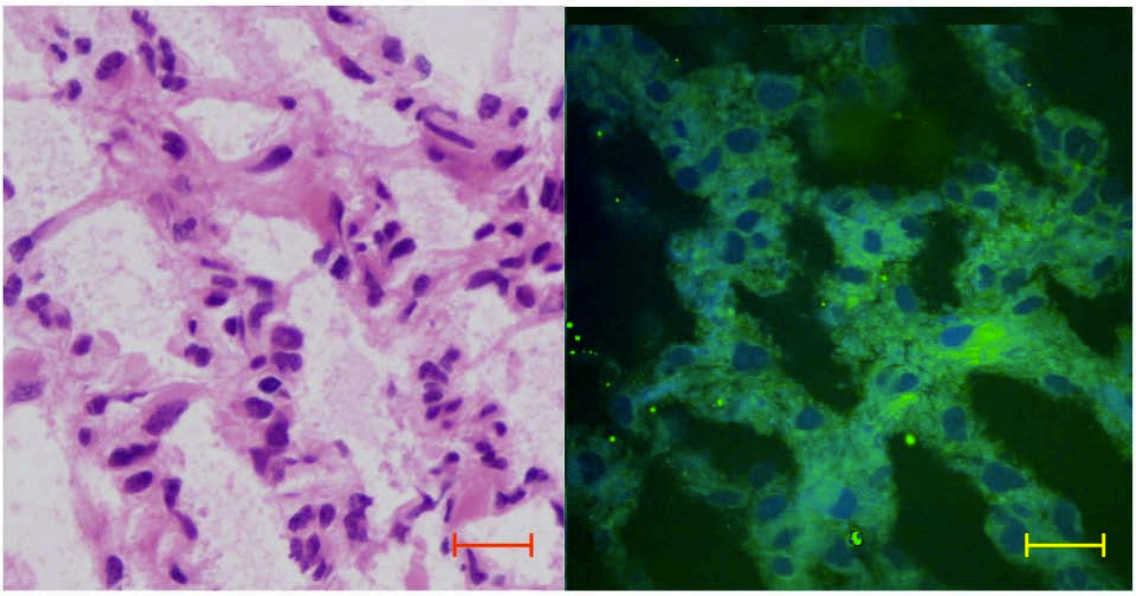

Figure 4.2 (a) H&E staining (b) SRS image of Glioblastoma Multiforme (GBM) from a human frozen section case. Scale bar is 25 μm.

In order to capture information from a bigger area of tissue without compromising the resolution, a tiling approach (Ji et al., 2013) was used. Fast laser switching between 2845cm^{-1} and 2930cm^{-1} was performed by Labview program automatically. The translational stage moved by the length of the field of view after image acquisition at

these two channels. The acquired images were reconstructed to create a composite image of the entire scanned area.

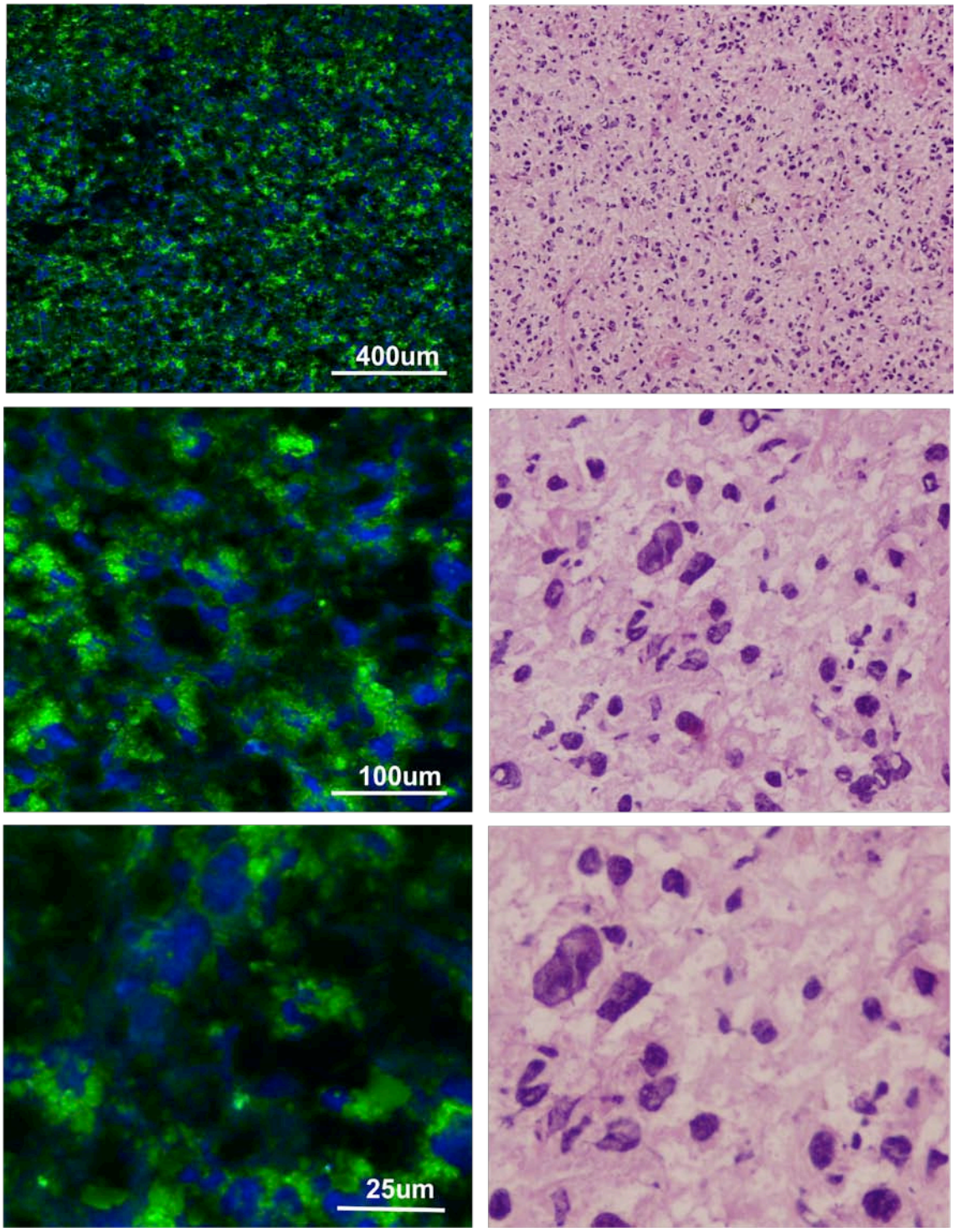

Figure 4.3 SRS (left) and H&E (right) images of Glioblastoma Multiforme at different scales.

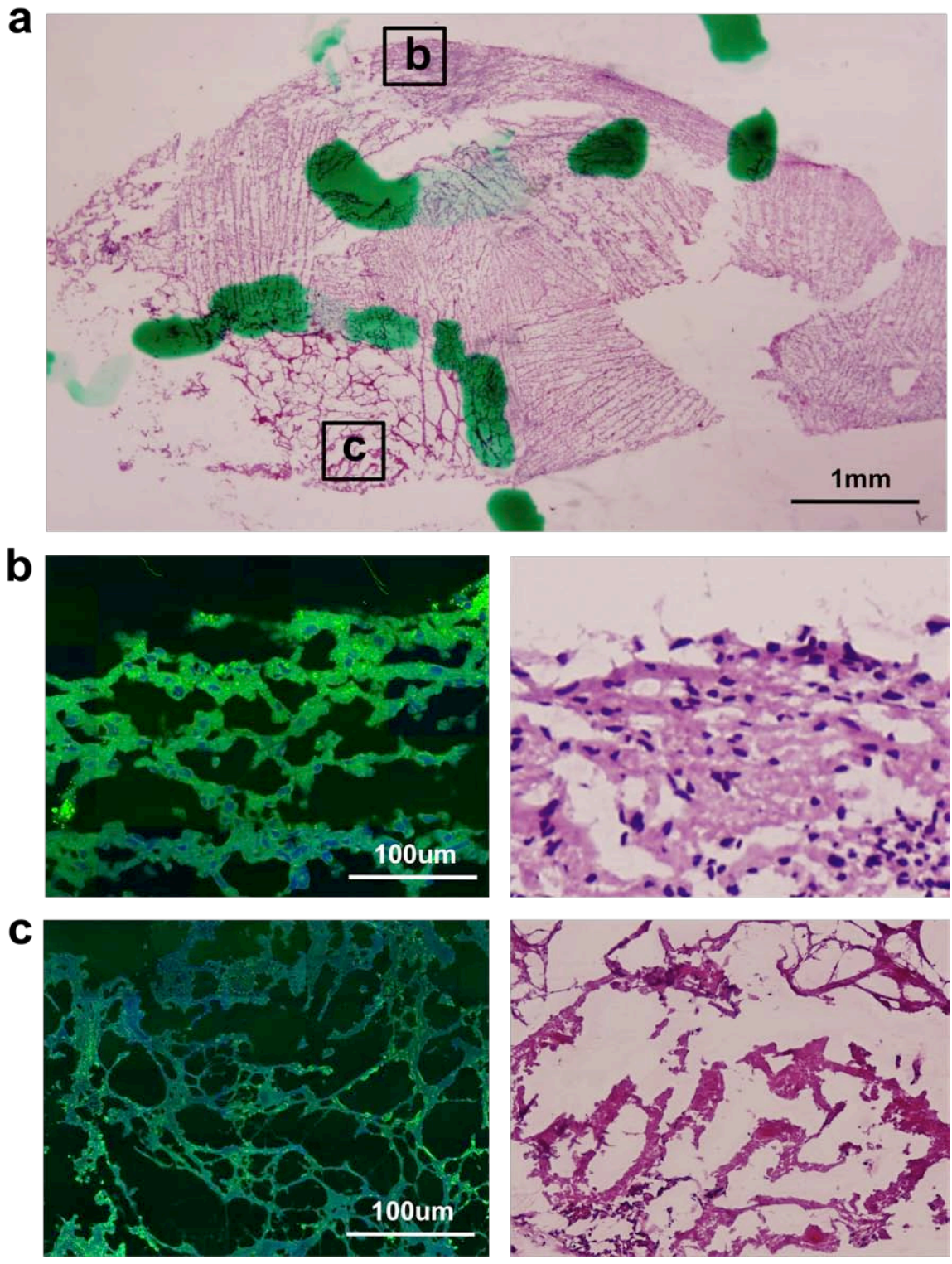

Figure 4.4 Comparison between necrosis and tumor.

As seen in Figure 4.3, the SRS images are comparable to H&E staining images at

different scales, which mimics the procedures of switching to objectives with different magnification performed by pathologists during the diagnosis process.

In Figure 4.4, this case contains both regions of tumor and necrosis (dead tissue). The SRS images of these two regions are shown in (b) and (c), where different cellularity and nucleus-to-cytoplasm ration are observed. SRS has the capability to identify and differentiate tumor and necrosis. Especially for necrosis, the nuclear outlines are still visible in contrast to H&E. This additional detail helps pathologists to confirm their diagnosis on necrosis, which sometimes is difficult on regularly processed formalin-fixed H&E sections. The identification of necrosis has a significant importance in tumor grading. Sometimes tumors cannot be termed as glioblastomas (grade IV) because necrosis is not observed on H&E contrast. Therefore, SRS imaging can potentially help decrease the downgrading of grade IV gliomas.

4.3 Materials and Method

The SRS imaging setup is as described in Chapter 2. The imaging was performed in the transmission mode, in which the signal was collected after the sample plane. Tiling scan over the entire area of the tissues was performed with the scanning steps matching with the field of view of each scan. Image acquisition at two excitation condition was conducted before each translational step.

Sample preparation

Tissues were acquired from the tissue bank at Brigham and Women's hospital according to DF/HCC Protocol 10-417. The acquired frozen tissue blocks were cut into thin slices using cryostat microtome into 10 μm and mounted on a glass slide. Embedding OCT was washed off the tissues using PBS to avoid potential interfering signal. The tissues were

then placed the 4% formalin and sent to Xie Lab in Harvard campus in Cambridge for SRS imaging.

Mouse tissue were cut into 5um and 10um using cryostat microtome and imaged using SRS imaging. Adjacent sections were put into formalin for 24 hours and imaged. There was no significant degradation being observed over time.

4.4 Discussion and Conclusion

It has been demonstrated that SRS imaging can be used as a diagnostic tool for brain tumor capturing all the information provided by histopathology gold standard H&E staining. According to WHO grading criteria, current diagnosis upon glioblastoma (grade IV tumor) is performed according to 5 major criteria: 1. Vascular proliferation 2. Increased cellularity 3. Nuclear atypia 4. High degree of Mitotic Activity 5. Necrosis (Brat et al., 2008). These features can be captured by SRS imaging by mapping the distribution lipid, protein and nucleic acids (Chapter 2). The combination of lipid and protein channel gives the nuclear shape due to the lack of lipid content in nuclei. Feature 2-4 can be graded based on the image contrast brought by lipid & protein channels, and can be further improved by mapping the nucleic acids concentration. Vascular proliferation can also be identified based on protein distribution.

SRS imaging may have bigger potential in the future compared to traditional histology diagnosis method because it generates the lipid contrast, which is missing in H&E staining. The lipid content is usually washed out for histology sample preparation purposes. Important regions of brain such as white matter rich in lipid are better captured by SRS imaging. Destruction of myelin sheath, which is fatty sheath composed of lipid coating the axons of nerves, leads to neural malfunction or even Alzheimer's disease

(Bartzokis, 2004, 2011). SRS imaging has the capability of analyzing the integrity of myelin sheath, providing indications to these neural diseases.

Several other techniques have also been used for histopathology in a label-free manner. Confocal reflection (Master and So, 2008), optical coherence tomography (OCT) (Tearney et al., 1997) and third harmonic generation (Witte et al., 2011) demonstrate some features of morphology but don't generate multicolor chemical contrast. Second harmonic generation (SHG) and two-photon excited auto-fluorescence (TPAF) are limited to few specific molecules (Zipfel et al., 2003; Li et al., 2010; Campagnola et al., 2002). Infrared absorption also allows for multicolor imaging (Gremlich and Yan, 2001), but in the water-rich tissues the penetration depth and spatial resolution is limited due to the long wavelength (Meyer et al., 2011).

With further development on the miniaturization of SRS system, imaging guided intra-operative pathology diagnosis can be made. Surgeons can have a more reliable way of deciding on the surgical endpoints, which might significantly decrease the biopsy area maintaining the neural function in a much better way. Especially for the infiltrative tumor such as glioma, which infiltrates up to 4 cm from the tumor core (Silbergeld et al., 1997), SRS imaging is more useful in identifying mass lesion and more sparse infiltrating tumor cells. The priority for the surgery is to maximally reduce the mass lesion not to remove every infiltrating cell. However, in most of the glioblastoma surgeries, residual tumor is unpurposely left in the surgical cavity even though it is safe to remove them (Orringer et al., 2012).

There are still some technical challenges to make SRS readily available for intra-operative diagnosis such as correction mechanism for motion and sampling efficiency

over a large area of surgical cavity (Ji et al., 2013). A more quantitative sensitivity and specificity study needs to be conducted for proving clinical feasibility. SRS and CARS imaging with fiber laser source (Freudiger and Yang, 2014; Balu et al., 2010) have been demonstrated and there are continuing efforts upon endoscopy (Legare et al., 2006; Saar et al., 2011), which bring new possibilities of miniaturization of the system. However, more engineering efforts are needed on scanning and detection probe design.

References

Albert, F.K., Forsting, M., Sartor, K., Adams, H.P., and Kunze, S. (1994). Early postoperative magnetic resonance imaging after resection of malignant glioma: objective evaluation of residual tumor and its influence on regrowth and prognosis. Neurosurgery 34, 45-60.

Balu, M., Liu, G., Chen, Z., Tromberg, B.J., and Potma, E.O. (2010). Fiber delivered probe for efficient CARS imaging of tissues. Optics express 18, 2380-2388.

Bartzokis, G. (2004). Age-related myelin breakdown: a developmental model of cognitive decline and Alzheimer's disease. Neurobiology of aging 25, 5-18.

Bartzokis, G. (2011). Alzheimer's disease as homeostatic responses to age-related myelin breakdown. Neurobiology of aging 32, 1341-1371.

Brat, D.J., Prayson, R.A., Ryken, T.C., and Olson, J.J. (2008). Diagnosis of malignant glioma: role of neuropathology. Journal of neuro-oncology 89, 287-311.

Campagnola, P.J., Millard, A.C., Terasaki, M., Hoppe, P.E., Malone, C.J., and Mohler, W.A. (2002). Three-dimensional high-resolution second-harmonic generation imaging of endogenous structural proteins in biological tissues. Biophysical journal 82, 493-508.

Freudiger, C.W., Pfannl, R., Orringer, D.A., Saar, B.G., Ji, M., Zeng, Q., Ottoboni, L., Wei, Y., Waeber, C., Sims, J.R., et al. (2012). Multicolored stain-free histopathology with coherent Raman imaging. Laboratory investigation; a journal of technical methods and pathology 92, 1492-1502.

Freudiger, C.W., Yang, W., Holtom, G.R., Peyghambarian, N., Xie, X.S., and Kieu, K.Q. (2014). Stimulated Raman Scattering Microscopy with a Robust Fibre Laser Source. Nature photonics 8, 153-159.

Fu, Y., Wang, H., Shi, R., and Cheng, J.X. (2006). Characterization of photodamage in coherent anti-Stokes Raman scattering microscopy. Optics express 14, 3942-3951.

Gremlich HU, Yan B. Infrared and Raman Spectroscopy of Biological Materials. Marcel Dekker, Inc.: New York, Vol.24, 2001.

Horton, N.G., Wang, K., Kobat, D., Clark, C.G., Wise, F.W., Schaffer, C.B., and Xu, C. (2013). three-photon microscopy of subcortical structures within an intact mouse brain. Nature photonics 7.

Hygino da Cruz, L.C., Jr., Rodriguez, I., Domingues, R.C., Gasparetto, E.L., and Sorensen, A.G. (2011). Pseudoprogression and pseudoresponse: imaging challenges in

the assessment of posttreatment glioma. AJNR American journal of neuroradiology 32, 1978-1985.

Ji, M., Orringer, D.A., Freudiger, C.W., Ramkissoon, S., Liu, X., Lau, D., Golby, A.J., Norton, I., Hayashi, M., Agar, N.Y., et al. (2013). Rapid, label-free detection of brain tumors with stimulated Raman scattering microscopy. Science translational medicine 5, 201ra119.

Kalkanis, S.N., Kondziolka, D., Gaspar, L.E., Burri, S.H., Asher, A.L., Cobbs, C.S., Ammirati, M., Robinson, P.D., Andrews, D.W., Loeffler, J.S., et al. (2010). The role of surgical resection in the management of newly diagnosed brain metastases: a systematic review and evidence-based clinical practice guideline. Journal of neuro-oncology 96, 33-43.

Kleihues, P., Burger, P.C., and Scheithauer, B.W. (1993). The new WHO classification of brain tumours. Brain pathology 3, 255-268.

Legare, F., Evans, C.L., Ganikhanov, F., and Xie, X.S. (2006). Towards CARS Endoscopy. Optics express 14, 4427-4432.

Li, C., Pastila, R.K., Pitsillides, C., Runnels, J.M., Puoris'haag, M., Cote, D., and Lin, C.P. (2010). Imaging leukocyte trafficking in vivo with two-photon-excited endogenous tryptophan fluorescence. Optics express 18, 988-999.

Louis, D.N., Ohgaki, H., Wiestler, O.D., Cavenee, W.K., Burger, P.C., Jouvet, A., Scheithauer, B.W., and Kleihues, P. (2007). The 2007 WHO classification of tumours of the central nervous system. Acta neuropathologica 114, 97-109.

Master BR, So PTC. Biomedical Nonlinear Optical Microscopy. Oxford University Press, Inc.: New York, 2008.

Meyer, T., Bergner, N., Bielecki, C., Krafft, C., Akimov, D., Romeike, B.F., Reichart, R., Kalff, R., Dietzek, B., and Popp, J. (2011). Nonlinear microscopy, infrared, and Raman microspectroscopy for brain tumor analysis. Journal of biomedical optics 16, 021113.

Nan, X., Potma, E.O., and Xie, X.S. (2006). Nonperturbative chemical imaging of organelle transport in living cells with coherent anti-stokes Raman scattering microscopy. Biophysical journal 91, 728-735.

Nazzaro, J.M., and Neuwelt, E.A. (1990). The role of surgery in the management of supratentorial intermediate and high-grade astrocytomas in adults. Journal of neurosurgery 73, 331-344.

Nimsky, C., Ganslandt, O., Buchfelder, M., and Fahlbusch, R. (2003). Glioma surgery evaluated by intraoperative low-field magnetic resonance imaging. Acta neurochirurgica Supplement 85, 55-63.

Orringer, D., Lau, D., Khatri, S., Zamora-Berridi, G.J., Zhang, K., Wu, C., Chaudhary, N., and Sagher, O. (2012). Extent of resection in patients with glioblastoma: limiting factors, perception of resectability, and effect on survival. Journal of neurosurgery 117, 851-859.

Saar, B.G., Freudiger, C.W., Reichman, J., Stanley, C.M., Holtom, G.R., and Xie, X.S. (2010). Video-rate molecular imaging in vivo with stimulated Raman scattering. Science 330, 1368-1370.

Saar, B.G., Johnston, R.S., Freudiger, C.W., Xie, X.S., and Seibel, E.J. (2011). Coherent Raman scanning fiber endoscopy. Optics letters 36, 2396-2398.

Silbergeld, D.L., and Chicoine, M.R. (1997). Isolation and characterization of human malignant glioma cells from histologically normal brain. Journal of neurosurgery 86, 525-531.

Stummer, W., Pichlmeier, U., Meinel, T., Wiestler, O.D., Zanella, F., Reulen, H.J., and Group, A.L.-G.S. (2006). Fluorescence-guided surgery with 5-aminolevulinic acid for resection of malignant glioma: a randomised controlled multicentre phase III trial. The Lancet Oncology 7, 392-401.

Sughrue, M.E., Kane, A.J., Shangari, G., Rutkowski, M.J., McDermott, M.W., Berger, M.S., and Parsa, A.T. (2010). The relevance of Simpson Grade I and II resection in modern neurosurgical treatment of World Health Organization Grade I meningiomas. Journal of neurosurgery 113, 1029-1035.

Tearney, G.J., Brezinski, M.E., Bouma, B.E., Boppart, S.A., Pitris, C., Southern, J.F., and Fujimoto, J.G. (1997). In vivo endoscopic optical biopsy with optical coherence tomography. Science 276, 2037-2039.

Wang, H., Fu, Y., Zickmund, P., Shi, R., and Cheng, J.X. (2005). Coherent anti-stokes Raman scattering imaging of axonal myelin in live spinal tissues. Biophysical journal 89, 581-591.

Witte, S., Negrean, A., Lodder, J.C., de Kock, C.P., Testa Silva, G., Mansvelder, H.D., and Louise Groot, M. (2011). Label-free live brain imaging and targeted patching with third-harmonic generation microscopy. Proceedings of the National Academy of Sciences of the United States of America 108, 5970-5975.

Zipfel, W.R., Williams, R.M., Christie, R., Nikitin, A.Y., Hyman, B.T., and Webb, W.W. (2003). Live tissue intrinsic emission microscopy using multiphoton-excited native fluorescence and second harmonic generation. Proceedings of the National Academy of Sciences of the United States of America 100, 7075-7080.

Chapter 5

Quantitative Chemical Imaging with Multiplex Stimulated Raman Scattering Microscopy

Previous demonstrations of Stimulated Raman Scattering Microscopy have been limited to single Raman band measurements. In this chapter, we present a novel modulation multiplexing approach that allows real-time detection of multiple species using the fast Fourier transform. Double modulation and double demodulation are employed to achieve high speed and high sensitivity. Combining the advantages of high-speed label-free imaging and the chemical fingerprinting power of Raman spectroscopy, multiplex SRS is a powerful and quantitative method for fast label-free chemical composition analysis in biological systems. We demonstrate the quantitative determination of chemical concentrations in a ternary mixture. Furthermore, two imaging applications are pursued: (1) quantitative determination of oil content as well as pigment and protein concentration in microalgae cultures; and (2) 3D high-resolution imaging of blood, lipids, and protein distribution in ex vivo mouse skin tissue. We believe that quantitative multiplex SRS imaging uniquely combines the advantage of fast label-free imaging with the fingerprinting capability of Raman spectroscopy and enables numerous applications in lipid biology as well as biomedical imaging.

Contributions

The work in this chapter involved close collaboration with Dr. Dan Fu. Dr. Fu and Prof. Xie conceived the idea and designed the project. Dr. Fu, Dr. Fa-Ke Lu and I conducted the experiments and image analysis. Dr. Christian Freudiger, Douglas Pernik and Dr. Gary Holtom facilitated with the technical support.

5.1 Background

Unlike CARS, SRS microscopy has straightforward image interpretation and quantification without the complications arising from non-resonant background and phase matching conditions. Consequently, not only is the signal to noise ratio (SNR) improved, but the Raman spectral fidelity is also preserved. Because SRS has a linear concentration dependence, it has the potential to become a powerful method for label-free quantitative determination of chemical concentrations of individual species in a multicomponent system.

A major limitation of the current implementation of SRS microscopy is that only a single Raman band can be probed at a time. To quantitatively measure multiple components with overlapping Raman bands, at least the same number of bands needs to be measured. However, as high sensitivity SRS imaging uses a high frequency lock-in detection scheme, the same spectral-resolved detection approach that is commonly employed in fluorescence and multiplex CARS detection is currently impractical to implement due to the difficulty of building a multichannel lock-in that works in the MHz frequency range (Cheng et al., 2002; Kano and Hamaguchi, 2005; Muller and Schins, 2002). Spectrally tailored excitation is an excellent way of circumventing this problem and can distinguish as many chemical components as the number of spectral elements (Freudiger et al., 2011). However, this technique is restricted to single species detection per imaging session and it requires all species to be externally calibrated before imaging.

Here we present a novel modulation multiplexing approach that allows multiple Raman bands to be measured simultaneously. Through either in situ calibration or external calibration, multispecies chemical mapping can be implemented at subcellular resolution with speeds at least 3 orders of magnitude faster than confocal Raman imaging.

5.2 Methods

5.2.1 Instrumentation for Multiplex SRS

Instrumentation for multiplex SRS is shown in Figure 5.1. In SRS, the bandwidth of the pump and Stokes lasers determines both the resolution and the spectral coverage. For synchronized picosecond lasers that are typically employed for SRS microscopy, the spectral resolution is usually <10 cm^{-1} and only one band, corresponding to the frequency difference of the two lasers, is probed. To obtain large spectral bandwidth, a femtosecond Ti: sapphire laser (Coherent MIRA, 50 fs) is locked to a picosecond laser (HighQ Laser). This is achieved with an electronic synchronization unit from Coherent. The femtosecond laser output has a large FWHM spectral bandwidth of 240 cm^{-1} near 815 nm. Using an eight channel acousto-optic tunable filter (AOTF, Crystal Technology), the laser spectrum can be divided into as many as eight wavelength bands (Treado et al., 1992). The spectral resolution of the AOTF is 2.2 nm (or 33cm^{-1}). To reduce the effect of channel cross-talk, typically only three channels are used simultaneously in our experiments. The intensity of each wavelength band can be independently controlled and amplitude modulated using a home-built digital circuit driven by a single arbitrary function generator. We choose to modulate the three channels at 125 kHz, 100 kHz, and 75 kHz, respectively.

The key to the high sensitivity of SRS imaging is high frequency amplitude modulation, because solid state pulsed lasers have very low noise above 1 MHz. However, the modulation frequency of AOTF cannot go above 1 MHz. Therefore, we used a double-modulation technique with the picosecond beam (the Stokes beam) modulated at 20 MHz frequency using an electro-optical modulator (EOM) and the femtosecond beam (the pump beam) modulated at lower frequencies by the AOTF. On the detection side, only a single Si photodiode is needed and the signal is first demodulated at 20 MHz using a fast lock-in and then demodulated at lower

frequencies using a real-time digital Fourier transform. Because the digital demodulation is reasonably fast (>5 kHz), imaging can be performed using a galvo-scanner at sub-minute time scale.

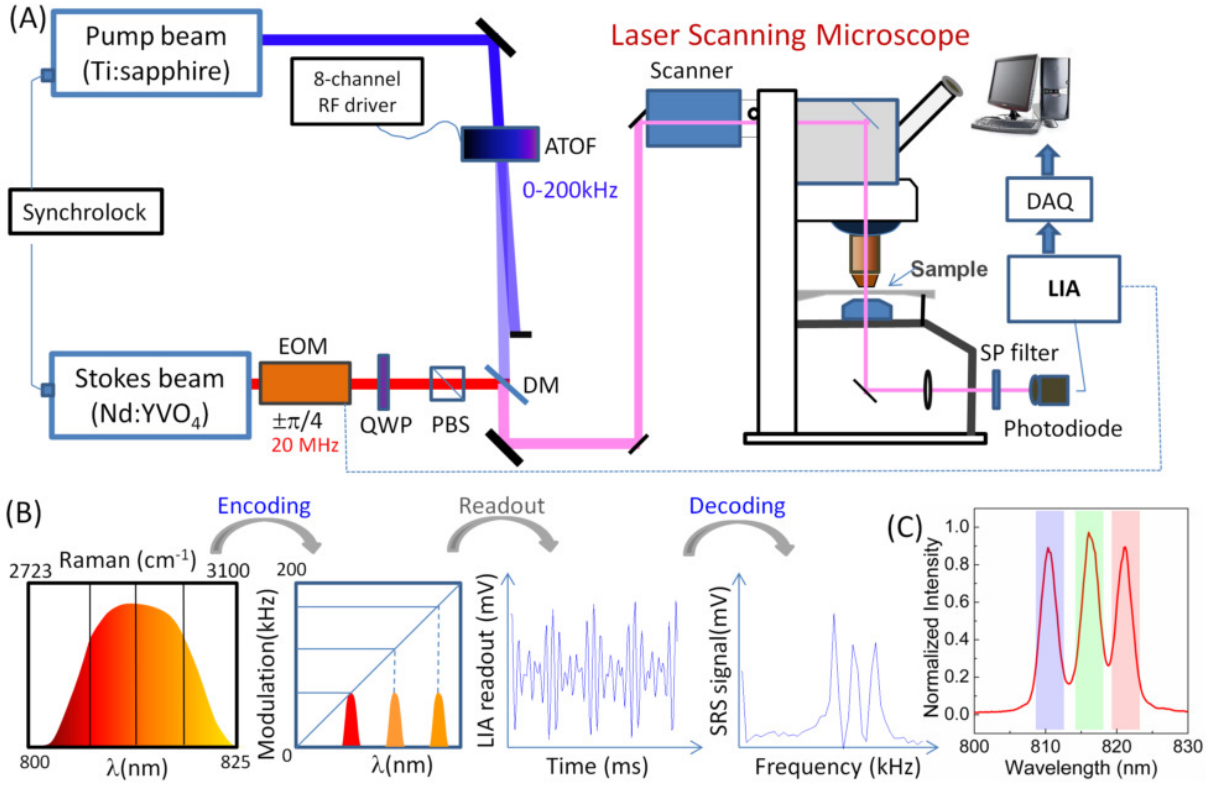

Figure 5.1 (A) Schematic diagram of multiplex SRS setup. HWP: half-wave plate; QWP: quarter-wave plate; EOM: electro-optical modulator; PBS: polarizing beamsplitter; DM: dichroic mirror; PMT: photomultiplier tube; LIA: lock-in amplifier.(B) Workflow of the multiplex Raman encoding and decoding process. (C) Example AOTF filtered spectrum using three channel modulation. Each shaded region corresponds to one channel modulated at a particular frequency.

We use an upright laser scanning microscope (Olympus FV300) for our solution measurement and imaging applications. The pump beam is detected in the transmission geometry. Signal from a 7.6 mm^2 silicon photodiode (Advanced Photonix) is fed into a homebuilt fast lock-in amplifier after passing through a 20MHz bandpass filter (BBP-21.4, Minicircuits) (Saar et al., 2010). The output from the lock-in amplifier is then digitized with a data acquisition card (DAQ, NI PCI-

6052E) at a rate of 320 kHz. A dual-core PC is used to perform real-time Fourier-transform on the streaming data from DAQ and extracts the amplitude components of signals at three different modulation frequencies.

5.2.2 Chemometrics Analysis

The chemometrics analysis is quite straightforward (Anton, 2005). Assume we have three chemical components (r, g, and b) in the sample. At any location in the sample, we measured SRS signal in three channels simultaneously (1, 2 and 3), we have the following equation:

$$\begin{aligned} S_1 &= C_r \sigma_{r1} p_1 + C_g \sigma_{g1} p_1 + C_b \sigma_{b1} p_1 \\ S_2 &= C_r \sigma_{r2} p_2 + C_g \sigma_{g2} p_2 + C_b \sigma_{b2} p_2 \\ S_3 &= C_r \sigma_{r3} p_3 + C_g \sigma_{g3} p_3 + C_b \sigma_{b3} p_3 \end{aligned} \qquad (1)$$

where S represents total SRS signal in one channel, C represents concentration, σ represents SRS cross-sections, p represents pump power. We neglected probe power and detection efficiency in equation (1) because they are the same for the three Raman bands. In any particular experiment, the power p1, p2, and p3 are fixed (roughly equal for the three channels) and therefore can be bundled together with the Raman cross-section σ to construct a calibration matrix, T, using the measured values from pure solutions:

$$T = \begin{bmatrix} \sigma_{r1} p_1 & \sigma_{g1} p_1 & \sigma_{b1} p_1 \\ \sigma_{r2} p_2 & \sigma_{g2} p_2 & \sigma_{b2} p_2 \\ \sigma_{r3} p_3 & \sigma_{g3} p_3 & \sigma_{b3} p_3 \end{bmatrix} \qquad (2)$$

With pure solutions with known concentrations for each species r, g or b, it is easy to determine each column of the calibration matrix T by dividing the three channels SRS signals with the concentration of that species. After we obtained calibration matrix T, we can calculate the SRS

signal in three channels for any combination of mixtures. Equivalently, from the measured SRS signals in the three channels, we can calculate the concentration of the three species in a mixture i using the inverse matrix:

$$\begin{bmatrix} C_r^i \\ C_g^i \\ C_b^i \end{bmatrix} = T^{-1} \begin{bmatrix} S_1^i \\ S_2^i \\ S_3^i \end{bmatrix} \quad (3)$$

The inverse matrix exists as long as the SRS cross-sections of any two species are not identical, which is typically the case in our experiments. This spectral unmixing can be done for every single pixel location in an inhomogeneous sample, thus allowing reconstruction of quantitative chemical maps for each individual chemical component. Because SRS is a nonlinear optical process, it has inherent optical sectioning similar to two photon fluorescence microscopy. Therefore, three dimensional high resolution chemical mapping can be performed as demonstrated in the skin imaging.

5.3 Results and Discussion

5.3.1 Quantification of Chemical Concentrations in Ternary Solution

We first demonstrate the quantitative determination of chemical concentrations of a ternary solution system. Mixtures of three chemicals: oleic acid, cholesterol, and cyclohexane, with significant Raman band overlap in the CH stretching region, are dissolved in deuterated chloroform. A total of 9 binary and 3 ternary mixtures were prepared. We chose three Raman Raman peaks to probe (2850, 2900, and 2960 cm^{-1}) based on their spontaneous Raman spectra (shown in Figure 5.2A). The power in each channel was 16 mW and the Stokes power was 76 mW at the objective focus. Standard linear algebra operation is used to calculate the binary and

ternary mixture concentrations based on measurements on single species. A ternary plot of the calculated concentrations is shown in Figure 5.2B.

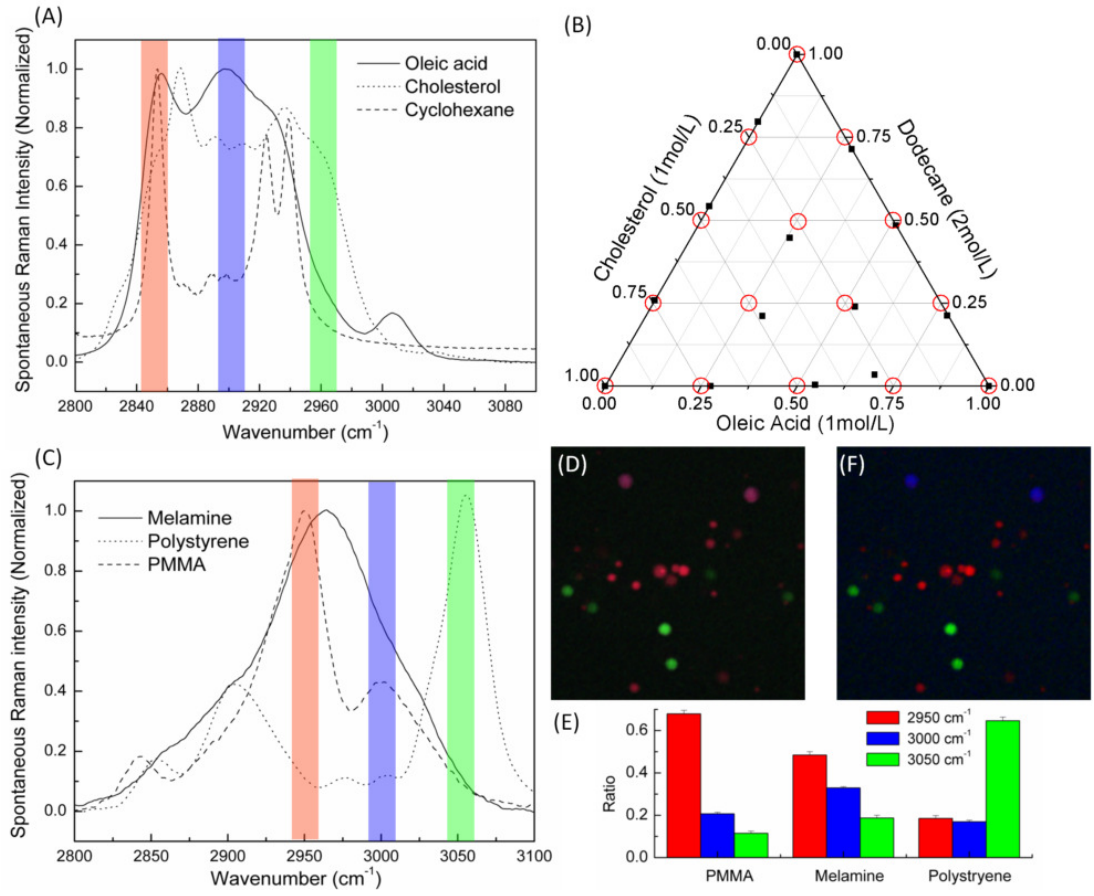

Figure 5.2 (A) Spontaneous Raman spectra of oleic acid, cholesterol, and cyclohexane. The red, blue and green lines indicate the location of the three Raman bands used for multiplex SRS imaging. (B) Ternary plot of the calculated concentrations of three component mixture based on multiplex SRS measurement on three Raman bands. (C). Spontaneous Raman spectra of melamine, PMMA, and polystyrene beads. (D) Raw composite image of three SRS images: red represents image at 2950 cm^{-1}, blue represents image at 3000 cm^{-1} and green represents image at 3050cm^{-1}. (E) Calibration bar graph of the normalized Raman intensities of each kind of bead at the designated three Raman band. (F) Reconstructed Raman image (red: PMMA, blue: melamine, and green: polystyrene).

We can see that the concentrations of most solutions are correctly inferred. The residual errors we see in the ternary plot are largely caused by femtosecond laser spectral drift during measurement, synchronization timing jitter, and the inaccuracy of matrix calibration due to the

cross-talk of the three channels caused by AOTF diffraction sidelobes. The measurement accuracy can be significantly improved if timing-jitter and cross-talk can be eliminated with better modulation technology.

We note that the multiplex data acquisition can be carried out at a rate > 5 kHz, at least two orders of magnitude faster than either conventional Raman imaging or multiplex CARS imaging. Moreover, for spatially segregated samples, calibration can be obtained *in situ* using the three channel images. To demonstrate this capability, we imaged mixtures of three different polymer beads embedded in agarose gel: 2 μm polystyrene (PS), 1-10 μm polymethyl methacrylate (PMMA) and 2 μm melamine. Three images (512×512 pixels with 200 μs pixel dwell time) are generated simultaneously.

Figure 5.2 (D) shows the composite image of three channels at 2950, 3000 and 3050 cm^{-1}, represented in red, blue and green color respectively. The red and blue channels exhibit small differences, due to the similar Raman spectra of melamine and PMMA. To distinguish them clearly, we first constructed the calibration matrix using *in situ* imaging data from three different kinds of beads and then applied the inverse matrix to the three channel image. Figure 5.2 (E) shows the normalized matrix value for the three different kinds of beads in bar graph. It agrees very well with that of spontaneous Raman spectra of the three species shown in Figure 5.2(C). The calculated concentration images are recompiled into a RGB composite image with each color showing one species (Figure 5.2 (F)). Different beads are now readily distinguished.

5.3.2 Multiplex SRS Imaging on Microalgae

In the first application, we demonstrate the use of multiplex SRS for studying microalgae biochemical composition, especially lipid content. The need for renewable energy sources has sparked growing interest in green algae oil production (Li et al., 2008; Mata et al., 2010). The

lipids (mainly triglyceride) stored in the microalgae could be converted into biodiesel efficiently. Various methods have been employed to evaluate the genetic and environmental factors that affect the oil producing capability of microalgae, but all have significant drawbacks. Fluorescent probes face problems such as nonspecific labeling, inaccuracy in quantification, photobleaching and phototoxicity (Elle et al., 2010). Traditional biochemical methods such as chromatography and mass spectrometry cannot analyze single cells and do not allow continuous *in situ* monitoring of oil accumulation. Most recently, Raman microspectroscopy has been used to study algal lipid composition but with very low throughput (Wu et al., 2011). CARS and SRS are excellent label-free alternatives to investigate lipid content because lipids are usually concentrated in droplets and have very strong Raman signal (Nan et al., 2006; Wang et al., 2011), but chlorophyll and carotenoids (both are referred to as pigment from here on), which are abundant in green algae, have strong two-color two-photon absorption (TPA) that interferes with Raman imaging. In addition, it is important to quantitatively separate protein from lipids, which is not possible with single Raman band imaging. TPA is a related nonlinear optical process that generates modulation signal in this pump-probe type imaging experiment, but it has much broader spectra response compared to Raman (Fu et al., 2007). With our new multiplex SRS approach, three channels can be used to separate pigment TPA, lipids SRS and protein SRS. Microalgae cultures were imaged at three different bands: 2780, 2850, and 2940 cm^{-1}. TPA contributes to all three channels due to its broad spectra response. At 2780 cm^{-1}, protein and lipid signals are almost negligible. At 2850 cm^{-1}, lipids have large Raman signal, and at 2940 cm^{-1}, both lipids and protein have strong Raman signals. We calibrated the signal distribution in three channels from protein and lipids using two prepared samples: one is 30% bovine serum albumin solution and the other is oleic acid liquid (Sigma). For pigment calibration we used the obtained

experimental images, similar to the calibration process used in the bead imaging. Cell cultures of *Botryococcus Braunii* microalgae are grown in modified bold 3N medium (both from UTEX). We compared two different lighting conditions: under continuous illumination versus a 12:12-h light: dark cycle. The optical power is lowered to 22 mW for the pump (all three channels) and 40 mW for the Stokes in order to minimize photodamage due to TPA. Figures 5.3(A) shows an example raw composite image of the SRS+TPA signal of microalgae. We can see that the pigment signal dominates all three channels, but is mostly located at the periphery of the cell in a clamshell shape, whereas lipid droplets are concentrated in the center of the cell. After spectra unmixing, the image clearly distinguishes the three major components (Figure 5.3(B)).

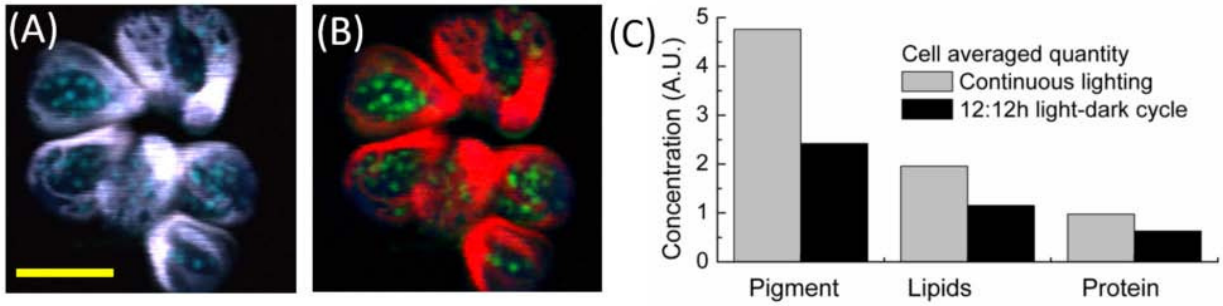

Figure 5.3 Multiplex SRS imaging of microalgal cells under different illumination conditions. (A) Raw composite images of microalgal cells at three bands: 2780 cm^{-1} (red), 2850cm^{-1} (green) and 2940 cm^{-1} (blue); (B) corresponding unmixed images: chlorophyll and carotenoids (red), lipids (green) and protein (blue); (C) bar graph of cell averaged concentration of pigment, lipids and protein for the two different samples. Scale bar: 10 μm.

We took a total of 15 frames for each sample (see Figure 5.4). With thresholding methods, the sizes of the cells were calculated. The average cell size for continuous illumination sample is much larger than that of 12:12h light: dark cycle sample lighting (Figure 5.4).

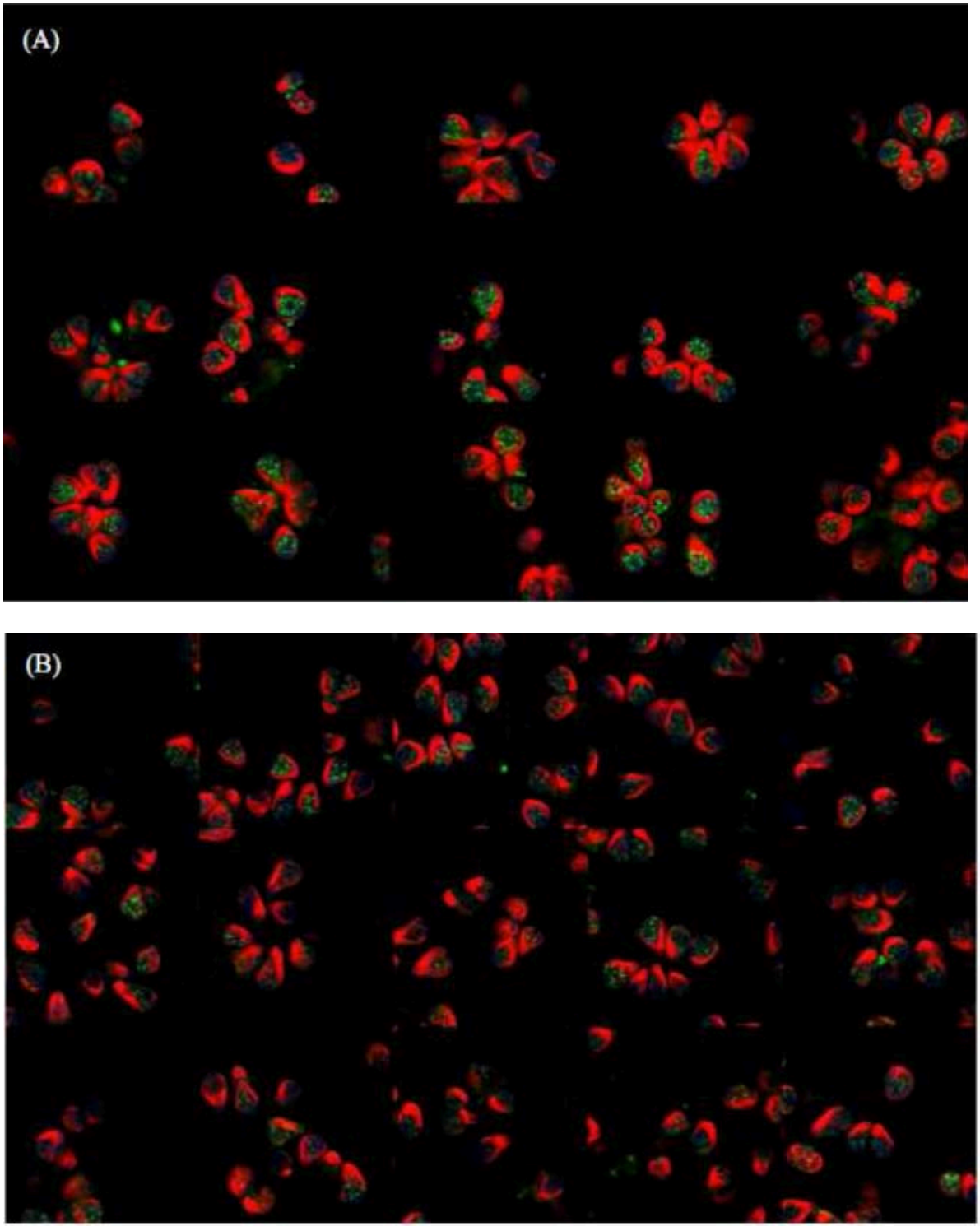

Figure 5.4 High resolution chemical image (15 frames mosaiced together, each frame is 512*512 pixels) of microalgae (A) grown under continuous lighting and (B) grown under 12:12h light: dark cycle. Red: chlorophyll and carotenoids; green: lipids; blue: protein.

It is known that algal cells under intense illumination could attain higher biomass compared with cells that had been adapted to low-level irradiance (Banerjee et al., 2002). To be more quantitative, we compared the cell averaged biomass for the two different types. Figure 5.3(C) shows the bar graph of the result. There is an increase in cellular concentration for all three components when microalgae are grown under continuous illumination. In particular, pigment increases by 95%, lipids by 68% and protein by 56%. The oil content can be gauged by the fraction of lipids mass in the total cell mass. We used the ratio of lipids to protein as a semi-quantitative measure of oil content. Clearly under continuous lighting, the lipids/protein ratio in the cell increases. This result is corroborated by other studies (Darzins et al., 2008; Fabregas et al., 2002). Interestingly, the pigment content increases the most. This is probably due to the adaptation of algal cells to light to increase photosynthetic activities.

5.3.3 Multiplex SRS Imaging of Mouse Skin

In the second application, we show that multiplex SRS could be used to study complicated biological samples where calibration of individual components is not easily available. In those cases, it is useful to use the spatial features of a sample to create pseudo-basis sets (assuming selected spatial locations have only one of the three major components) and use the images themselves to construct the calibration matrix. Consequently, the calculated images may not reflect the relative concentrations of each individual chemical component, but should still reflect the contributions of the major components. To demonstrate this, we imaged the 3D structure of mouse skin tissue. Skin has very complicated structure and compositions, providing both barrier and transport functions. These functions are intimately associated with vasculature and lipids. As discussed previously, the 2850 cm^{-1} channel mainly has contribution from lipids, while the 2940 cm^{-1} channel has contributions from both lipids and proteins (Saar et al., 2010). The 2780 cm^{-1}

channel is off Raman resonance and provides contrast for two-color TPA of hemoglobin, a key species that allows visualization of blood vessels (Fu et al., 2008; Fu et al., 2007). By using an independent channel to characterize the contribution from blood, together with lipids and protein SRS signals, we can disentangle major biochemical composition of different skin layers. The calibration matrix is obtained by picking specific regions with features corresponding to protein layer, blood vessels and subcutaneous fat layers based on raw composite images at different imaging depth. After reconstruction, Figure 5.5 shows spectrally separated blood (red), lipids (green) and protein (blue) images at increasing imaging depths with 6 μm depth increment.

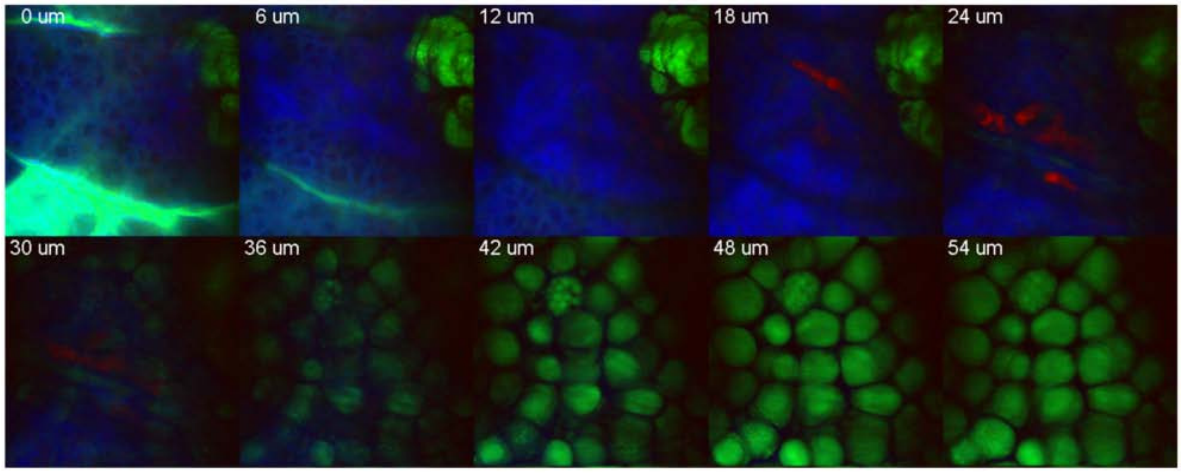

Figure 5.5 Multiplex SRS z stack images of freshly excised mouse ear skin: red - blood contrast, green - lipid contrast, and blue - protein contrast. Each image is 512×512 pixels.

Qualitatively, we can observe spatially distinctive features for blood vessels at a depth of around 15-30 μm. The lipid layer on the surface and the fat layer in the hypodermis can be clearly identified. We can also see that in the epidermis, there are many large cell nuclei (with characteristic low lipid concentration), and some have visible nucleoli as marked by higher protein content. Within the fat cell layer, some fat cells are surrounded by large numbers of much smaller lipid droplets. Those exquisite features are indications of the high sensitivity and spatial

resolution of our multiplex SRS method. This capability offers the potential of label-free real-time digital pathology.

5.4 Conclusion

In conclusion, we present multiplex SRS imaging using a novel modulation multiplex approach. Double modulation and double demodulation are employed to achieve high speed and high sensitivity. Combining the advantage of high speed label-free imaging and the chemical fingerprinting power of Raman spectroscopy, multiplex SRS is a powerful and quantitative method for fast label-free chemical composition analysis in biological systems. Absorption and fluorescence, which are typically major deterrents for spontaneous Raman based applications, did not cause problems in our measurements. In fact, we can use the TPA of pigments or hemoglobin as an independent parameter to evaluate the growth condition of algal cells and visualizing blood vessels, respectively. The speed of multiplex SRS is currently limited by the modulation speed of AOTF, but can be further improved by two orders of magnitude (500 kHz) with other technologies such as a multichannel acousto-optical modulator. Using such a modulator, the sensitivity and measurement accuracy could also be significantly improved as a result of better resolution (possibly <15 cm^{-1}) and larger number of channels (up to eight or sixteen, depending on models). The number of components that can be analyzed increases linearly with the number of spectral channels.

Our demonstrated applications are focused on the C-H stretching region because C-H stretching offers strong SRS signal and it is critical to have multiplex SRS for discriminating different species in this strongly congested vibrational region. Eight-channel or sixteen-channel SRS could enable quantification of different lipid species such as triglycerides and cholesterol esters. Extending multiplex modulation to the fingerprint region is straightforward by tuning the

Ti: sapphire laser to >900 nm. The SNR of multiplex SRS is only slightly degraded in comparison to narrowband SRS due to cross-talk. Therefore, all previous coherent Raman applications demonstrated in the fingerprint region can be better implemented by multiplex SRS with better chemical specificity and quantitative multi-component analysis. It is worth mentioning that there is a delicate balance between laser bandwidth, number of spectral channels and spectra information. Ideally the larger the spectral bandwidth and the number of channels, the better selectivity can be achieved. However, the laser power at each individual band is going to be limited, resulting in corresponding degradation of SNR. With proper design, we believe that multiplex SRS has enormous potential as a label-free chemical imaging approach for studying complex systems. It will find important applications in lipid biology studies and biomedical imaging.

References

Anton, H. (2005). Elementary Linear Algebra, 9th ed, Wiley.

Banerjee, A., Sharma, R., Chisti, Y., and Banerjee, U.C. (2002). Botryococcus braunii: A renewable source of hydrocarbons and other chemicals. Crit Rev Biotechnol *22*, 245-279.

Cheng, J.-x., Volkmer, A., Book, L.D., and Xie, X.S. (2002). Multiplex Coherent Anti-Stokes Raman Scattering Microspectroscopy and Study of Lipid Vesicles. J Phys Chem B *106*, 8493-8498.

Darzins, A., Hu, Q., Sommerfeld, M., Jarvis, E., Ghirardi, M., Posewitz, M., and Seibert, M. (2008). Microalgal triacylglycerols as feedstocks for biofuel production: perspectives and advances. Plant J *54*, 621-639.

Elle, I.C., Olsen, L.C.B., Pultz, D., Rodkar, S.V., and Fargeman, N.J. (2010). Something worth dyeing for: Molecular tools for the dissection of lipid metabolism in Caenorhabditis elegans. FEBS Letters *584*, 2183-2193.

Fabregas, J., Maseda, A., Dominguez, A., Ferreira, M., and Otero, A. (2002). Changes in the cell composition of the marine microalga, Nannochloropsis gaditana, during a light : dark cycle. Biotechnol Lett *24*, 1699-1703.

Freudiger, C.W., Min, W., Holtom, G.R., Xu, B., Dantus, M., and Sunney Xie, X. (2011). Highly specific label-free molecular imaging with spectrally tailored excitation-stimulated Raman scattering (STE-SRS) microscopy. Nat Photon *5*, 103-109.

Fu, D., Matthews, T.E., Ye, T., Piletic, I.R., and Warren, W.S. (2008). Label-free in vivo optical imaging of microvasculature and oxygenation level. J Biomed Opt *13*, 040503.

Fu, D., Ye, T., Matthews, T.E., Chen, B.J., Yurtserver, G., and Warren, W.S. (2007). High-resolution in vivo imaging of blood vessels without labeling. Opt Lett *32*, 2641-2643.

Kano, H., and Hamaguchi, H. (2005). Ultrabroadband (> 2500 cm(-1)) multiplex coherent anti-Stokes Raman scattering microspectroscopy using a supercontinuum generated from a photonic crystal fiber. Appl Phys Lett *86*, 121113.

Li, Y., Horsman, M., Wu, N., Lan, C.Q., and Dubois-Calero, N. (2008). Biofuels from Microalgae. Biotechnol Progr *24*, 815-820.

Mata, T.M., Martins, A.A., and Caetano, N.S. (2010). Microalgae for biodiesel production and other applications: A review. Renewable and Sustainable Energy Reviews *14*, 217-232.

Muller, M., and Schins, J.M. (2002). Imaging the thermodynamic state of lipid membranes with multiplex CARS microscopy. J Phys Chem B *106*, 3715-3723.

Nan, X., Potma, E.O., and Xie, X.S. (2006). Nonperturbative Chemical Imaging of Organelle Transport in Living Cells with Coherent Anti-Stokes Raman Scattering Microscopy. Biophysical Journal *91*, 728-735.

Saar, B.G., Freudiger, C.W., Reichman, J., Stanley, C.M., Holtom, G.R., and Xie, X.S. (2010). Video-Rate Molecular Imaging in Vivo with Stimulated Raman Scattering. Science *330*, 1368-1370.

Wang, M.C., Min, W., Freudiger, C.W., Ruvkun, G., and Xie, X.S. (2011). RNAi screening for fat regulatory genes with SRS microscopy. Nat Meth *8*, 135-138.

Wu, H., Volponi, J.V., Oliver, A.E., Parikh, A.N., Simmons, B.A., and Singh, S. (2011). In vivo lipidomics using single-cell Raman spectroscopy. PNAS *108*, 3809-3814.

Part II (Chapter 6-7)

Single Cell Transcriptome Analysis of Mouse Retina

Functional studies on nervous systems are essential for our understanding of human sensation, memory and behavior. Retina system is relatively well defined compared to other nervous systems due to its laminated structure. Retinal cells transmit electrical signal through several layers and eventually pass on to the central neurons connected to the brain. The wiring of retinal cells is extremely important and regulates different functions of the system. There has been extensive study on the electrophysiology aspect on this system. Molecular profiling is needed for the better understanding of the wiring mechanism.

Recently Multiple Annealing Looping Based Amplification Cycles (MALBAC) is developed, which enables the whole genome amplification of a single cell (Zong et al., 2012). Combined with reverse transcription reaction prior to this procedure, a whole transcriptome amplification method is also developed (Chapman et al., 2015). This technique is superior to other single cell transcriptome techniques with its high reproducibility rate and low dropout rate. This enables us to get the transcriptome information in each individual retinal cell for the classification of different cell populations as well as previously undefined subpopulations.

In Chapter 6, we demonstrate the capability of MALBAC-RNA-seq for classifying different retinal cell populations (photoreceptors and retinal ganglion cells) and subpopulations (different direction selective retinal ganglion cells) using principal component analysis and hierarchical clustering of the amplified single cell transcriptome data.

In Chapter 7, we use a similar approach to solve an unclear wiring problem in the movement

direction sensing function by identifying the molecular divergence of ON-OFF starburst amacrine cell (SAC) sublaminae. We identified two distinct clusters of SACs based on their single cell transcriptome data and reported differentially expressed genes. The *in situ* immunostaining results have demonstrated the strong correlation of this clustering result and the ON-OFF functional difference with more follow-up functional study to be continued by Dr. Yirong Peng in Prof. Joshua Sanes' lab, who is the major collaborator on this project.

Contributions

This part of the thesis involved close collaboration with Dr. Yirong Peng in Prof. Joshua Sanes' group.

In Chapter 6: Single cell transcriptome analysis of photoreceptor and retinal ganglion cells in mouse, I, Dr. Yirong Peng, Prof. Xie and Prof. Sanes conceived the idea and designed the experiments. I and Dr. Yirong Peng conducted the experiments (Dr. Yirong Peng conducted mouse retina dissection and FACS sorting. I conducted single cell transcriptome amplification based on MALBAC technique, purification, quality control using qPCR and library preparation for sequencing.) Alec R. Chapman, I and Dr. Yirong Peng analyzed data.

In Chapter 7: Decoding the molecular divergence of the ON-OFF retinal circuit, Dr. Yirong Peng, I, Prof. Sanes and Prof. Xie conceived the idea and designed the experiments. I and Dr. Yirong Peng conducted the experiments (I conducted single cell transcriptome amplification based on MALBAC technique, purification, quality control using qPCR and library preparation for sequencing, Dr. Yirong Peng conducted mouse retina dissection, FACS sorting and immunostaining experiments.) Dr. Yirong Peng and I analyzed the data. Alec R. Chapman and Guangyu Zhou helped with some analysis.

Chapter 6

Single Cell Transcriptome Analysis of Photoreceptor and Retinal Ganglion Cells in Mouse

6.1 Background

6.1.1 Overview of Retina System

Understanding the nervous system in mammalians is a long-standing question involving billions of neurons with complicated wiring mechanism. The circuit wiring mechanism is very important for the understanding of mammalians' cognition, memory and behaviors, yet still very little is known due to limited technological approaches. Retina system, one part of the central nervous system, is as complex as other parts, but its features of regular laminar structure, compactness and easy physical accessibility give scientists great opportunities to study the circuit formation (Sanes and Zipursky, 2010). The visual information input consists of multidimensional features such as color, shape and motion and it is encoded and sent to the brain in a parallel processing fashion (Nassi and Callaway, 2009). The complex visual input in the function of a light pattern (position, wavelength and time) is first projected to the outer layer of retina as a 2D photoreceptor array and converted into electrochemical signal being passed through several hundred micrometers of retina to the brain (Rodieck, 1998). There are at least 80 different neuron cell populations, which are characterized based on anatomical structure and physiological response. It is also considered that there are 20 distinct circuits in the retina comprising a dozen parallel pathways at least signaled to the central brain for post processing (Dacey, 2004). The relevant information is further extracted and integrated by the visual cortex and a unified and coherent perception is generated.

Retina is organized in a laminar structure with three separate nuclear layers containing cell bodies without synapses (Sanes and Zipursky, 2010). There are 6 major cell types in these retinal layers: photoreceptors in the outer nuclear layer; interneurons (horizontal, bipolar and amacrine cells) and Muller glia cells in the inner nuclear layer; retinal ganglion cells or RGCs and some amacrines in the ganglion cell layer (Masland, 2001; Wassle, 2004). In between these nuclear layers are two plexiform layers containing synapses without cell bodies (Figure 6.1). This is a simplified view of the retina structure. In real systems, each major cell type is further divided into multiple subtypes based on physiological, structural and molecular differences. The plexiform layers can also be further divided into sublaminae.

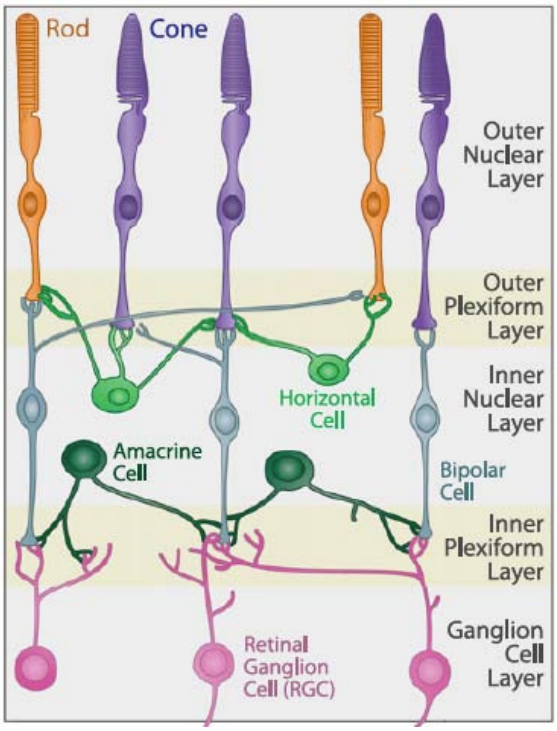

Figure 6.1 Mammalian retina structure (Sanes and Zipursky, 2010)

Retinal ganglion cells (around 1.5million in human retina) are very essential, forming the optic nerve and connecting the eye to the brain (Nassi and Callaway, 2009). As the retinal output, the ganglion cell arrangement needs to be very compact due to the anatomical bottleneck of the optic

nerve. Therefore mammalian visual systems incorporate the strategy of reducing the features of visual input to a smaller dimension of specialized and parallel output channels. There are at least 17 different ganglion cell types with each type tiling the retina and conveying different aspects of the visual input in parallel to the brain simultaneously (Dacey, 2004). One important feature studied more in detail in our work is the perception to motion direction. The ganglion cells responsible for this feature are termed as direction-selective ganglion cells (DSGCs) (Barlow and Levick, 1965). There are four types of DSGCs with each type responding to motion in each of the four cardinal directions (ventral, dorsal, temporal and nasal). Each type of ooDSGCs responds robustly with maximum number of spikes in the electrophysiology tests when the visual stimulus is moving in their preferred direction, and responds minimally (with minimal firing activity) to the opposite (or null) direction (Wei and Feller, 2011). In our following study, Drd4-GFP (nasal-preferring) (Huberman, et al., 2009) and Hb9-GFP (temporal-preferring) (Trenholm, et al., 2011) subsets are used under investigation.

6.1.2 Whole Transcriptome Amplification and Sequencing of Single Cells

Molecular signature is becoming more crucial for the understanding of circuit formation in retina. Classifying the recognition molecules can give more indication to the connectivity between cells. Currently classification is incomplete and molecular markers are not available for some subtypes. Therefore a technique to read out the genetic profile of an individual cell is needed. Currently technologies such as fluorescence *in situ* hybridization (FISH) (Raj et al., 2006; Taniguchi et al., 2010; Topalidou et al., 2011), Quantitative reverse-transcription polymerase chain reaction (qRT-PCR) (Bengtsson et al., 2005; Diehn et al., 2009; Guo et al., 2010; Sanchez-Freire et al., 2012; Warren et al., 2007) and microarray(Brown and Botstein, 1999; DeRisi et al., 1997) can help identify specific mRNA targets in cells and tissues. However

the throughput is still very low and inefficient for a large number of genetic targets. Therefore a whole transcriptome sequencing technique is needed for both higher accuracy and wider dynamic range. Moreover, the stochasticity of mRNA expression leads to cell-to-cell variation. Therefore single cell transcriptome measurement is highly demanded. However, the mRNA amount in a single cell is much lower than the sequencing analysis threshold. Therefore amplification of single cell RNA is required and there are several techniques developed towards this goal.

PCR has been widely used to amplify molecules into bigger amount (Saiki et al., 1988), but the bias/unevenness is big due to the kinetic variations in the first several PCR amplication cycles (Shiroguchi et al., 2012). The first demonstrated single-cell transcriptome sequencing technique is based on a PCR amplification scheme using the terminal transferase before the second strand synthesis (Tang et al., 2010; Tang et al., 2009). This technique has amplification bias towards 3' ends and short transcripts. Moreover, the efficiency is limited due to multiple steps before making a full amplicon. Later techniques were developed based on a reverse transcriptase with template-switching activity (Islam et al., 2011, 2012; Picelli et al., 2013; Ramskold et al., 2012). Transcriptome profiling of human embryors (Xue et al., 2013) and mouse bone-marrow-derived dendritic cells (Shalek et al., 2013) were demonstrated using these techniques. Although the coverage is improved, the low amplification reproducibility is still a problem especially for genes with low expression levels. Cel-seq was later developed using in-vitro transcription (IVT) in stead of PCR (Hashimshony et al., 2012) enabling multiplex amplification but the bias on 3' end of the transcripts is still significant.

Recently, multiple annealing and looping-based amplification cycles (MALBAC) method has been developed for single cell whole genome amplification (Zong et al., 2012). This technique is

based on a quasi-linear instead of exponential amplification approach, which enables it to reduce the amplification bias significantly compared to previous whole genome amplification techniques base on MDA (Dean et al., 2001). Based on this genome amplification method, a single-cell transcriptome amplification method was developed and termed as MALBAC-RNA amplification (Chapman et al., 2015).

The amplification scheme is presented in Figure 6.2, individual cells are placed into separate PCR tubes preloaded with cell lysis buffer. After performing cell lysis at 70°C for 90 seconds, mRNA is reverse transcribed to complimentary DNAs (cDNAs). Oligo (dT) primer is used in the reverse transcription step to extract mRNA transcripts from other functional RNAs.

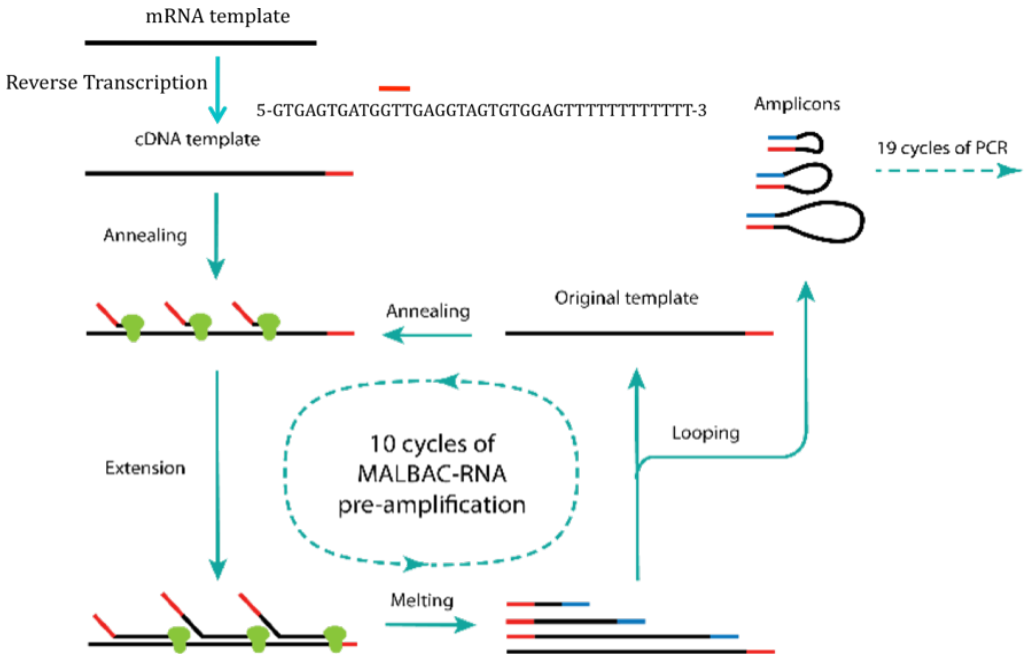

Figure 6.2 Single cell MALBAC-RNA amplification scheme (Chapman et al., 2015)

The cDNA synthesis is then followed by further amplification steps similar to MALBAC-DNA (Zong et al, 2012). A 34-nucleotide sequence primer is used for the first amplication step combining the 27-nucleotide sequence in the poly-T primer together with 7 random nucleotides. These primers are considered to randomly/evenly hybridize to the template cDNA at 4°C.

Second strand cDNA synthesis starts when temperature is increased to 65^{o}C. Deep VentR (exo-) DNA polymerase with strand displacement activity is used, allowing the primers to displace the downstream primers as it proceeds along the template and generating longer synthesized products. Each newly synthesized cDNA contains a 27-nucleotide tag at its 3'end while reaching the end of the extension on the template, which is complementary to its 5' end. The cDNAs leave the template as the temperature is increased to 95^{o}C and the two ends of the amplified products hybridize together at 58^{o}C to form a loop with a small spatial dimension avoiding the further amplification based on these products. This ensures all the following rounds of amplification to be based on the original template instead of the synthesized products from the previous rounds, which leads the amplification to a close-to-linear process with less bias. The first round of amplification contains a total of 10 cycles to generate enough amplicons for the following PCR step (19 cycles of PCR amplification using primers with the same 27-base common sequence). The final yield of cDNA amounts to 100ng to 1ug depending on the original mRNA amount.

MALBAC-RNA-Seq demonstrates high reproducibility and sensitivity, especially for low abundant genes (Chapman et al., 2015). This is essential for our study on the retina system as some cells of interest such as photoreceptors are relatively smaller with fewer transcripts. Therefore we plan to use MALBAC-RNA-Seq to acquire the whole transcriptome information of individual retinal cells and perform functional studies on them. We first plan to test the feasibility of this approach by applying it on known cell populations and checking if the distinct populations can be differentiated.

6.2 Methods and Materials

6.2.1 Experimental Workflow

The experimental workflow is demonstrated in Figure 6.3. The transgenic mouse (Hb9 or Drd4)

at postnatal day 6 (P6) or day 15 (P15) was sacrificed and each retina was dissociated separately using papain. After the dissociation, the cell density was checked before it was suspended in MEM and sent to flow cytometer for single cell isolation (details discussed in 6.2.2). The individual cells were isolated into 0.2mL PCR tubes each of which is filled with 5 microliter aliquot of cell lysis buffer. We then performed reverse transcription and MALBAC amplification on the isolated cells in separated tubes as described in 6.1.2. The amplified cDNAs were purified and tested with gel electrophoresis and qPCR on marker genes for quality control. We conducted library preparation only on those good quality samples and we pooled the samples with distinct barcodes together and sent it to Illumina high throughput sequencers.

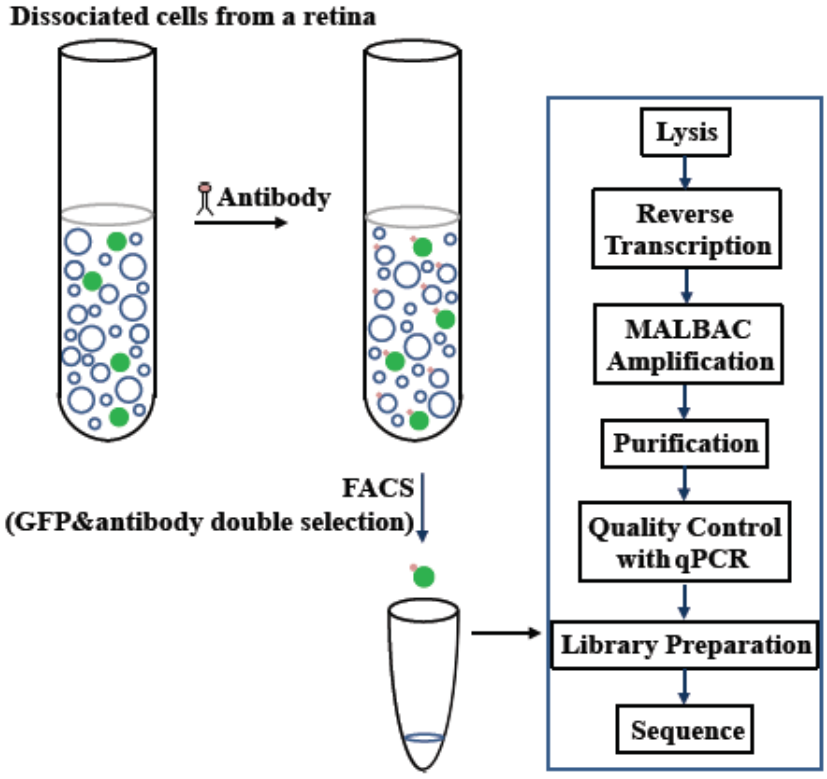

Figure 6.3 Experimental workflow

6.2.2 Fluorescence-activated Cell Sorting

We isolated Hb9 photoreceptor cells, retinal ganglion cells (RGC) and Drd4 retinal ganglion

cells at age P6 and P15 using fluorescence-activated cell sorting (Figure 6.4). The cells were isolated based on size (FSC channel), granularity (SSC channel), singularity (pulse width channel) GFP signal (FL1 channel) and Thy1 expression (FL4 channel). Thy1 expression is read out by the PE/Cy7 conjugated to the antibody of Thy1. In the transgenic mouse line Hb9::eGFP, only photoreceptors and RGCs express GFP. The RGCs were further selected based on Thy1+ expression and photoreceptors were isolated based on Thy1- FACS gating. In the transgenic mouse with GFP expressed under the control dopamine receptor 4 promoter (Drd4-EGFP) (Gong et al., 2003), GFP+ cells are found to be only present in the ganglion cell layer (Huberman et al., 2009). Therefore Drd4 RGC cells were isolated based on GFP+ and Thy1+ for double confirmation.

Table 6.1 Summary of the cell types for FACS

Cell types labeled	Mouse line	FACS purification
Cone photoreceptors	**Hb9:GFP**	GFP^+ and anti-$Thy1.2^-$
ooDSGCs (Ventral)		GFP^+ and anti-$Thy1.2^+$
ooDSGCs (Nasal)	**Drd4:GFP**	GFP^+ and anti-$Thy1.2^+$

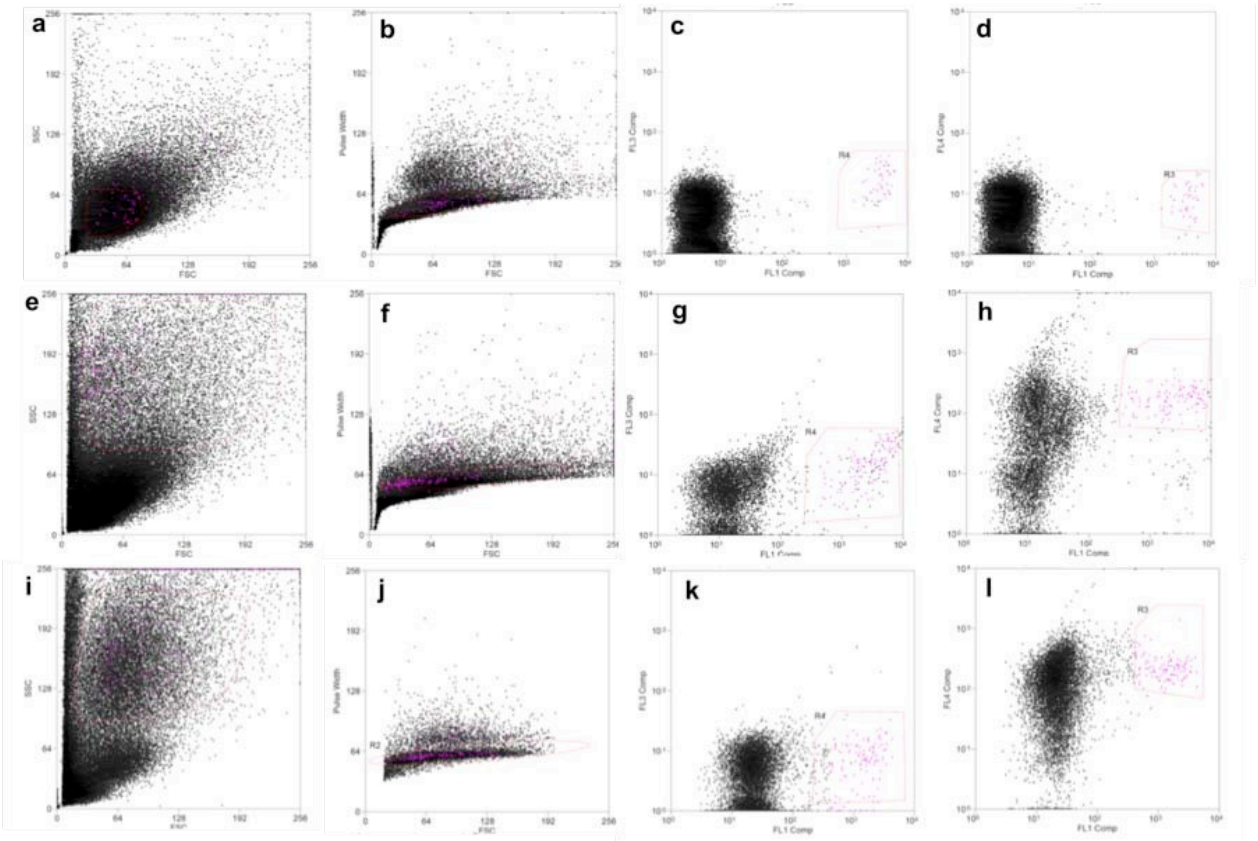

Figure 6.4 Gating panels on FACS, fluorescence-activated cell sorting. (a)-(d) Hb9 photoreceptors. (e)-(h) Hb9 retinal ganglion cells. (i)-(l) Drd4 retinal ganglion cells. FSC: forward scattering channel; SSC: side scattering channel; FL1: GFP; FL4: PE/Cy7. The first column represents the size and granularity of all sorted events. The gate in the second column selects the single cell events only. The gate in the third column selects out GFP-positive cells. The gate in the fourth column selects out Thy1-positive cells (RGCs) or Thy1-negative cells (photoreceptors).

6.2.3 MALBAC-RNA Amplification

We followed the single cell transcriptome amplification protocol based on MALBAC described in (Chapman et al., 2015). We lysed the isolated cells using detergent IGEPAL CA-630. This detergent does not interfere with the subsequent reverse transcriptional process so there is no need to remove it after the lysis step. For the reverse transcription step, we used Superscript III, which has been reported to potentially generate full length cDNAs of 10 kilobases (Kurimoto, et al., 2006; Tang et al., 2009; Taniguchi et al., 2009). We then conducted 10 cycles of MALBAC

using deep vent (exo-) DNA Polymerase, which has strand displacement function. After that, we conducted 19 cycles of PCR amplification. Amplified cDNA products were purified with Zymo DNA Clean & Concentrator-5 and eluted into 30uL EB buffer. These amplified DNA products were directly used for standard Illumina HiSeq library preparation.

6.2.4 Quantitative PCR

The qPCR were performed by 7500 Fast real time PCR system (Applied Biosystems, MA, USA). Each 20uL reaction comprised of 10mL qPCR Master Mix 2x, 0.4uL Rox dye 50X (Thermo Scientific), 0.2uL primer (100uM) and 1uL purified cDNA amplicons and 8.4uL DEPC treated water. The PCR procedure comprised a 10 min 95^{o}C hot start followed by 40 cycles of amplification (95 ^{o}C denaturation for 15s and 60 ^{o}C annealing/extention for 1min)..

6.2.5 Data Analysis

The sequencing output reads were aligned to the mm9 reference genome using Tophat 2.0.4 (Kim et al., 2013). We used Cufflinks 2.0.1 to estimate FPKM values (Trapnell et al., 2013). Pincipal-component analysis (PCA) and hierarchical clustering analysis were performed in R and Matlab. Differential gene analysis was performed using CuffDiff (Trapnell et al., 2013) and the gene expression heat map on these genes was performed in Matlab and R.

6.3 Results and Discussion

Photoreceptors and ganglion cells are located in two distinct layers spaced by another nuclear layer and two plexiform layers. The functions and morphology are also very different and they do not connect to each other directly. Therefore the difference in their molecular profiles is considered to be bigger than that between other cell types/subtypes in the retina. We first test the feasibility of our techniques on these two cell types and perform blind clustering analysis based on the acquired transcriptome data. We also include the two subtypes of direction selective

ganglion cells (DSGCs): Hb9 RGC responding to motion in ventral direction and Drd4 RGC responding to motion in nasal direction.

40 individual cells of photoreceptors and retina ganglion cells in two age groups of postnatal day 5 and day 15 were included in the analysis. After acquiring the amplified cDNA using MALBAC-RNA-Seq, qPCR (quantitative PCR) was performed for home keeping gene Gapdh and marker genes for each type (Thy1 for RGCs and Arr3 for photoreceptor cells). Figure 6.5a shows the immunostaining results confirming the marker gene expression in photoreceptor cells (Arr3) and RGCs (Thy1). The co-localization of GFP and Arr3 in photoreceptor cells, GFP and Thy1 in RGCs were observed. Figure 6.5 b shows the relative Ct count (compared to home keeping gene Gapdh) for maker genes of photoreceptor (Arr3) and maker gene of ganglion cells (Thy1).

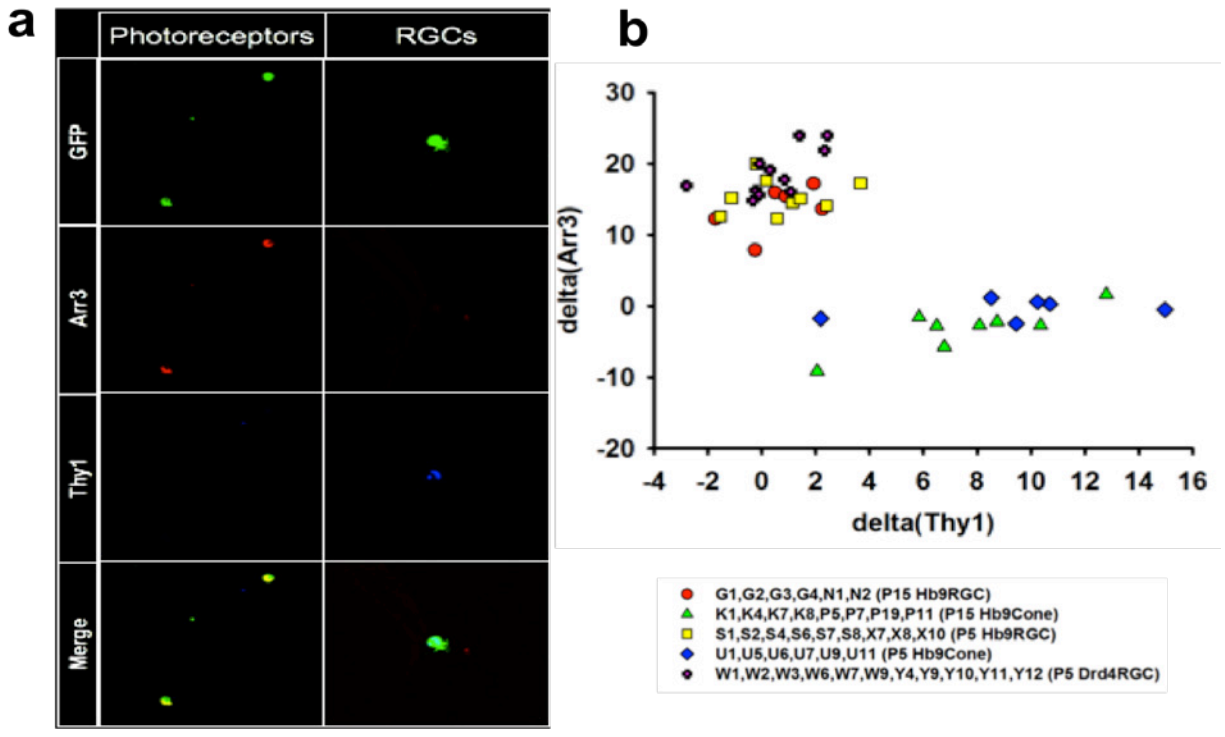

Figure 6.5 (a) Immunostaining results of Hb9 photoreceptor cells and retina ganglion cells; (b) Relative Ct number for Thy1 and Arr3 (subtracted by the Ct number of Gapdh) based on qPCR results of amplified cDNAs.

As we can see here, most of the retinal ganglion cells have high Ct number in Arr3 (low gene expression level) while photoreceptor cells have low Ct numbers (high gene expression level) for these genes, which is consistent with the immunostaining results (Figure 6.5a). On the other hand, Thy1 is highly expressed in ganglion cells but not photoreceptor cells. The qPCR result serves as one quality control method combined with Qubit for the yield checking and gel electrophoresis for the length distribution checking.

The cells passing the quality control were prepared as sequencing library and sent to the Illumina Hi-Seq 2500. The cluster density plot of the sequencing data is shown in Figure 6.6.

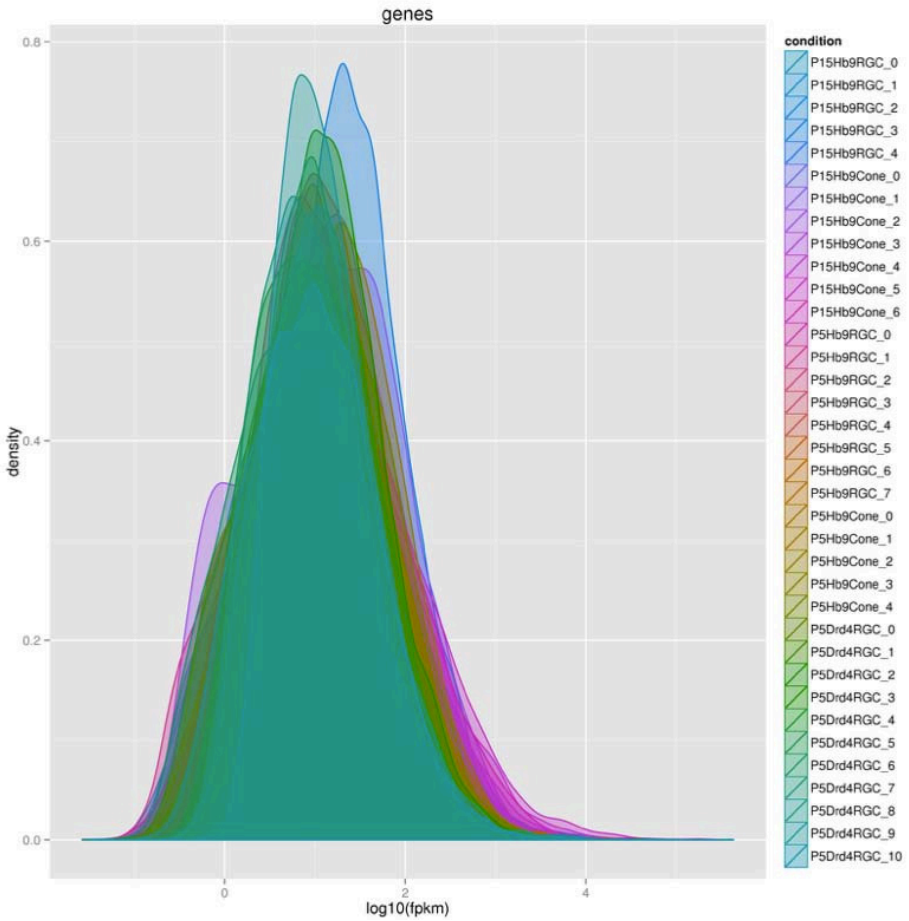

Figure 6.6 Cluster density plot of the sequencing data of individual cells

The cluster density can be understood as a smoothed representation of a histogram. It is based on

the Kernel density estimation, a non-parametric way to estimate the probability density function of a random variable. This graph indicates the sequence data quality. All samples cluster in similar ranges, indicating no weird sequenced samples.

The FPKM of marker genes are plotted in Figure 6.7. Photoreceptor cells exhibit high FPKM value in Arr3 and low value in Thy1, which is opposite with retinal ganglion cells. The results are consistent with qPCR result shown in Figure 6.5b.

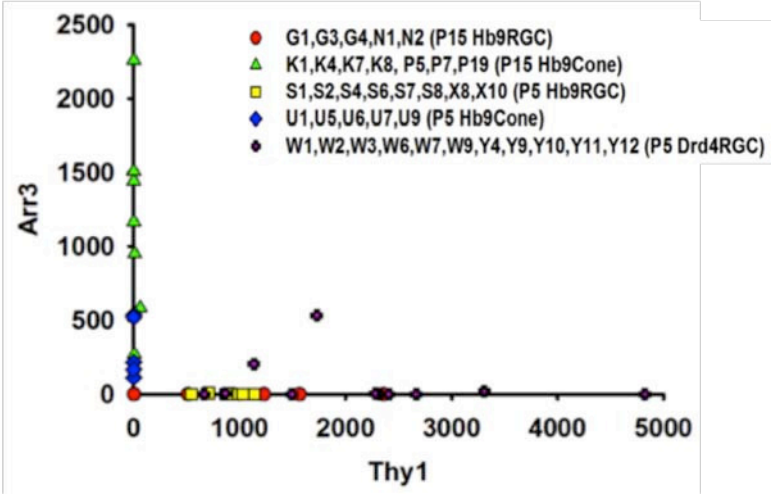

Figure 6.7 FPKM values of Thy1 and Arr3 across sequenced samples

The heat map on the expression level of more known marker genes and control genes is shown in Figure 6.8. The results are mostly consistent with previous reported discoveries, reassuring our data quality. Opn1sw (opsin1, cone pigment, short-wave-sensitive) and opn1mw (opsin 1, medium-wave-sensitive) responsible for color vision are specifically expressed only in photoreceptors.

A principle component analysis was performed on all the genes detected across all the measured samples as shown in Figure 6.9. PCA helps visualization by compressing multi-dimensional information in the data set (m cells each with n genes give m x n dimension data set) down to two or three dimensions. Data points represented by eigen values (magnitude) and an

eigen vectors (direction) are projected onto an axis to give the largest variance along the line. This axis is indicated as the principal component one. Principle component two, orthogonal to the first principal component, is the axis upon which the next largest variance is achieved. The distance between the data points indicates the degree of genetic difference between samples. As we see here in Figure 6.9, photoreceptors cluster nicely together, which are separated from ganglion cells belonging to another cluster. Furthermore, age difference is also exhibited as distinct clusters of P5 and P15 photoreceptor cells. The two subtypes of ganglion cells are also clustered at different locations on the PCA plot.

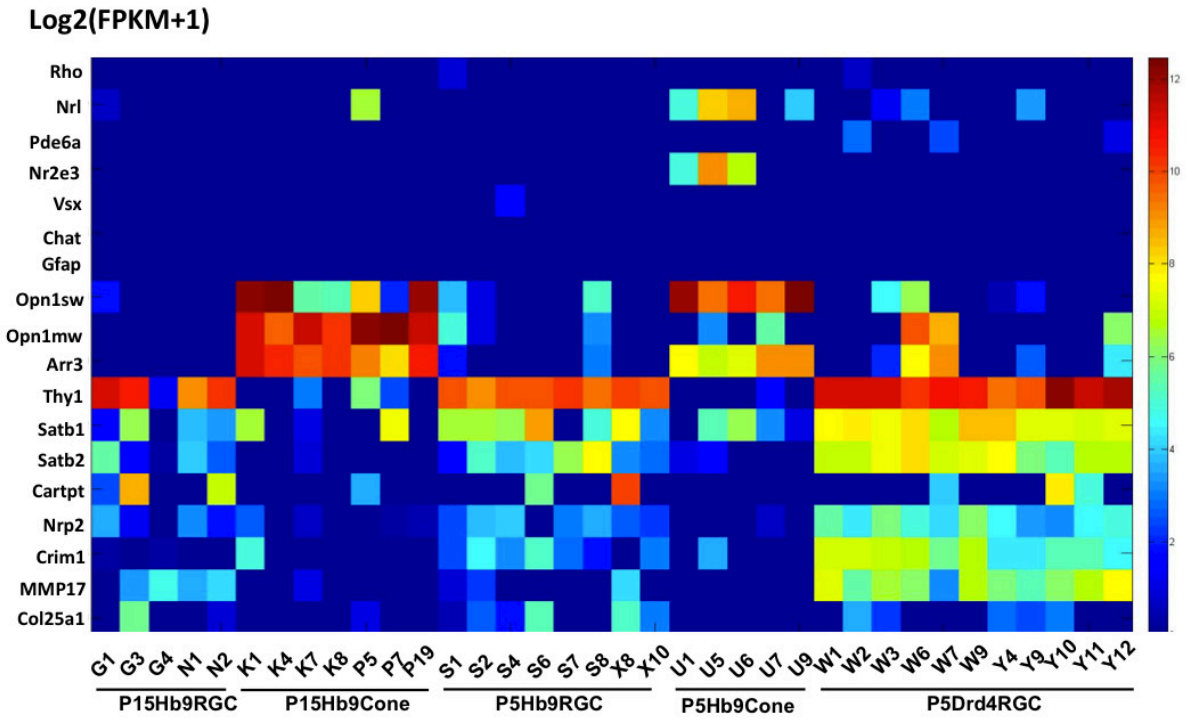

Figure 6.8 Heat map of the expression level of previously reported maker genes.

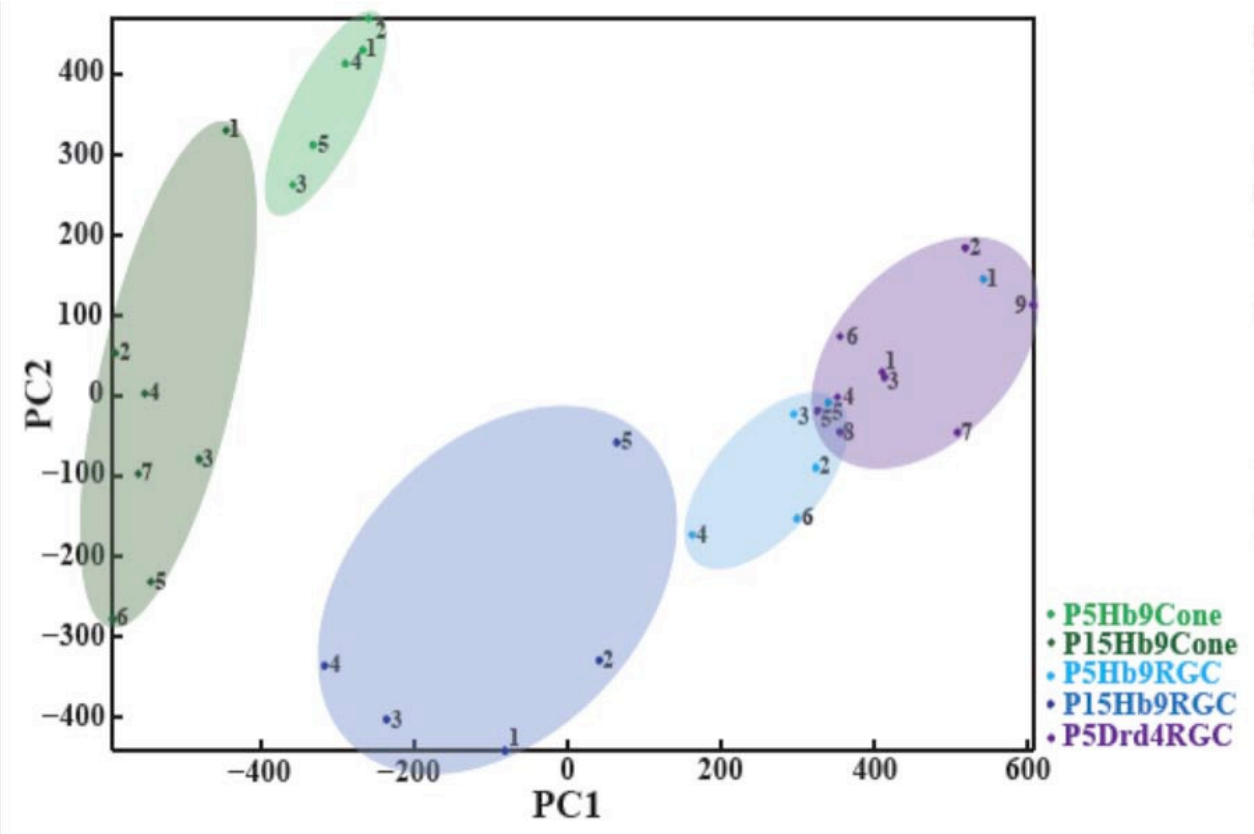

Figure 6.9 Principle component analysis of Hb9 cone photoreceptors and Hb9/Drd4 RGCs.

Hierarchical clustering result across all genes detected is shown in Figure 6.10. A complete linkage method with Euclidean distance calculation was used for this hierarchical clustering. The distance between two clusters is defined by the maximum distance between their individual components. Two nearest clusters were merged into a new one at each stage of the clustering process and this is repeated until the entire data set was agglomerated into a single cluster at the end. As we seen in Figure 6.10, photoreceptors and RGCs belong to two separate clusters with longest distance. One layer below that the age dependent clustering in photoreceptors and that subtype dependent clustering in RGCs was observed with a single outlier of Drd4 RGC mixed in the other subtype cluster.

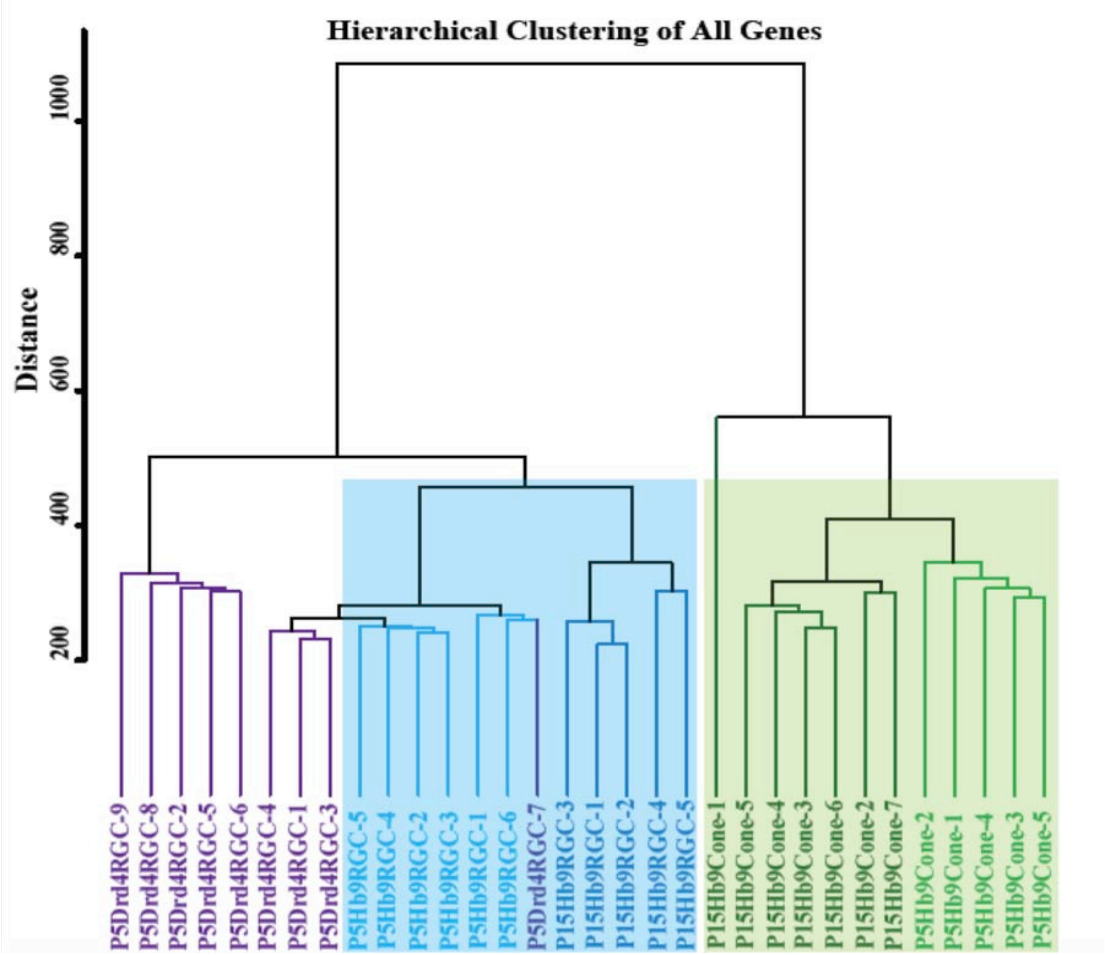

Figure 6.10 Hierarchical clustering result of Hb9 cone photoreceptors and Hb9/Drd4 RGCs.

The gene expression difference in photoreceptor cells and RGCs are further demonstrated in the heat map shown as Figure 6.11. The transcriptional regulator CRX was identified as a photoreceptor –specific retinopathy gene (Chen et al., 1997; Furukawa et al., 1997; Freund et al., 1997) and it was reported to be essential for terminal differentiation of rods and cones and enhance the expression of photoreceptor-specific genes (Mitton et al., 2000; Hennig et al., 2008). As seen in Figure 6.11, CRX is specifically expressed in photoreceptors not in RGCs, which is consistent with previous report.

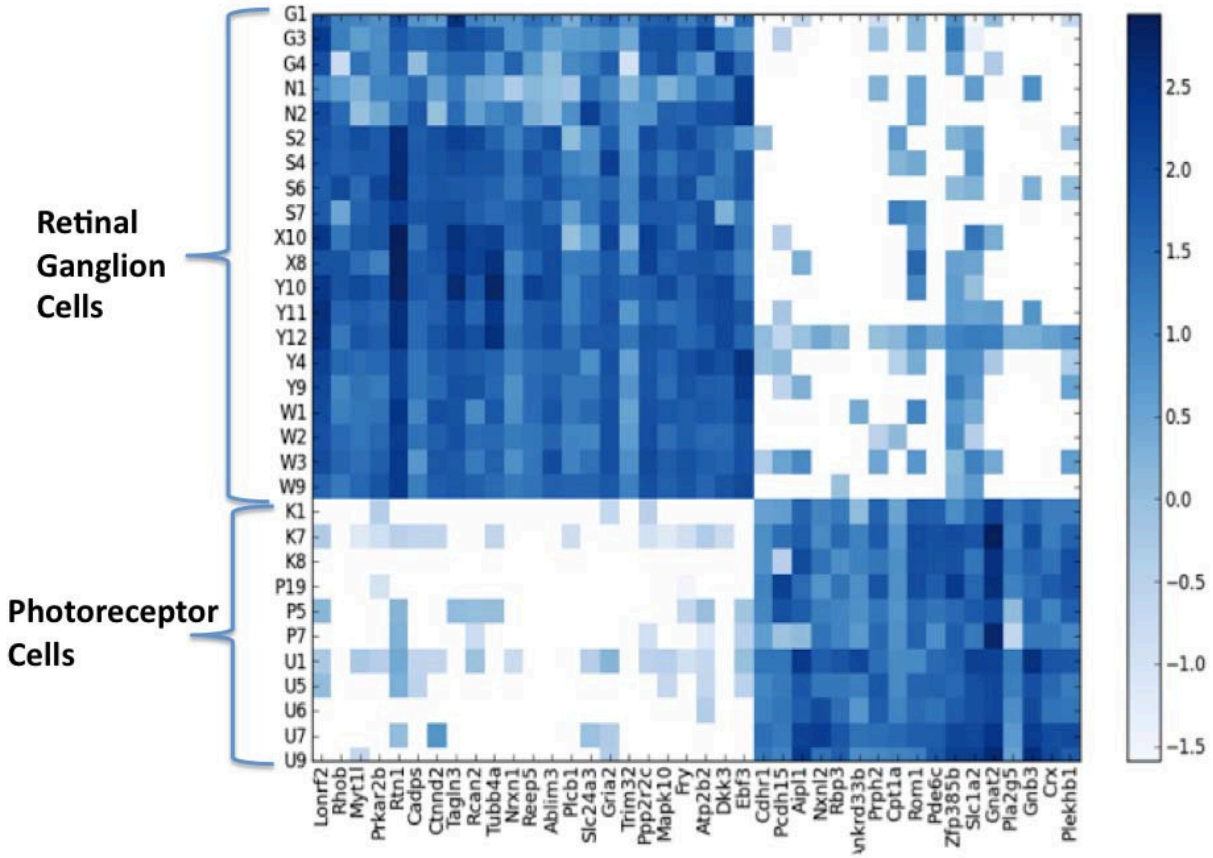

Figure 6.11 Heat map of differentially expressed genes in photoreceptors vs. retinal ganglion cells.

More differential gene analysis was conducted between Hb9 RGCs and Drd4 RGCs (Figure 6.12) Matrix metalloprotease 17 (Mm17), cell surface-associated enzyme (Sohail et al., 2008), was reported to be specifically expressed in Drd4 RGCs (Kay et al., 2011). This is further confirmed by our result demonstrated in Figure 6.12 where Mm17 is highly expressed in Drd4 RGCs but very lowly expressed in Hb9 RGCs. Cdh11 and several other genes also exhibit similar pattern and further in situ validation is needed. On the other hand, the expression levels of genes such as Rab15 and Scn2b are higher in Hb9 RGCs than in Drd4 RGCs. Whether these genes can be used as the Hb9 RGC markers needs further investigation.

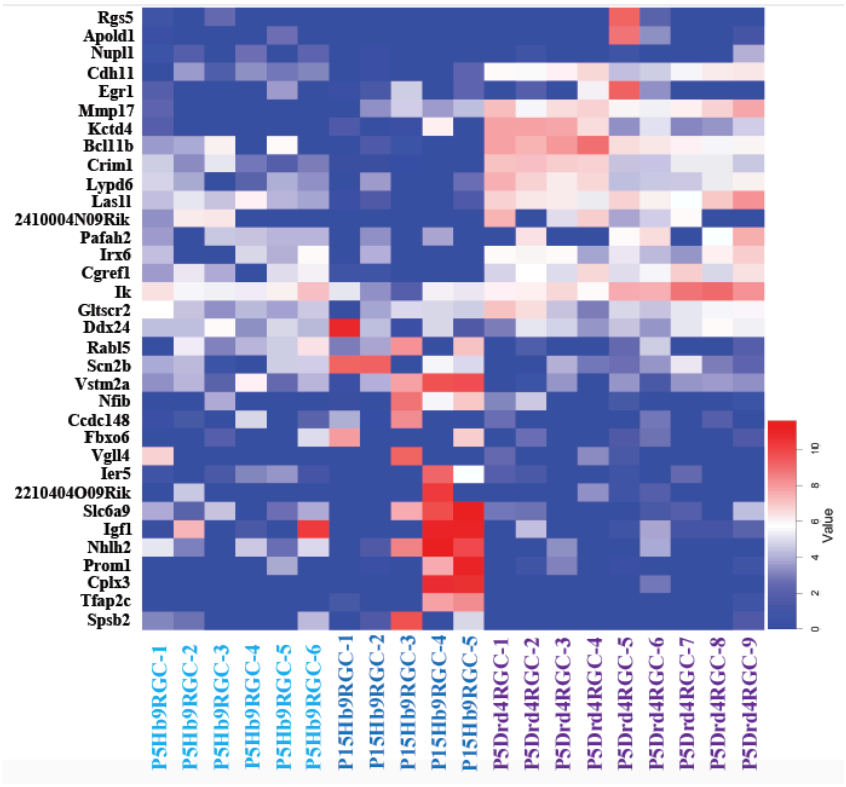

Figure 6.12 Heat map of differentially expressed genes in Hb9 RGCs vs. Drd4 RGCs.

6.4 Conclusion

In this chapter, we demonstrated that single cell transcriptome analysis using MALBAC-RNA-Seq method could well distinguish photoreceptors and retinal ganglion cells in the principle component analysis and hierarchical clustering analysis. The identified differentially expressed genes are consistent with previous validated reports and there are also newly reported genes which could potentially contribute to the future study on the function and age development of photoreceptor and retinal ganglion cells. Furthermore, the closely related retina ganglion cell subtypes Hb9 (responsive to ventral movement) and Drd4 (responsive to nasal movement) can also be distinguished using this approach. Single cell genetic profiles of these two RGC subtypes are uncovered for the first time and this information will be valuable for the future study of motion direction selective circuits.

References

Arber, S., Han, B., Mendelsohn, M., Smith, M., Jessell, T.M., and Sockanathan, S. (1999). Requirement for the homeobox gene Hb9 in the consolidation of motor neuron identity. Neuron 23, 659-674.

Barlow, H.B., and Levick, W.R. (1965). The mechanism of directionally selective units in rabbit's retina. The Journal of physiology 178, 477-504.

Bengtsson, M., Stahlberg, A., Rorsman, P., and Kubista, M. (2005). Gene expression profiling in single cells from the pancreatic islets of Langerhans reveals lognormal distribution of mRNA levels. Genome research 15, 1388-1392.

Brown, P.O., and Botstein, D. (1999). Exploring the new world of the genome with DNA microarrays. Nature genetics 21, 33-37.

Chen, S., Wang, Q.L., Nie, Z., Sun, H., Lennon, G., Copeland, N.G., Gilbert, D.J., Jenkins, N.A., Zack, D.J.(1997). Crx, a novel Otx-like paired homeodomain protein, binds to and transactivates photoreceptor cell-specific genes. Neuron 19, 1017–1030.

Dacey, D.M. (2004). The Cognitive Neurosciences (ed.Gazzaniga, M.S.) MIT Press, Cambridge, 281-301.

Dean, F.B., Nelson, J.R., Giesler, T.L., and Lasken, R.S. (2001). Rapid amplification of plasmid and phage DNA using Phi 29 DNA polymerase and multiply-primed rolling circle amplification. Genome research 11, 1095-1099.

DeRisi, J.L., Iyer, V.R., and Brown, P.O. (1997). Exploring the metabolic and genetic control of gene expression on a genomic scale. Science 278, 680-686.

Diehn, M., Cho, R.W., Lobo, N.A., Kalisky, T., Dorie, M.J., Kulp, A.N., Qian, D., Lam, J.S., Ailles, L.E., Wong, M., et al. (2009). Association of reactive oxygen species levels and radioresistance in cancer stem cells. Nature 458, 780-783.

Freund, C. L., Gregory-Evans, C.Y., Furukawa, T., Papaioannou, M., Looser, J., Ploder, L., Bellingham, J., Ng, D., Herbrick, Ja.A., Duncan, A., Scherer, S.W., Tsui, L.C., Loutradis-Anagnostou, A., Jocobson, S.G., Cepko, C.L., Bhattacharya, S.S., Mcklnnes, R.R. (1997). Cone-rod dystrophy due to mutations in a novel photoreceptor-specific homeobox gene (CRX) essential for maintenance of the photoreceptor. Cell 91, 543–553.

Furukawa, T., Morrow, E. M. & Cepko, C. L. (1997). Crx, a novel otx-like homeobox gene, shows photoreceptor-specific expression and regulates photoreceptor differentiation. Cell 91, 531–541.

Gong, S., Zheng, C., Doughty, M.L., Losos, K., Didkovsky, N., Schambra, U.B., Nowak, N.J., Joyner, A., Leblanc, G., Hatten, M.E., et al. (2003). A gene expression atlas of the central nervous system based on bacterial artificial chromosomes. Nature 425, 917-925.

Guo, G., Huss, M., Tong, G.Q., Wang, C., Li Sun, L., Clarke, N.D., and Robson, P. (2010). Resolution of cell fate decisions revealed by single-cell gene expression analysis from zygote to blastocyst. Developmental cell 18, 675-685.

Hashimshony, T., Wagner, F., Sher, N., and Yanai, I. (2012). CEL-Seq: single-cell RNA-Seq by multiplexed linear amplification. Cell reports 2, 666-673.

Hennig, A. K., Peng, G. H. & Chen, S. (2008). Regulation of photoreceptor gene expression by Crx-associated transcription factor network. Brain Res. 1192, 114–133.

Huberman, A.D., Wei, W., Elstrott, J., Stafford, B.K., Feller, M.B., and Barres, B.A. (2009). Genetic identification of an On-Off direction-selective retinal ganglion cell subtype reveals a layer-specific subcortical map of posterior motion. Neuron 62, 327-334.

Islam, S., Kjallquist, U., Moliner, A., Zajac, P., Fan, J.B., Lonnerberg, P., and Linnarsson, S. (2011). Characterization of the single-cell transcriptional landscape by highly multiplex RNA-seq. Genome research 21, 1160-1167.

Islam, S., Kjallquist, U., Moliner, A., Zajac, P., Fan, J.B., Lonnerberg, P., and Linnarsson, S. (2012). Highly multiplexed and strand-specific single-cell RNA 5' end sequencing. Nature protocols 7, 813-828.

Kay, J.N., De la Huerta, I., Kim, I.J., Zhang, Y.F., Yamagata, M., Chu, M.W., Meister, M., and Sanes, J.R. (2011). Retinal Ganglion Cells with Distinct Directional Preferences Differ in Molecular Identity, Structure, and Central Projections. J Neurosci 31, 7753-7762.

Kim, D., Pertea, G., Trapnell, C., Pimentel, H., Kelley, R., and Salzberg, S.L. (2013). TopHat2: accurate alignment of transcriptomes in the presence of insertions, deletions and gene fusions. Genome biology 14, R36.

Kurimoto, K., Yabuta, Y., Ohinata, Y., Ono, Y., Uno, K.D., Yamada, R.G., Ueda, H.R., and Saitou, M. (2006). An improved single-cell cDNA amplification method for efficient high-density oligonucleotide microarray analysis. Nucleic Acids Res 34.

Mitton, K. P., Swain, P.K., Chen, S., Xu, S., Zack, D.J., Swaroop, A. (2000) The leucine zipper of NRL interacts with the CRX homeodomain. A possible mechanism of transcriptional synergy in rhodopsin regulation.J. Biol. Chem. 275, 29794–29799.

Nassi, J.J., and Callaway, E.M. (2009). Parallel processing strategies of the primate visual system. Nature reviews Neuroscience 10, 360-372.

Picelli, S., Bjorklund, A.K., Faridani, O.R., Sagasser, S., Winberg, G., and Sandberg, R. (2013). Smart-seq2 for sensitive full-length transcriptome profiling in single cells. Nature methods 10, 1096-1098.

Raj, A., Peskin, C.S., Tranchina, D., Vargas, D.Y., and Tyagi, S. (2006). Stochastic mRNA synthesis in mammalian cells. Plos Biol 4, e309.

Ramskold, D., Luo, S., Wang, Y.C., Li, R., Deng, Q., Faridani, O.R., Daniels, G.A., Khrebtukova, I., Loring, J.F., Laurent, L.C., et al. (2012). Full-length mRNA-Seq from single-cell levels of RNA and individual circulating tumor cells. Nature biotechnology 30, 777-782.

Rodieck, R.W.(1998). The First Steps in Seeing. Sinauer Associates.

Saiki, R.K., Gelfand, D.H., Stoffel, S., Sharf, S.J., Higuchi, R., Horn, G.T., Mullis, K.B., and Erlich, H.A. (1988). Primer-directed enzymatic amplification of DNA with a thermostable DNA polymerase. Science 239, 487-491.

Sanchez-Freire, V., Ebert, A.D., Kalisky, T., Quake, S.R., and Wu, J.C. (2012). Microfluidic single-cell real-time PCR for comparative analysis of gene expression patterns. Nature protocols 7, 829-838.

Sanes, J.R., and Zipursky, S.L. (2010). Design principles of insect and vertebrate visual systems. Neuron 66, 15-36.

Shalek, A.K., Satija, R., Adiconis, X., Gertner, R.S., Gaublomme, J.T., Raychowdhury, R., Schwartz, S., Yosef, N., Malboeuf, C., Lu, D., et al. (2013). Single-cell transcriptomics reveals bimodality in expression and splicing in immune cells. Nature 498, 236-240.

Shiroguchi, K., Jia, T.Z., Sims, P.A., and Xie, X.S. (2012). Digital RNA sequencing minimizes sequence-dependent bias and amplification noise with optimized single-molecule barcodes. Proc. Natl.Acad.Sci.U.S.A. 109, 1347-1352.

Sohail A, Sun Q, Zhao H, Bernardo MM, Cho JA, Fridman R. (2008). MT4-(MMP17) and MT6-MMP (MMP25), A unique set of membrane-anchored matrix metalloproteinases: properties and expression in cancer. Cancer Metastasis Rev., 27:289–302.

Swaroop, A., Kim, D., and Forrest, D. (2010). Transcriptional regulation of photoreceptor development and homeostasis in the mammalian retina. Nat Rev Neurosci 11, 563-576.

Tang, F., Barbacioru, C., Nordman, E., Li, B., Xu, N., Bashkirov, V.I., Lao, K., and Surani, M.A. (2010). RNA-Seq analysis to capture the transcriptome landscape of a single cell. Nature protocols 5, 516-535.

Tang, F., Barbacioru, C., Wang, Y., Nordman, E., Lee, C., Xu, N., Wang, X., Bodeau, J., Tuch, B.B., Siddiqui, A., et al. (2009). mRNA-Seq whole-transcriptome analysis of a single cell. Nature methods 6, 377-382.

Taniguchi, K., Kajiyama, T., and Kambara, H. (2009). Quantitative analysis of gene expression in a single cell by qPCR. Nat Methods 6, 503-U550.

Taniguchi, Y., Choi, P.J., Li, G.W., Chen, H., Babu, M., Hearn, J., Emili, A., and Xie, X.S. (2010). Quantifying E. coli proteome and transcriptome with single-molecule sensitivity in single cells. Science 329, 533-538.

Topalidou, I., van Oudenaarden, A., and Chalfie, M. (2011). Caenorhabditis elegans aristaless/Arx gene alr-1 restricts variable gene expression. Proceedings of the National Academy of Sciences of the United States of America 108, 4063-4068.

Trapnell, C., Hendrickson, D.G., Sauvageau, M., Goff, L., Rinn, J.L., and Pachter, L. (2013). Differential analysis of gene regulation at transcript resolution with RNA-seq. Nat Biotechnol 31, 46-+.

Warren, L.A., Rossi, D.J., Schiebinger, G.R., Weissman, I.L., Kim, S.K., and Quake, S.R. (2007). Transcriptional instability is not a universal attribute of aging. Aging cell 6, 775-782.

Wassle, H. (2004). Parallel processing in the mammalian retina. Nature reviews Neuroscience 5, 747-757.

Wei, W., and Feller, M.B. (2011). Organization and development of direction-selective circuits in the retina. Trends in neurosciences 34, 638-645.

Xue, Z., Huang, K., Cai, C., Cai, L., Jiang, C.Y., Feng, Y., Liu, Z., Zeng, Q., Cheng, L., Sun, Y.E., et al. (2013). Genetic programs in human and mouse early embryos revealed by single-cell RNA sequencing. Nature 500, 593-597.

Zong, C., Lu, S., Chapman, A.R., and Xie, X.S. (2012). Genome-wide detection of single-nucleotide and copy-number variations of a single human cell. Science 338, 1622-1626.

Chapter 7

Decoding the Molecular Divergence in the ON-OFF Retinal Circuit

Motion detection is an important functional feature of visual processing. Wiring mechanism of ON-OFF direction-selective retina ganglion cells (ooDSGCs) and inhibitory starburst amacrine cells (SACs) is crucial for the understanding of direction-selective response of retina to motion stimuli. There are two subtypes of SACs responding distinctively to the onset (ON subtype) and cessation (OFF subtype) of the visual stimulus, which also correlates with their connectivity with the bistratified ooDSCGs and their cell body localizations. Understanding the development of the regulatory network by ON-OFF SACs is crucial for uncovering the direction selection network but little is known about the molecular difference between these two subtypes due to the limitation in current available technologies. Here we perform single cell transcriptome analysis of SACs using MALBAC-RNA-seq approach to uncover the difference in the genetic profiles of ON versus OFF SACs. We classify two distinctive groups of SACs using principal component analysis and k-mean clustering method. We report the significant differential genes between these two clusters and validate in situ the ON-layer specific expression of Sox9 and OFF-layer specific expression of Calretinin using immunostaining method. The decreasing expression gap in Sox9 between ON and OFF subtypes with age is also observed in the transcriptome data analysis as well as in immunostaining results.

7.1 Background

In Chapter 6, the direction selectivity in retina in response to motion stimuli was mentioned and we will discuss more in detail in this chapter. It was first found fifty years ago that certain types of ganglion cells in rabbit retina responded selectively to a preferred motion direction (Barlow and Levick, 1965). There are two types of direction-selective ganglion cells in mammalian retina. One is an ON-OFF type responding to both dark and bright objects moving in a preferred direction at a broad range of speeds. Four subtypes exist with each one preferring one direction out of four cardinal axis (Barlow and Levick, 1965; Oyster, 1968). Another one is the ON type responding to slowly moving objects with 3 subtypes (Barlow and Levick, 1965; Oyster, 1968). Here we focus our discussion on the ON-OFF type ganglion cells, referred as ooDSGCs.

As shown in Figure 7.1, the dendrites of ooDSGCs extend to two sublaminae (termed as ON sublamina and OFF sublamina) within the plexiform layer of the retina (Amthor et al., 1984; Yang and Masland, 1994). They are in contact with and receive signal from two major interneuron cell types: glutamatergic biopolar cells and GABAergic starburst amacrine cells. The bipolar cells are further divided into two subtypes (ON/OFF subtype): the ON type bipolar cells depolarize with bright stimuli while the OFF type ones depolarize with dark stimuli. Each subtype connects to the corresponding layer of ooDSGC dendrites and transmits excitatory signals from photoreceptors (Famiglietti, 2002; Masland, 2001; Wassle, 2004). The bipolar cells also connect to starburst amacrine cells and transmit excitatory signal to them and the starburst amacrine cells are also categorized into two subtypes depending on their functions which correlates with

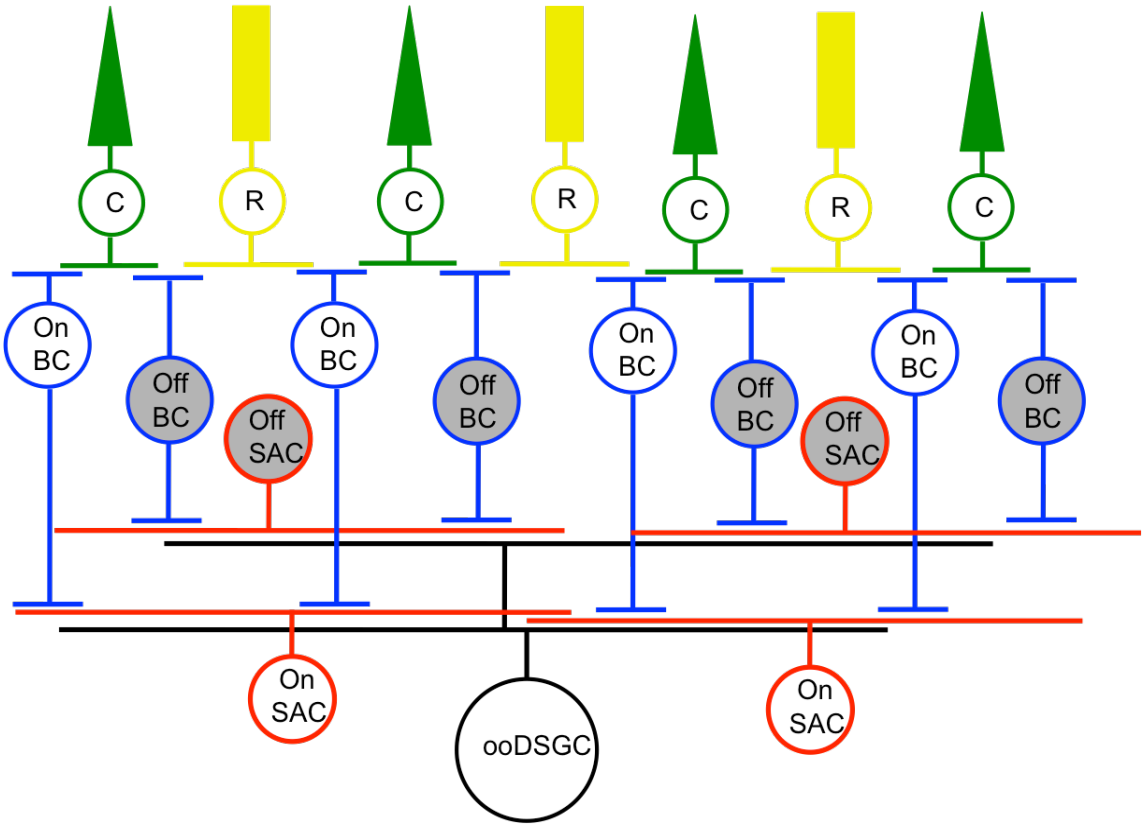

Figure 7.1 Wiring diagram of direction selection circuit. R: rod photoreceptor cell; C: cone photoreceptor cell; BC: bipolar cell; SAC: starburst amacrine cell; ooDSGC: On-off direction selecltive ganglion cell.

their localization of cell bodies and dendritic connectivity with bipolar cells and ooDSGCs (Chalupa and Gunhan, 2004). The ON type starburst amacrine cells receives excitatory signal from ON type bipolar cells and then transmits inhibitory signal to the dendrites of ooDSGCs in the ON sublamina. Similar relationship holds for OFF type starburst amacrine cells with OFF type bipolar cells and OFF sublamina of ooDSGC dendrites (Bloomfield, 1992, 1996; Huberman et al., 2009; Kay et al., 2011; Peters and Masland, 1996; Stacy and Wong, 2003; Taylor and Wassle, 1995). It has been found that bipolar cells differentiate after the beginning of ooDSGC stratification, suggesting that starburst amacrine cells (SAC) might have the function of mediating the early stratification of ooDSGC due to the earlier development before bipolar cells (Chalupa and Gunhan, 2004; Wong, 2003). Moreover, it was found that antagonizing Ach

synapses does not block direction selectivity (Ariel and Daw, 1982; Chiao and Masland, 2002; He and Masland, 1997; Kittila and Massey, 1997; Masland and Ames, 1976), while antagonizing $GABA_A$ does (Ariel and Daw, 1982; Caldwell et al., 1978; He and Masland, 1997; Kittila and Massey, 1995). This indicates that the inhibition plays a key role in the direction selectivity function (Ariel and Daw, 1982; Briggman et al., 2011; Caldwell et al., 1978; Euler et al., 2002; He and Masland, 1997; Kittila and Massey, 1995; Wei et al., 2011; Yonehara et al., 2011). Therefore, starburst amacrine cell as the major inhibitory interneuron plays the key role in the direction selectivity function. This hypothesis was further confirmed by two experimental studies observing the loss of direction selectivity function upon ablating starburst amacrine cells using toxins (Amthor et al., 2002; Yoshida et al., 2001).

Although it was indicated in some studies that visual experience is essential to the morphological and physiological maturation of retina (Fosser et al., 2005; Guenther et al., 2004; Lee et al., 2006; Lee et al., 2005; Lee et al., 2007; Lee et al., 2008; Tian and Copenhagen, 2001, 2003; Zhang et al., 2005). The independence of visual experience on the establishment of direction selectivity in the retina was reported (Elstrott et al., 2008) and some signaling pathway in the mouse retina such as P2X2-purinoceptor is considered to be programmed intrinsically (Kaneda et al., 2010).

The molecular mechanisms for the development of ON versus OFF starburst amacrine cells is not well understood. P2X2-purinoceptor was found to develop selectively in the OFF pathway(Kaneda et al., 2004), but it happens only after postnatal week 5-6 (Kaneda et al., 2010). At early developmental stage, P2X2-purinoceptor was developed in both ON and OFF pathways.

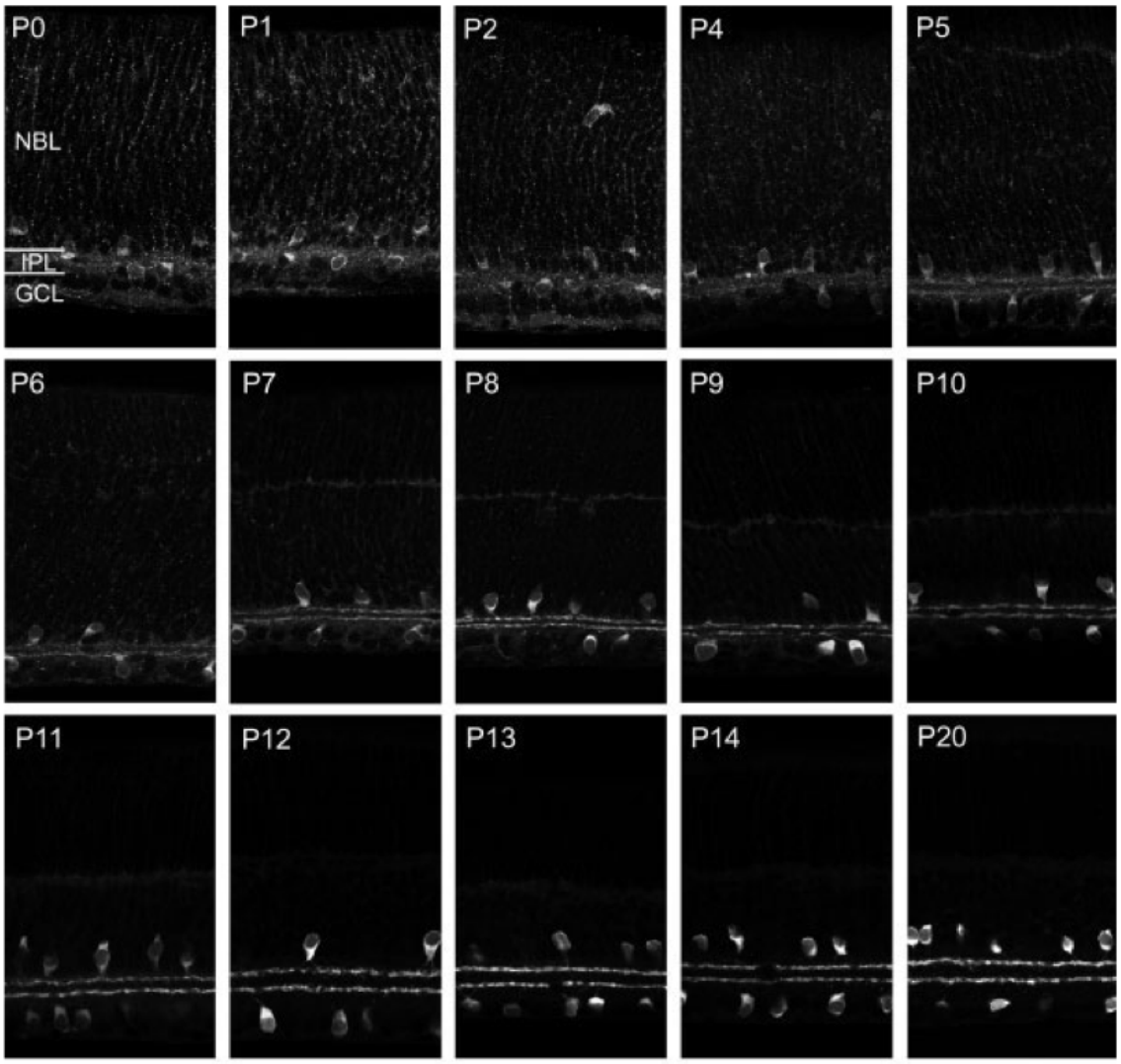

Figure 7.2 Early development of on-off layer of starburst amacrine cells (SAC) (Zhang et al., 2005).

It was observed that the ON-OFF layer formation of starburst amacrine cells happens at postnatal day 5 (as shown in Figure 7.2), the transcriptional events at this time point is a great interest for our study. Therefore P2X2 cannot be used as a marker for ON versus OFF layer for our further study on the early development of SAC circuit. It was later reported that the transmembrane protein semaphoring 6A is only expressed in the ON layer of SAC from postnatal day 9 (Sun et al., 2013). However repeated experiments showed that it was expressed in both layers without significant difference.

Therefore currently there is no reliable biomarker to differentiate ON versus OFF layer of starburst amacrine cells, making it impossible to enrich each subpopulation for further study. The approach of using laser capture microdissection incurs cell damage due to the frozen sectioning process and optical damage from the laser (Espina et al., 2006). Fluorescence *in situ* sequencing (FISSEQ) of RNA (Lee et al., 2015) was recently developed, which enables the gene profiling in specified location in tissue. However the current detectability is limited to 200-400 mRNA molecules. ON and OFF starburst amacrine cells are considered to be very close to each other in terms of the genetic profiles potentially with only a small fraction of genes differentially expressed between the two subtypes, therefore larger coverage over the transcriptome is desired.

With similar approach described in Chapter 6, we use Fluorescence-activated Cell Sorting (FACS) technique to isolate single starburst amacrine cells and then utilize the MALBAC-RNA-Seq method to amplify the mRNA for sequencing. Clustering analysis is performed based on the transcriptome data of each cell, followed by differential gene analysis to identify potential candidate marker genes. We use immunostaining method to validate the differentially expressed genes *in situ*.

7.2 Methods and Materials

ChAT-Cre mouse line (crossed with YFP reporter line) (Rossi et al., 2011) was sacrificed at postnatal day 6 (P6) and day 14 (P14). The retina was dissociated with papain and single cells were isolated using Fluorescence-activated Cell Sorting (FACS) based on GFP and antibody of Vc1.1 conjugated to vChAT (SAC marker). Figure 7.3a shows the immunostaining results of dissociated cell body (the first column) and *in situ* at the ON-OFF SAC laminae (the second column). GFP and ChAT/vChAT co-expression is confirmed in these immunostaining results. Figure 7.3b shows the gating panel in fluorescence-activated cell sorting (FACS). The cells were

isolated based on size (FSC channel), granularity (SSC channel), singularity (pulse width channel) GFP signal (FL1 channel) and ChAT/vChAT expression (FL4 channel). ChAT/vChAT expression is read out by conjugated antibody Vc1.1. The downstream workflow is very similar with what has been described in 6.2 with reverse transcription, MALBAC amplification, purification, quality control, library preparation and sequencing.

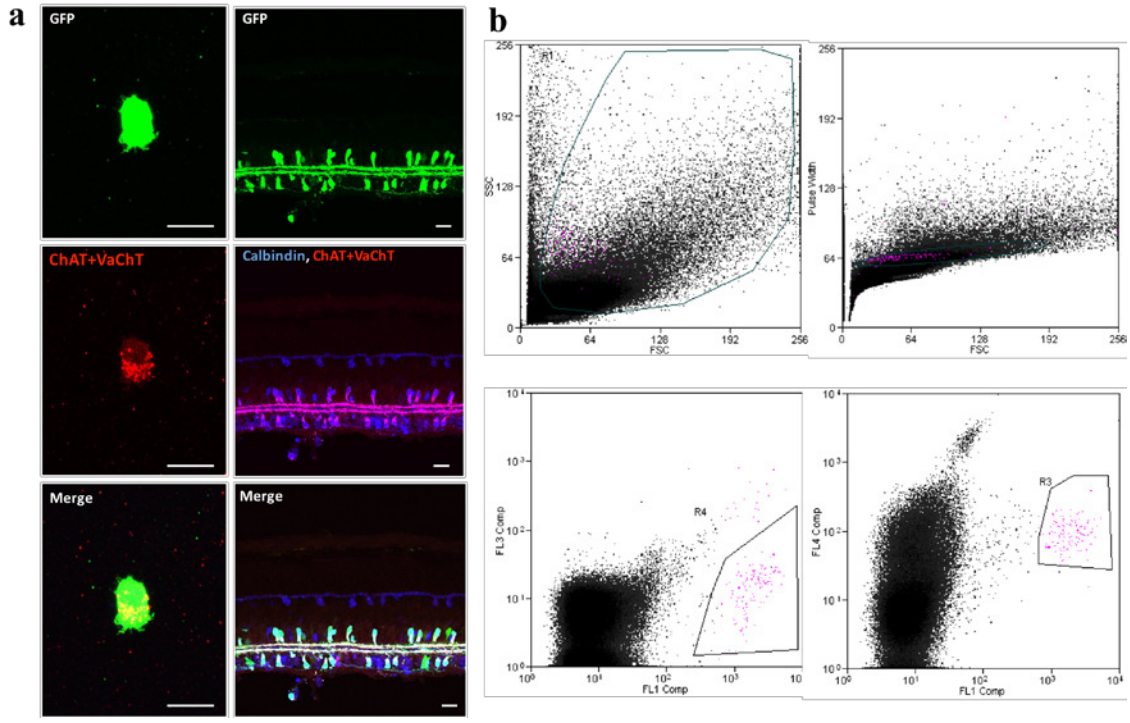

Figure 7.3 (a) Immunostaining results of dissociated SAC cells (left) and on-off SAC laminae in situ (right). Scale bar: 10 μm. (b) Gating panels on FACS, fluorescence-activated cell sorting. FSC: forward scattering channel; SSC: side scattering channel; FL1: GFP; FL4: Vc1.1. The upper left panel represents the size and granularity of all sorted events. Single cell events are gated in the upper right panel. GFP positive cells are gated in the lower left panel selects. The gate in the lower right panel selects out ChAT positive cells.

The number of genes detected per cell depends on the read number per cell. It first increases with higher mapped reads and saturates at 1~2 million mapped reads (Figure 7.4). We pooled 48 cells in each Hi-Seq lane of 200 million read capacity, around 170 million read was used efficiently and the mapping rate is around 70%. On average each cell can get ~2 million mapped reads,

which is enough for optimizing the number of the genes detected.

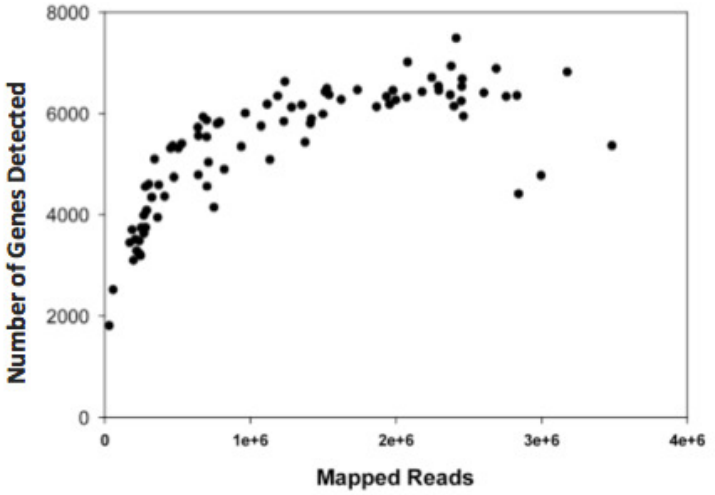

Figure 7.4 Number of genes detected depending on mapped reads. The samples include all the SACs, photoreceptors and RGCs (Chapter 6).

7.3 Results and Discussion

For our initial study, the transcriptome of 48 starburst amacrine cells were acquired and principle component analysis (PCA) was performed upon the whole transcriptome of these 48 cells (Figure 7.5). We observed clusters biased by the batch difference (samples collection conducted on different mice at different ages at postnatal day 5, 6, 7), which might come from the intrinsic genetic profile difference among different individual mouse or developmental difference among different ages. Since the transcriptome difference between ON versus OFF SACs was possibly overridden by the batch difference, more careful study was conducted upon minimizing the batch difference among all the sampled cells.

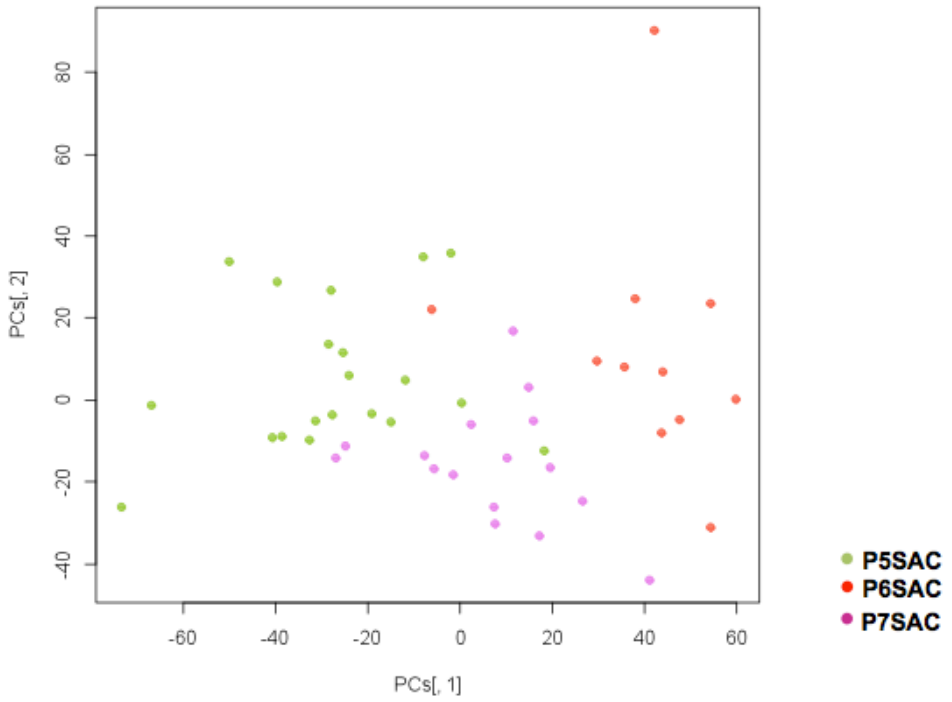

Figure 7.5 Principle component analysis (PCA) of the transcriptome data of 48 single P5, P6, P7 starburst amacrine cells (SAC)

We minimized the batch difference by collecting cells from a single eye of one male mouse at postnatal day 6 and did the same procedure for the sample collection at postnatal day 14. The cells from each batch were amplified simultaneously with same procedure and same reagent aliquots. The following purification and library preparation was also conducted in an unbiased way among samples. Minimal bias brought by batch difference or experimental procedures was guaranteed following these principles. Furthermore, the initial screening of qualified cells for further analysis was conducted by the hierarchical clustering of all sequenced samples for the SAC marker genes and control genes (Figure S7.1) and PCA/hierarchical clustering analysis on the whole transcriptome of the remaining samples (Figure S7.2). 44 P6-SACs and 39 P14-SACs remained for further analysis.

P6-SACs were analyzed separately from P14 SACs. The PCA of these 44 cells demonstrates two clusters in the 2D and 3D plot (Figure 7.6). The clustering marked in (b) was conducted using k-

means method. Although there are 5 outliers not included in any one of the two clusters, most of the cells can be classified in one cluster.

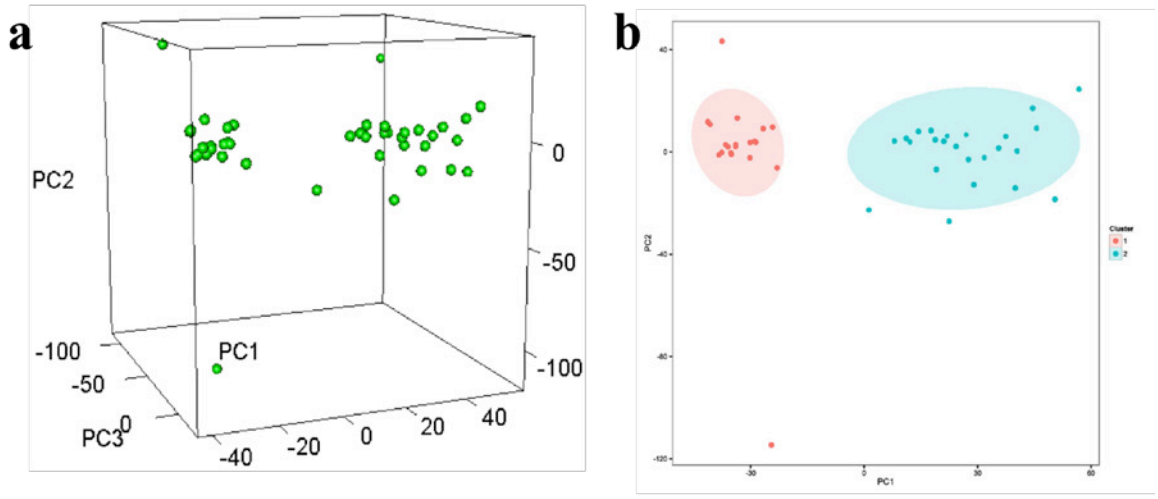

Figure 7.6 Principle component analysis (PCA) of P6- SACs (a) 3D (b) 2D.

Same analysis was conducted on P14-SACs (Figure 7.7). Two clusters are also observed in 2D and 3D plots but the two clusters are closer than those in P6-SACs, which might be due to the convergence of expression pattern at later development stage.

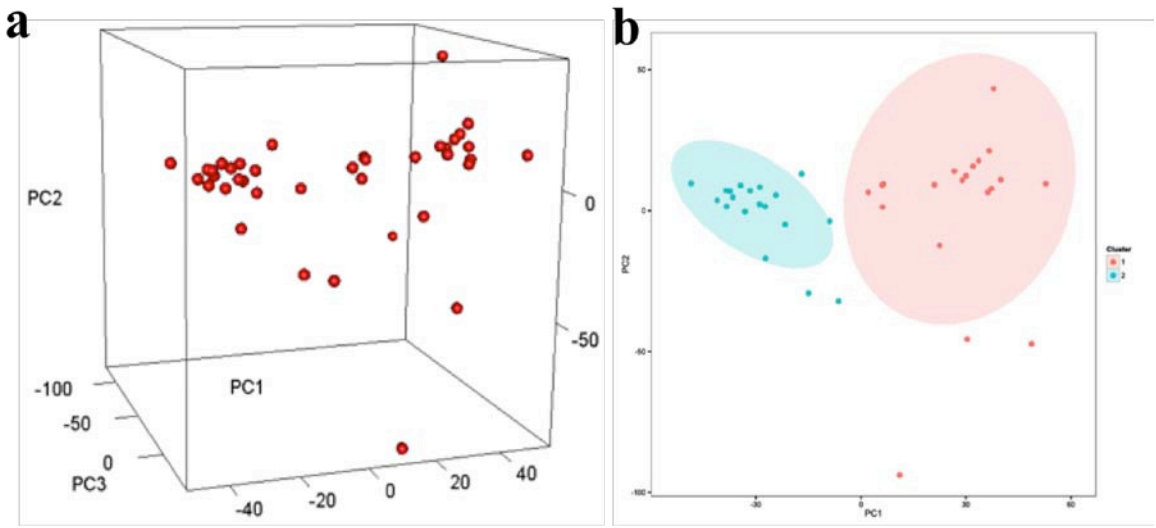

Figure 7.7 Principle component analysis (PCA) of P14-SACs (a) 3D (b) 2D.

After pulling all the SACs (P6 & P14) together, the clustering structure still maintains, indicating

that the difference between the two clusters is bigger than that between two ages (Figure 7.8).

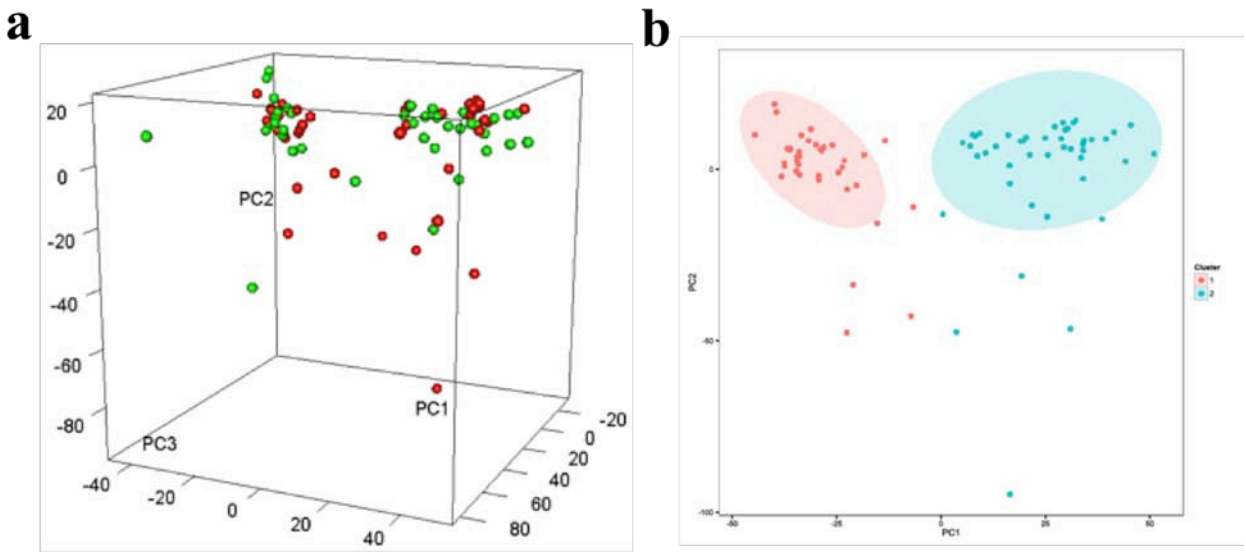

Figure 7.8 Principle component analysis (PCA) of all P6 and P14 SACs (a) 3D , P6 SACs in red, P14 SACs in green/blue (b) 2D.

Differential analysis on gene expressions were conducted for P6 SACs and P14 SACs separately using Cuffdiff. There are 761 genes in the significant differential gene list in P6-SACs and 339 genes in the significant differential gene list in P14-SACs (Figure 7.9). 189 of these genes are in the significant differential gene lists in both P6-SAC and P14-SAC.

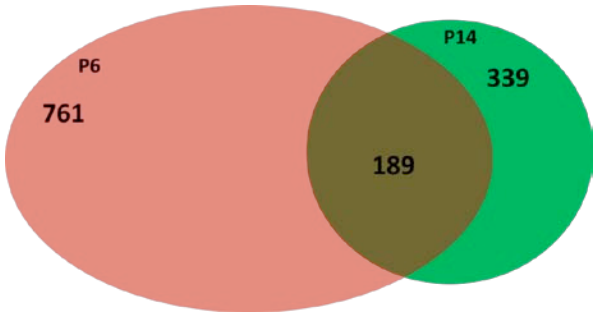

Figure 7.9 Significant differential genes in P6 and P14 SACs

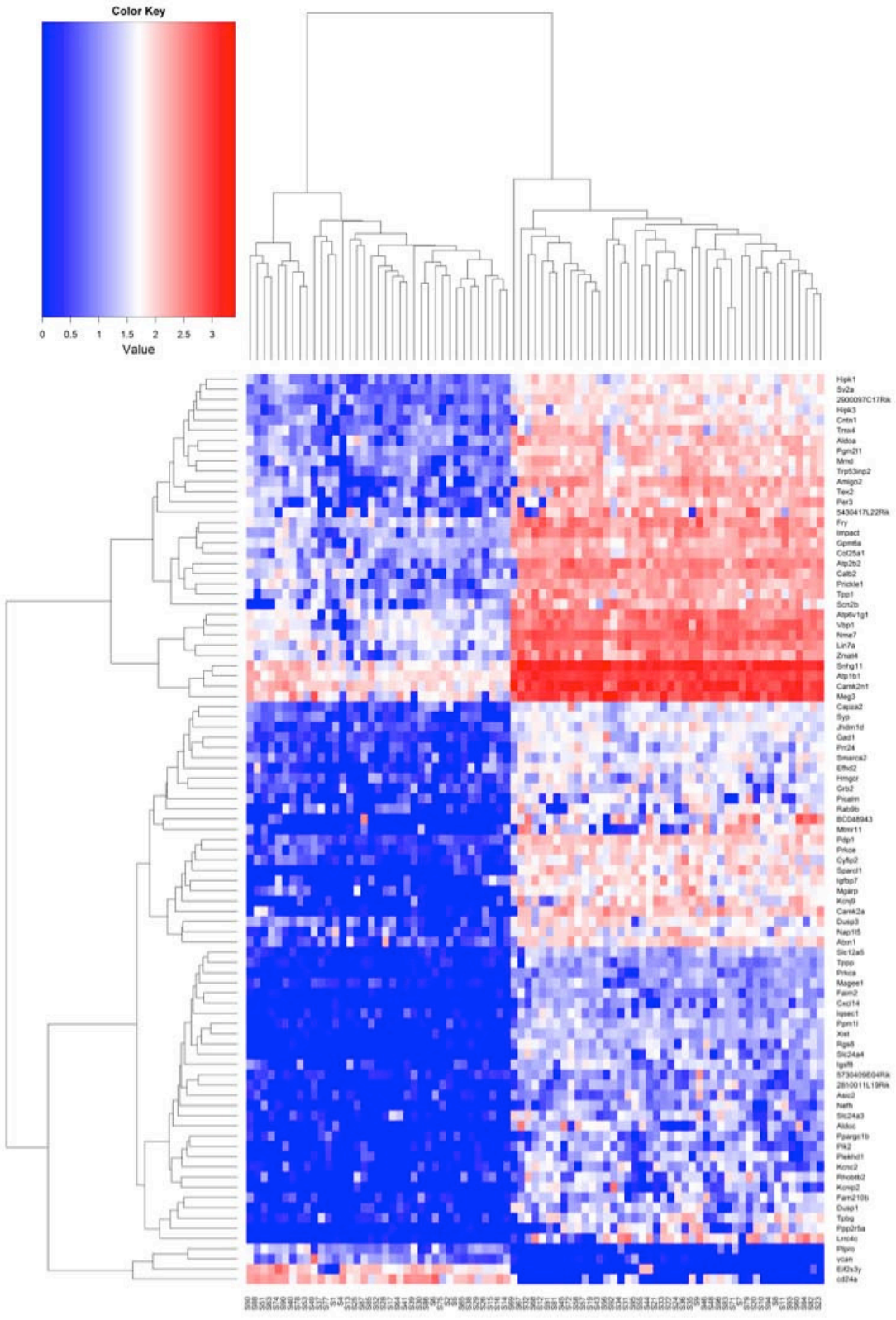

Figure 7.10 Heat map of expression levels in 100 top listed significant differential genes across all SACs

The heat map of the expression level in top 100 listed genes across SACs is shown in Figure 7.10 and the functional classification of these differential genes is listed in Table 7.1, where 9 transmembrane proteins are identified (these genes need close attention due to its relatedness with the cell-to-cell connectivity).

Table 7.1 Functional classification of top 100 listed significant differential genes.

Transmembrane protein	Lrrc4c, Faim2, Igsf8, synaptophysin, Amigo2, Tex2, Cntn1, Tmx4, Calb2
Matricellular protein	Sparcl1, vcan, Tpbg, Atxn1, Sv2a, Gpm6a, Smarca2, Col25a1
Zinc finger protein	Zmat4
Enzyme	Ppp2r5a, Prkca, Aldoc, Camk2a, Ppm1l, Ptpro, Dusp1, Plk2, Prkce, Pdp1, Gad1, Dusp3, Hmgcr, Atp2b2, Hipk3, Aldoa, Tpp1, Hipk1, Pgm2l1, Atp6v1g1, Nme7, Camk2n1, Atp1b1, Jhdm1d
Channel	Slc24a4, Kcnip2, Kcnj9, Slc12a5(KCC2), Kcnc2, Asic2, Slc24a3, Scn2b
Cytoskeleton genes	Nefh, Tppp, Efhd2, Capza2, Mtmr11
ligand, antigen	Cxcl14, Igfbp7, cd24a,
X-chromosome gene	Magee1 (ncRNA), Magee1, Xist
Y-chromosome gene	Eif2s3y (ncRNA)
Nuclear receptor	Prickle1, Trp53inp2
cytoplasmic gene	Rgs8, Rhobtb2, Rab9b, Grb2,
Unknown	Plekhd1, BC048943, 2810011L19Rik, Fam210b, Ppargc1b, Picalm, Prr24, 5730409E04Rik, Nap1l5, 2900097C17Rik, Mmd, Impact, 5430417L22Rik,

To test if the clustering result corresponds to the ON-OFF SAC sublamina difference as we hypothesized, the *in situ* validation on individual differential gene candidate is needed. Sox9 was in the significant gene list in P6-SAC group but not in P14-SAC group. The expression level in P6-SAC and P14-SAC in the two identified clusters is shown in Figure 7.11.

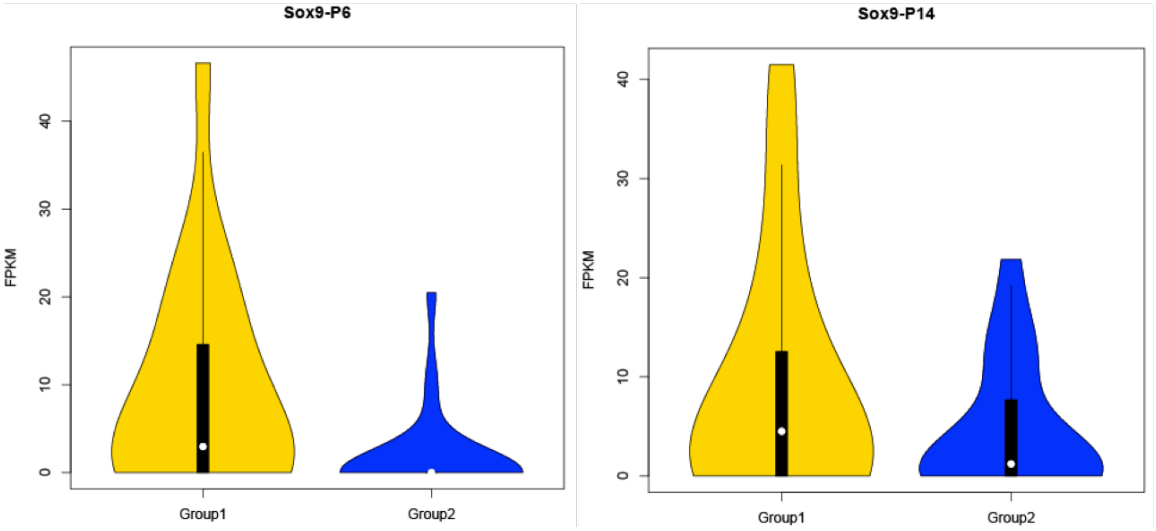

Figure 7.11 Violin plot of Sox9 expression level in two clusters at Postnatal day 6 (P6, left) and day 14 (P14, right).

Immunohistochemistry analysis was performed for the observation of co-localization of Sox9, GFP (labeling all SACs) and vChAT (vesicular acetylcholine transporter). ChAT is the enzyme responsible for synthesizing acetylcholine and acetylcholine is produced only by starburst amacrine cells, so the localization of vChAT indicates the location of SAC. In Figure 7.12, the expression of Sox9, which is highly expressed in one cluster of sequenced samples but lowly expressed in the other one, is shown in the red channel (c, c', c''). The distributions of GFP and vChAT are shown is in (a, a', a'') and (b, b', b''). Indicated by the arrows in (c), (d), (a')-(d'), Sox9 and GFP/vChAT exhibit selective overlap in the cell body staining only in the ON sublamina of inner plexiform layer. Therefore Sox9 can potentially be used as an ON-OFF sublamina marker gene for early development stage before eye opening.

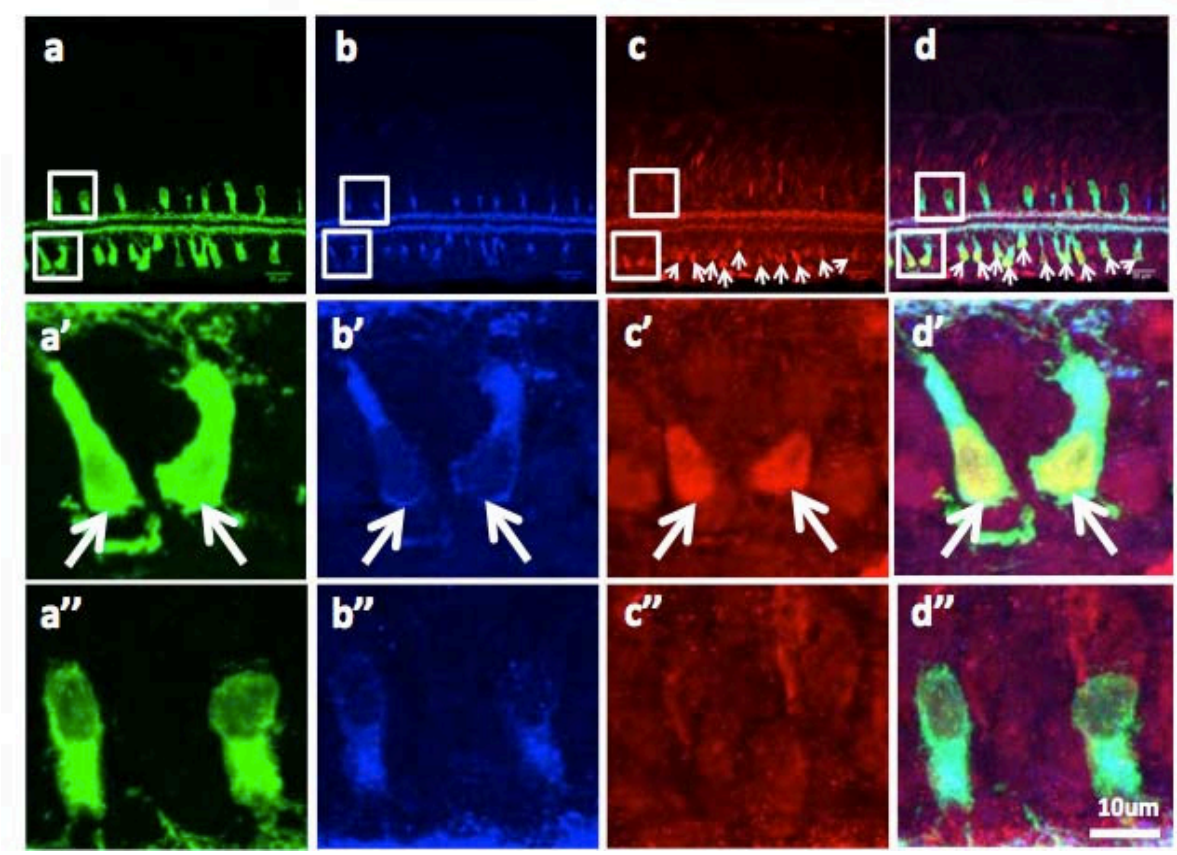

Figure 7.12 Immunostaining results of P6 ChATCre, STPY15. a. GFP; b. vChAT; c. Sox9; d. Merged image. a'-d': zoomed-in images of the cells at the on layer. a''-d'': zoomed-in images of the cells at the off layer. As seen here, Sox9 is only expressed in on layer.

More age points were investigated for Sox9. Figure 7.13 shows the co-localization of Sox 9 and GFP/vChAT across 4 age points (P1, P5, P10, P16). Similar observation can be still made in P1 before the ON-OFF sublamina is segregated and the SAC dendrites are intermingled and the co-localization of Sox9 with vChAT in cell bodies is mostly observed close to the ganglion cell layer (GCL) rather than the inner nuclear layer (INL).

For P10 and P16, same conclusion can be drawn that Sox9 is specifically expressed in the ON sublamina, however the expression difference between the two sublaminae decreases with age. Same trend is observed in the sequencing data, where P14 shows smaller difference in the expression level of Sox9 between two clusters compared to P6. As we see the expression level of

Sox9 converges between ON versus OFF sublamina as the mice get older in their development stage, we hypothesize that Sox 9 is crucial in determining the cell fate of SAC at early developmental stage.

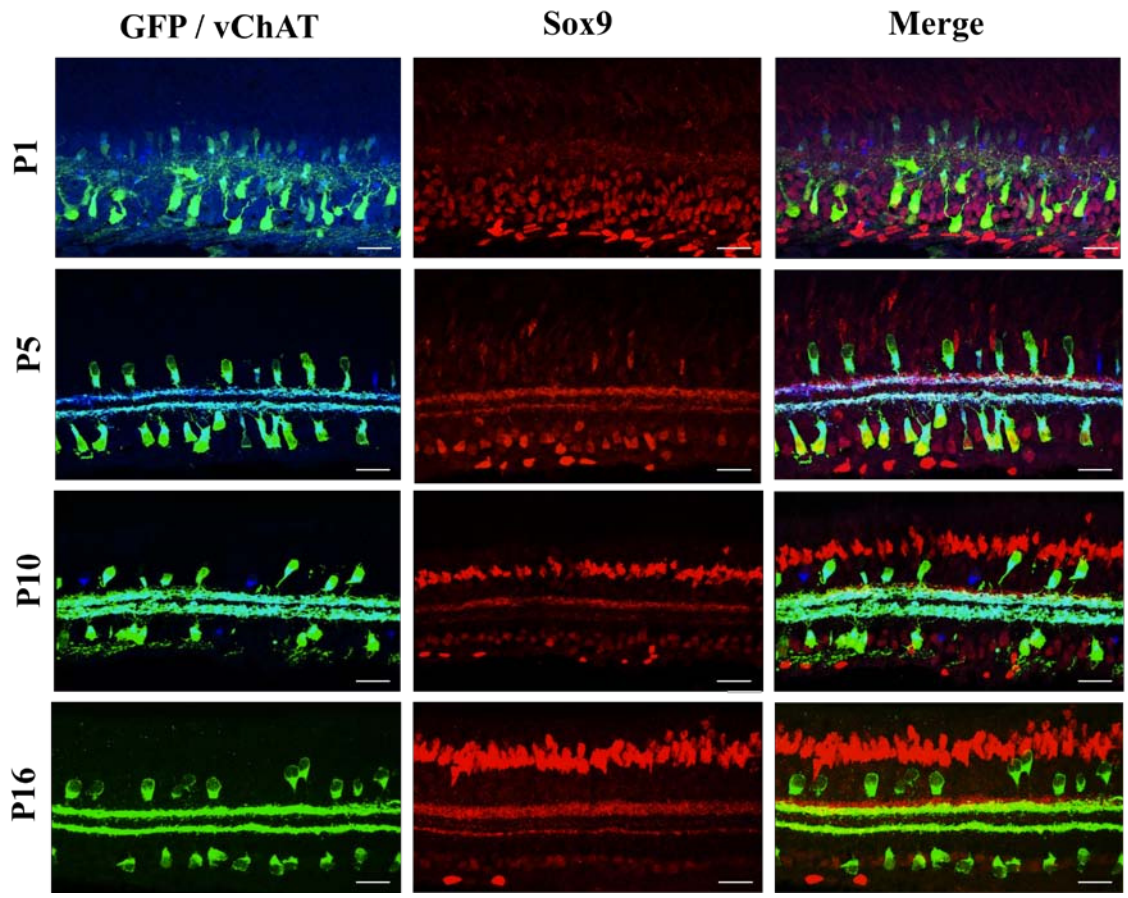

Figure 7.13 Immunostaining results across 4 age points (P1, P5, P10, P16). Scale bar: 20 μm.

This hypothesis can also be supported by the report that GABA is released by SAC to neighboring SACs during the first postnatal week (Zheng et al., 2004) and report on the ooDSGCs forming GABAergic synapses with SACs well before eye opening around postnatal day 12 (Lee et al., 2010; Wei et al., 2011).

Opposite observation can be made in Calretinin, which is highly expressed in the cluster 2 (where Sox9 shows low expression level) and demonstrates low expression level in cluster 1 (where Sox9 shows high expression level). The violin plot of the Calretinin expression in two

groups at P6 and P14 is shown in Figure 7.14.

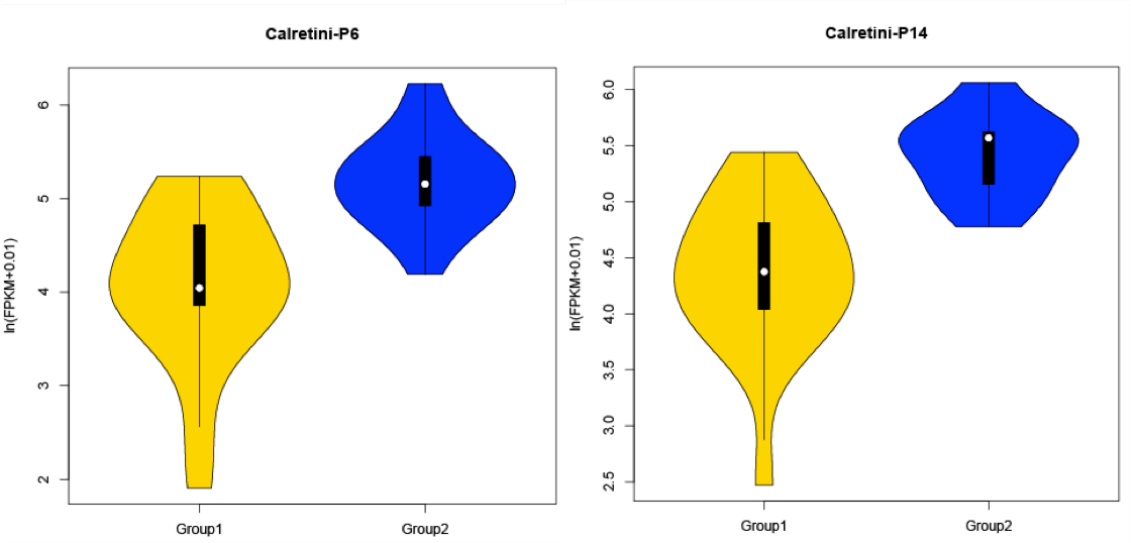

Figure 7.14 Violin plot of Calretinin expression level in two clusters at Postnatal day 6 (P6, left) and day 14 (P14, right)

This is further confirmed by the *in situ* validation using immunostaining method. Figure 7.15 shows the co-expression of GFP (a, a', a'') and Calretini (b, b', b'') at postnatal day 6 mouse retina. As seen here, Calretinin and GFP exhibit selective overlap in the cell body staining only in the OFF sublamina of inner plexiform layer, where Sox9 demonstrates low expression. This result is consistent with the sequencing data. Combining the opposite observation of Sox9 and Calretinin in both sequencing results and immunostaining results, the corresponding relationship of defined cluster 1 to ON-SAC and cluster 2 to OFF-SAC is justified.

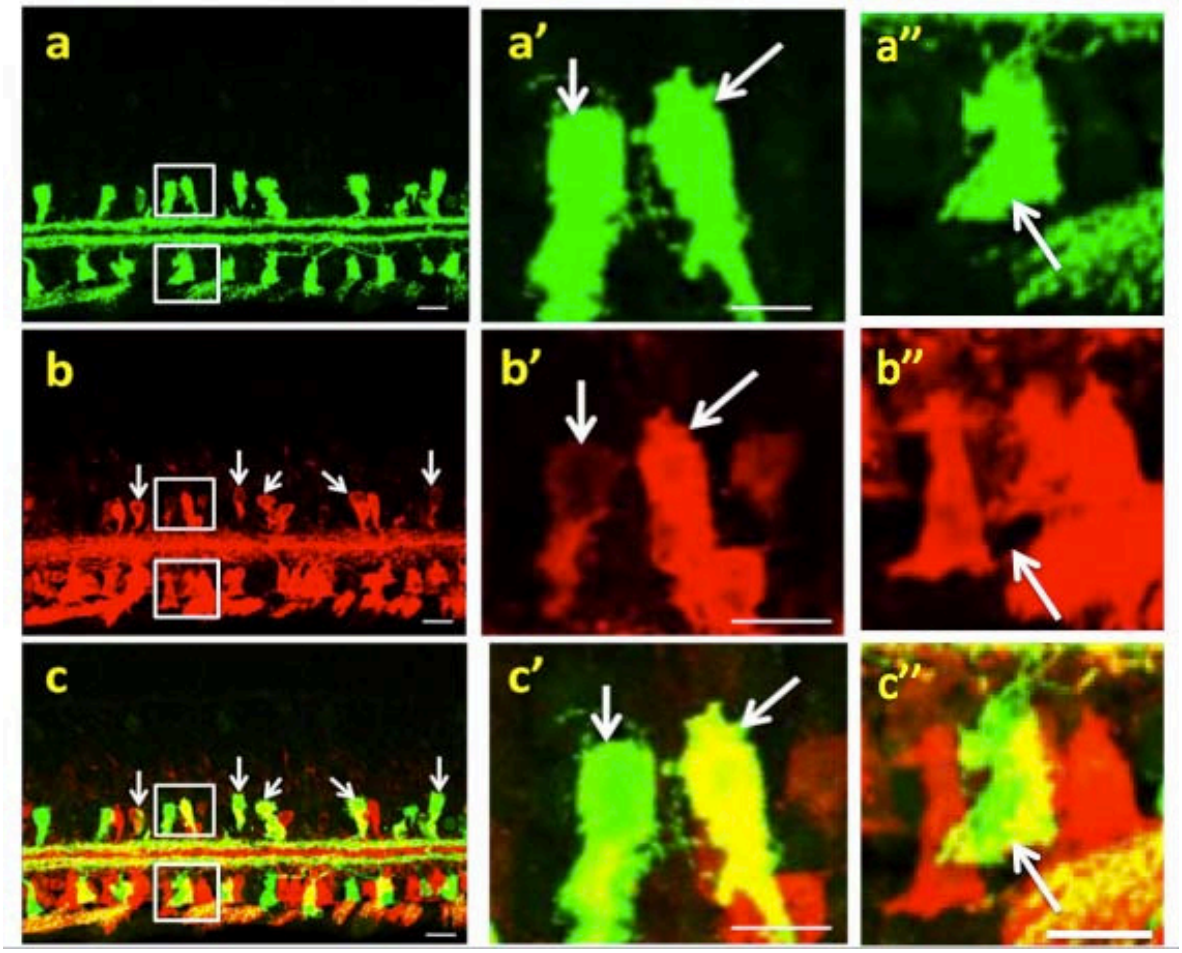

Figure 7.15 Immunostaining results of P6-ChATCre,STPY15. a. GFP; b. Calretinin; c. Merged image. a'-c': zoomed-in images of the cells at the off layer. a''-c'': zoomed-in images of the cells at the on layer. As seen here, Calretinin is only expressed in Off sublamina. Scale bar: 20 μm.

More validation is underway on the identified differentially expressed genes. Figure 7.16 shows several candidates demonstrating great potential. Vcan, Cd24a, Ptpro and Eif2s3y are potentially ON-SAC specific genes, whereas Lcc4c, Sparcl1, Kcnj9 and Calb2 are potentially OFF-SAC specific genes.

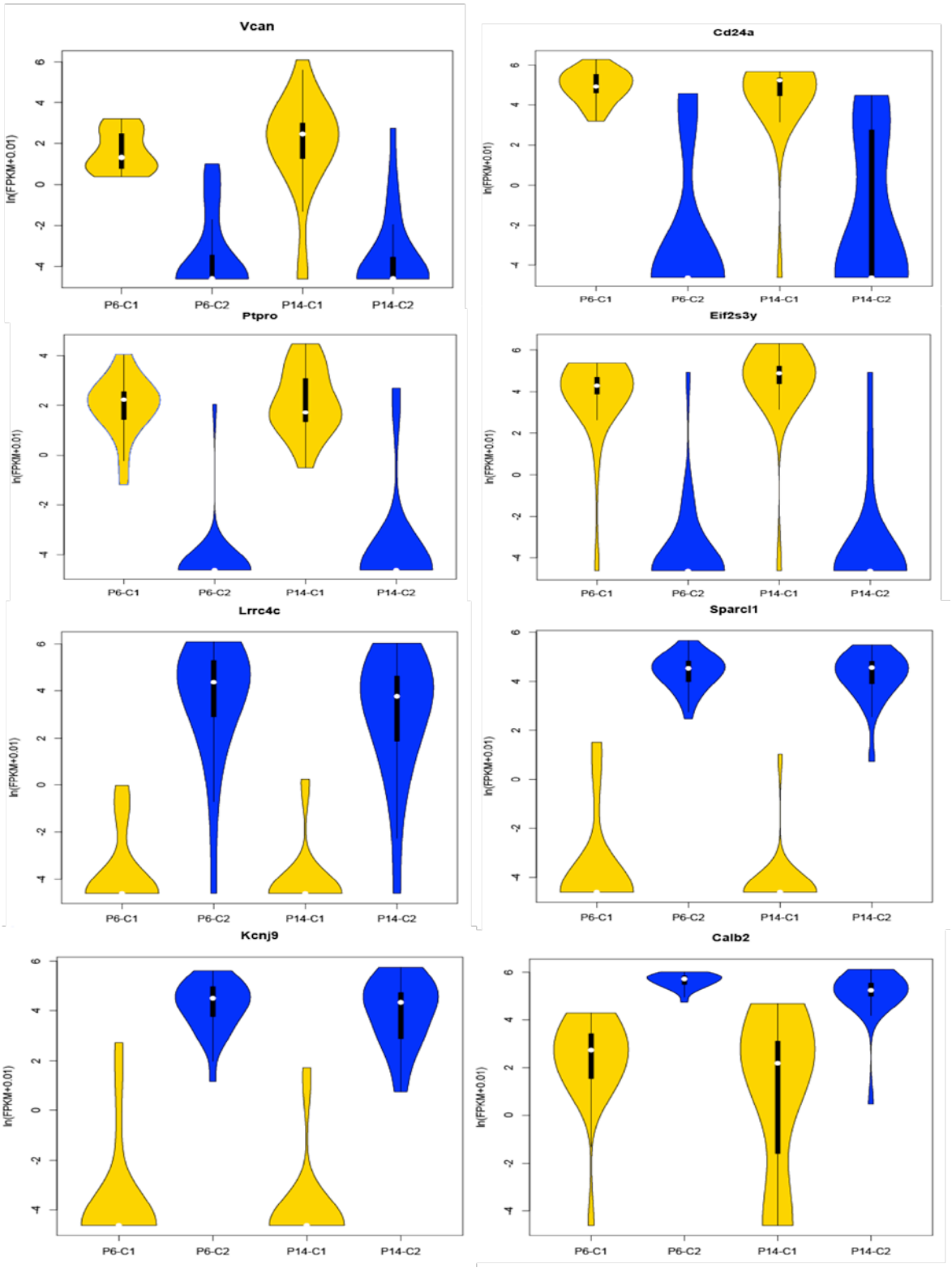

Figure 7.16 Violin plot of more differentially expressed genes

6.5 Conclusion

Starburst amacrine cells, the inhibitory inter-neurons essential for direction selectivity function, have been classified into two groups using single cell transcriptome analysis. 761 significant differential genes in P6-SACs and 339 significant differential genes in P14-SACs have been identified, 189 of which are in the significant differential gene lists in both P6-SAC and P14-SAC. One significant differential gene between these two clusters Sox9 has been validated *in situ* to be mainly expressed in the ON-SACs. Another identified differential gene Calretinin with expression pattern opposite to Sox9 has been validated *in situ* to be mainly expressed in the OFF-SACs. Moreover, the ON versus OFF difference in the Sox9 expression decreases with age based on the *in situ* immunostaining results at four different age points, which is consistent with the observation based on the sequencing results. The clustering result by far correlates with the ON-OFF function difference and more validation is needed on the newly identified differential genes. This opens up more opportunities for the functional studies on the ON-OFF direction selective circuit in retina.

References

Amthor, F.R., Keyser, K.T., and Dmitrieva, N.A. (2002). Effects of the destruction of starburst-cholinergic amacrine cells by the toxin AF64A on rabbit retinal directional selectivity. Visual neuroscience 19, 495-509.

Amthor, F.R., Oyster, C.W., and Takahashi, E.S. (1984). Morphology of on-off direction-selective ganglion cells in the rabbit retina. Brain research 298, 187-190.

Ariel, M., and Daw, N.W. (1982). Pharmacological analysis of directionally sensitive rabbit retinal ganglion cells. The Journal of physiology 324, 161-185.

Barlow, H.B., and Levick, W.R. (1965). The mechanism of directionally selective units in rabbit's retina. The Journal of physiology 178, 477-504.

Bloomfield, S.A. (1992). Relationship between receptive and dendritic field size of amacrine cells in the rabbit retina. Journal of neurophysiology 68, 711-725.

Bloomfield, S.A. (1996). Effect of spike blockade on the receptive-field size of amacrine and ganglion cells in the rabbit retina. Journal of neurophysiology 75, 1878-1893.

Briggman, K.L., Helmstaedter, M., and Denk, W. (2011). Wiring specificity in the direction-selectivity circuit of the retina. Nature 471, 183-188.

Caldwell, J.H., Daw, N.W., and Wyatt, H.J. (1978). Effects of picrotoxin and strychnine on rabbit retinal ganglion cells: lateral interactions for cells with more complex receptive fields. The Journal of physiology 276, 277-298.

Chalupa, L.M., and Gunhan, E. (2004). Development of On and Off retinal pathways and retinogeniculate projections. Progress in retinal and eye research 23, 31-51.

Chiao, C.C., and Masland, R.H. (2002). Starburst cells nondirectionally facilitate the responses of direction-selective retinal ganglion cells. The Journal of neuroscience : the official journal of the Society for Neuroscience 22, 10509-10513.

Demb, J.B. (2007). Cellular mechanisms for direction selectivity in the retina. Neuron 55, 179-186.

Elstrott, J., Anishchenko, A., Greschner, M., Sher, A., Litke, A.M., Chichilnisky, E.J., and Feller, M.B. (2008). Direction selectivity in the retina is established independent of visual experience and cholinergic retinal waves. Neuron 58, 499-506.

Espina, V., Wulfkuhle, J.D., Calvert, V.S., VanMeter, A., Zhou, W., Coukos, G., Geho, D.H., Petricoin, E.F., 3rd, and Liotta, L.A. (2006). Laser-capture microdissection. Nature protocols 1, 586-603.

Euler, T., Detwiler, P.B., and Denk, W. (2002). Directionally selective calcium signals in dendrites of starburst amacrine cells. Nature 418, 845-852.

Famiglietti, E.V. (2002). A structural basis for omnidirectional connections between starburst amacrine cells and directionally selective ganglion cells in rabbit retina, with associated bipolar cells. Visual neuroscience 19, 145-162.

Fosser, N.S., Brusco, A., and Rios, H. (2005). Darkness induced neuroplastic changes in the serotoninergic system of the chick retina. Brain research Developmental brain research 160, 211-218.

Guenther, E., Schmid, S., Wheeler-Schilling, T., Albach, G., Grunder, T., Fauser, S., and Kohler, K. (2004). Developmental plasticity of NMDA receptor function in the retina and the influence of light. FASEB journal : official publication of the Federation of American Societies for Experimental Biology 18, 1433-1435.

He, S., and Masland, R.H. (1997). Retinal direction selectivity after targeted laser ablation of starburst amacrine cells. Nature 389, 378-382.

Huberman, A.D., Wei, W., Elstrott, J., Stafford, B.K., Feller, M.B., and Barres, B.A. (2009). Genetic identification of an On-Off direction-selective retinal ganglion cell subtype reveals a layer-specific subcortical map of posterior motion. Neuron 62, 327-334.

Kaneda, M., Ishii, K., Morishima, Y., Akagi, T., Yamazaki, Y., Nakanishi, S., and Hashikawa, T. (2004). OFF-cholinergic-pathway-selective localization of P2X2 purinoceptors in the mouse retina. J Comp Neurol 476, 103-111.

Kaneda, M., Ito, K., Shigematsu, Y., and Shimoda, Y. (2010). The OFF-pathway dominance of P2X(2)-purinoceptors is formed without visual experience. Neuroscience research 66, 86-91.

Kay, J.N., De la Huerta, I., Kim, I.J., Zhang, Y., Yamagata, M., Chu, M.W., Meister, M., and Sanes, J.R. (2011). Retinal ganglion cells with distinct directional preferences differ in molecular identity, structure, and central projections. The Journal of neuroscience : the official journal of the Society for Neuroscience 31, 7753-7762.

Kittila, C.A., and Massey, S.C. (1995). Effect of ON pathway blockade on directional selectivity in the rabbit retina. Journal of neurophysiology 73, 703-712.

Kittila, C.A., and Massey, S.C. (1997). Pharmacology of directionally selective ganglion cells in the rabbit retina. Journal of neurophysiology 77, 675-689.

Lee, E.J., Gibo, T.L., and Grzywacz, N.M. (2006). Dark-rearing-induced reduction of GABA and GAD and prevention of the effect by BDNF in the mouse retina. The European journal of neuroscience 24, 2118-2134.

Lee, E.J., Merwine, D.K., Mann, L.B., and Grzywacz, N.M. (2005). Ganglion cell densities in normal and dark-reared turtle retinas. Brain research 1060, 40-46.

Lee, E.J., Merwine, D.K., Padilla, M., and Grzywacz, N.M. (2007). Choline acetyltransferase-immunoreactive neurons in the retina of normal and dark-reared turtle. J Comp Neurol 503, 768-778.

Lee, E.J., Padilla, M., Merwine, D.K., and Grzywacz, N.M. (2008). Developmental regulation of the morphology of mouse retinal horizontal cells by visual experience. The European journal of neuroscience 27, 1423-1431.

Lee, J.H., Daugharthy, E.R., Scheiman, J., Kalhor, R., Ferrante, T.C., Terry, R., Turczyk, B.M., Yang, J.L., Lee, H.S., Aach, J., et al. (2015). Fluorescent in situ sequencing (FISSEQ) of RNA for gene expression profiling in intact cells and tissues. Nature protocols 10, 442-458.

Lee, S., Kim, K., and Zhou, Z.J. (2010). Role of ACh-GABA cotransmission in detecting image motion and motion direction. Neuron 68, 1159-1172.

Masland, R.H. (2001). The fundamental plan of the retina. Nature neuroscience 4, 877-886.

Masland, R.H., and Ames, A., 3rd (1976). Responses to acetylcholine of ganglion cells in an isolated mammalian retina. Journal of neurophysiology 39, 1220-1235.

Oyster, C.W. (1968). The analysis of image motion by the rabbit retina. The Journal of physiology 199, 613-635.

Peters, B.N., and Masland, R.H. (1996). Responses to light of starburst amacrine cells. Journal of neurophysiology 75, 469-480.

Rossi, J., Balthasar, N., Olson, D., Scott, M., Berglund, E., Lee, C.E., Choi, M.J., Lauzon, D., Lowell, B.B., and Elmquist, J.K. (2011). Melanocortin-4 receptors expressed by cholinergic neurons regulate energy balance and glucose homeostasis. Cell metabolism 13, 195-204.

Stacy, R.C., and Wong, R.O. (2003). Developmental relationship between cholinergic amacrine cell processes and ganglion cell dendrites of the mouse retina. J Comp Neurol 456, 154-166.

Sun, L.O., Jiang, Z., Rivlin-Etzion, M., Hand, R., Brady, C.M., Matsuoka, R.L., Yau, K.W., Feller, M.B., and Kolodkin, A.L. (2013). On and off retinal circuit assembly by divergent molecular mechanisms. Science 342, 1241974.

Taylor, W.R., and Wassle, H. (1995). Receptive field properties of starburst cholinergic amacrine cells in the rabbit retina. The European journal of neuroscience 7, 2308-2321.
Tian, N., and Copenhagen, D.R. (2001). Visual deprivation alters development of synaptic function in inner retina after eye opening. Neuron 32, 439-449.

Tian, N., and Copenhagen, D.R. (2003). Visual stimulation is required for refinement of ON and OFF pathways in postnatal retina. Neuron 39, 85-96.

Wassle, H. (2004). Parallel processing in the mammalian retina. Nature reviews Neuroscience 5, 747-757.

Wei, W., Hamby, A.M., Zhou, K.L., and Feller, M.B. (2011). Development of asymmetric inhibition underlying direction selectivity in the retina. Nature 469, 402-+.

Wong, R.O.L.G., L. (2003). Development of the vertebrate retina. In The Visual Neurosciences (Cambridge, MA: MIT Press), pp. 77-93.

Yang, G., and Masland, R.H. (1994). Receptive fields and dendritic structure of directionally selective retinal ganglion cells. The Journal of neuroscience : the official journal of the Society for Neuroscience 14, 5267-5280.

Yonehara, K., Balint, K., Noda, M., Nagel, G., Bamberg, E., and Roska, B. (2011). Spatially asymmetric reorganization of inhibition establishes a motion-sensitive circuit. Nature 469, 407-+.

Yoshida, K., Watanabe, D., Ishikane, H., Tachibana, M., Pastan, I., and Nakanishi, S. (2001). A key role of starburst amacrine cells in originating retinal directional selectivity and optokinetic eye movement. Neuron 30, 771-780.

Zhang, J., Yang, Z., and Wu, S.M. (2005). Development of cholinergic amacrine cells is visual activity-dependent in the postnatal mouse retina. J Comp Neurol 484, 331-343.

Zheng, J.J., Lee, S., and Zhou, Z.J. (2004). A developmental switch in the excitability and function of the starburst network in the mammalian retina. Neuron 44, 851-864.

Appendix

Supplementary Figures

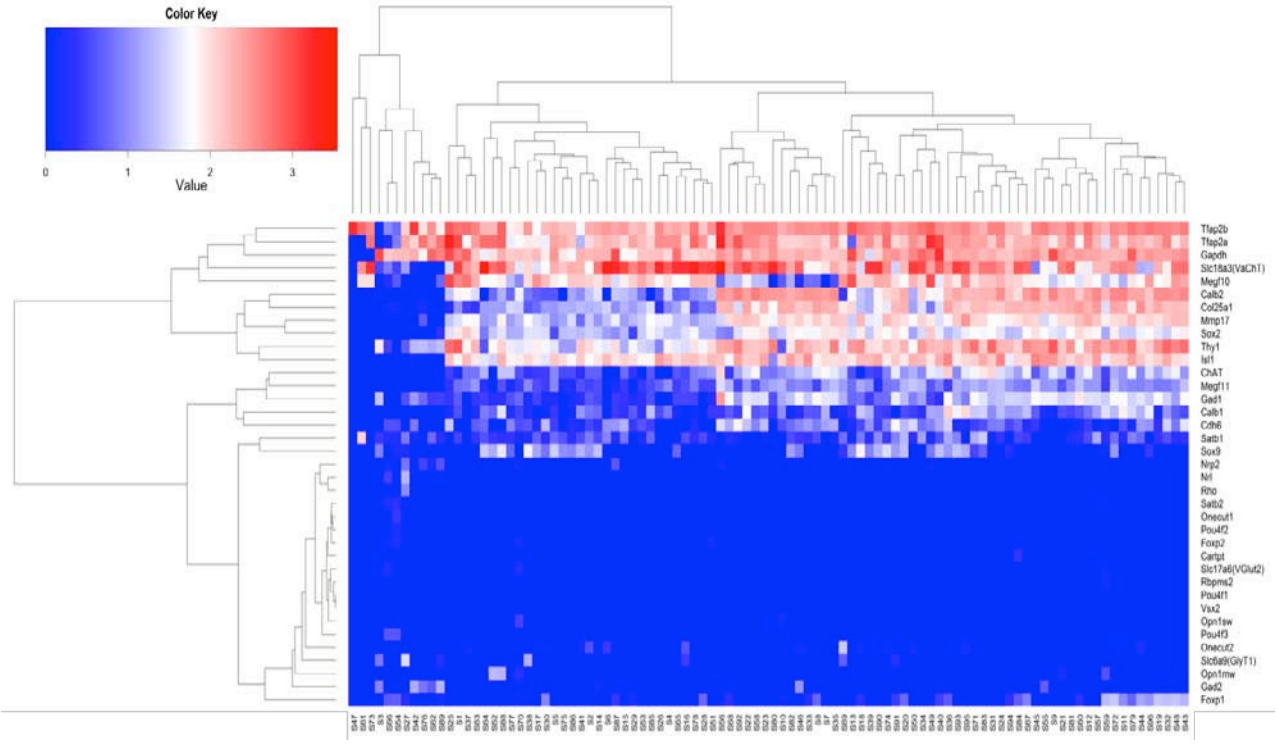

Figure S7.1 Clustering of 96 SACs based on marker genes and control genes of SACs. There are several key marker genes missing in 11 SACs, which may due to the sample processing problems or mixture of other cell types. These 11 cells were screened out for the following analysis.

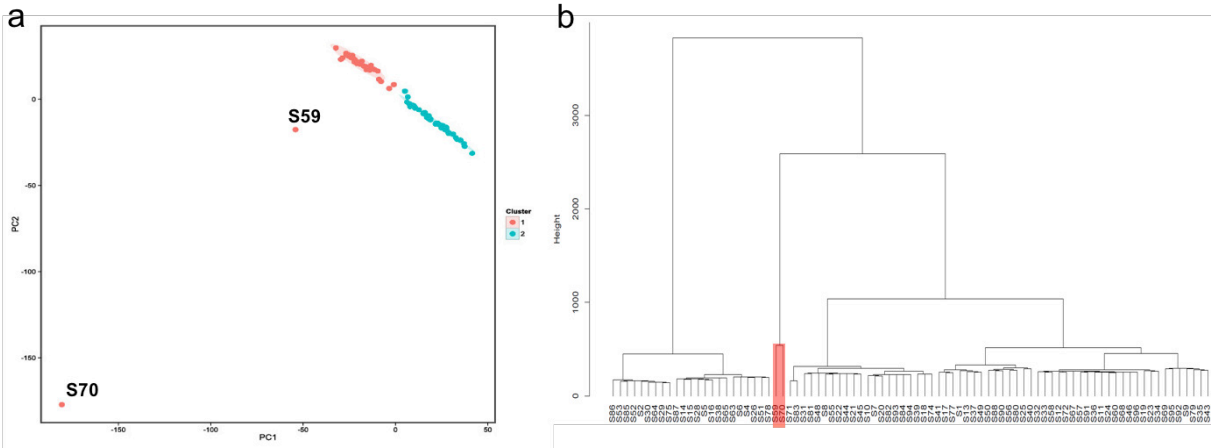

Figure S7.2 (a) Principle Component Analysis (PCA) (b) Hierarchical clustering of the transcriptome of the remaining 85 SACs. S50 and S70 (marked in red) are far away from most of the cells on the PCA plot as well as in hierarchical clustering analysis. These two cells were screened out for the following analysis.

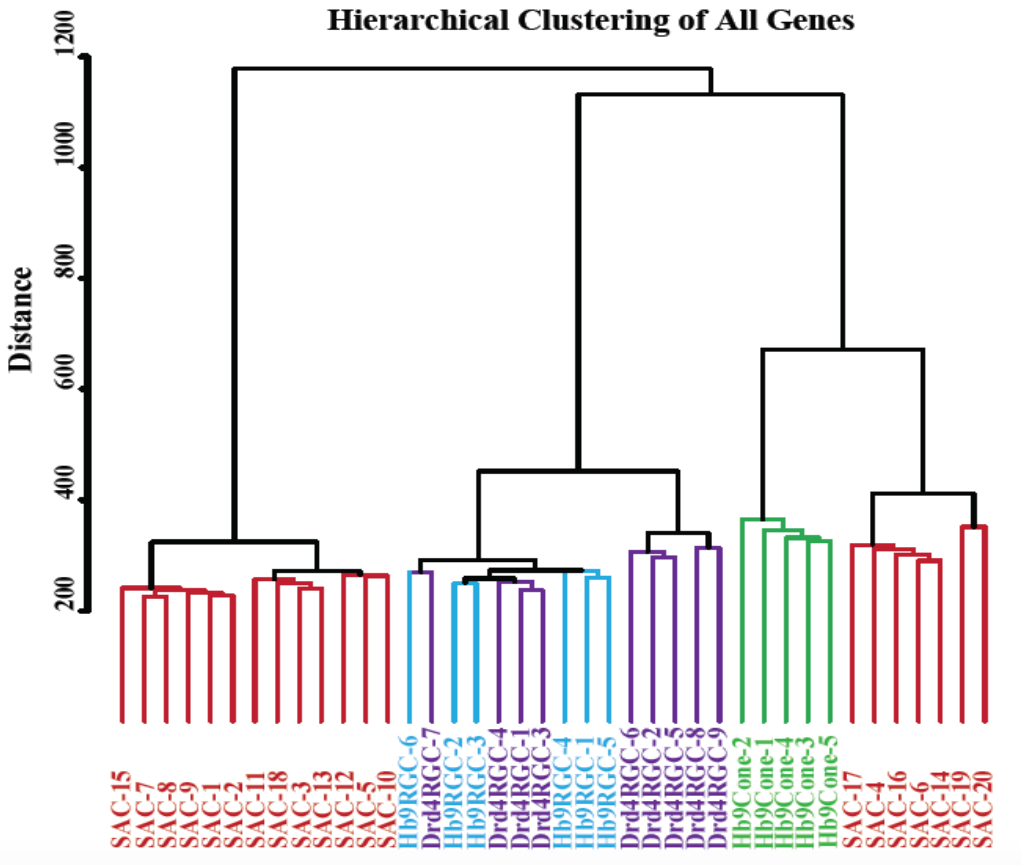

Figure S7.3 Hierarchical clustering of all SACs, RGCs and photoreceptors.

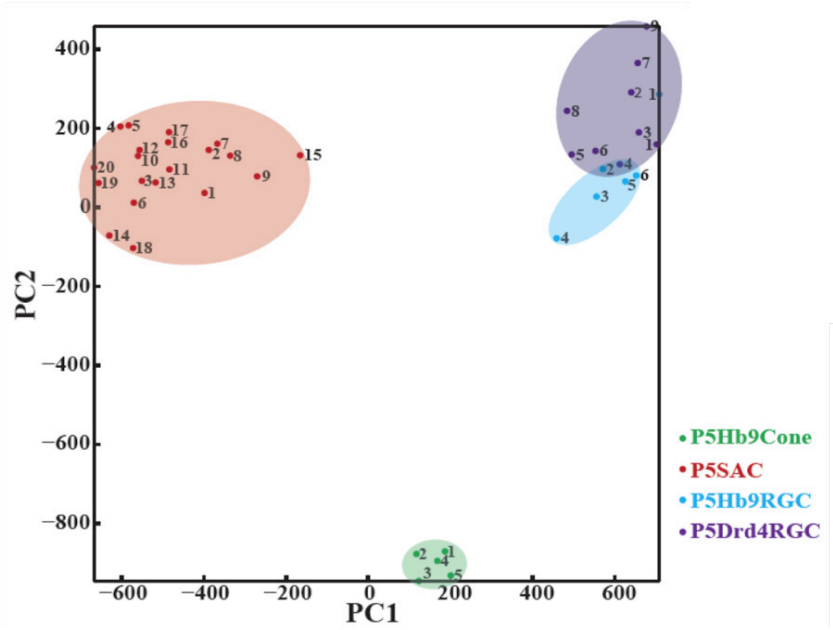

Figure S7.4 Principle component analysis of all SACs, RGCs and photoreceptors.

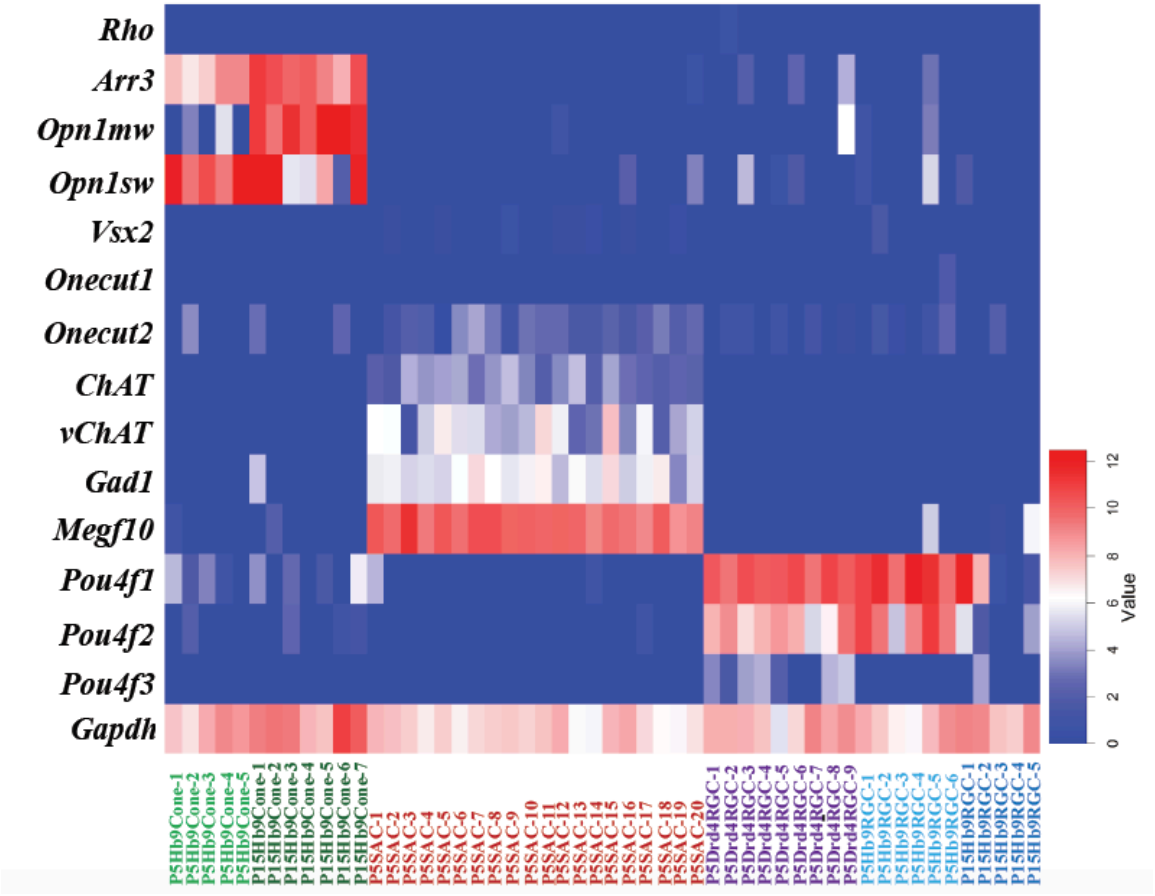

Figure S7.5 Heat map of the marker genes for SACs, RGCs and photoreceptor cones.